

BRIGHT-FIELD AND FLUORESCENCE
CHIP-SCALE MICROSCOPY FOR
BIOLOGICAL IMAGING

Thesis by
Seung Ah Lee

In Partial Fulfillment of the Requirements for the degree
of
Doctor of Philosophy



CALIFORNIA INSTITUTE OF TECHNOLOGY
Pasadena, California
2014
(Defended January 24, 2014)

ACKNOWLEDGEMENTS

First and foremost, I would like to express my deepest gratitude to my advisor, Dr. Changhuei Yang, for his guidance throughout my study. His insights and ideas has taught me how to do scientific research. His passion and enthusiasm for research has been the strongest motivation for me. His patience and encouragement had always pointed me towards the right direction when I was in doubt. I am grateful for the wonderful research environment he provided the group with and the creative energy that inspires everyone. I cannot imagine having a better advisor and a mentor.

I would like to show my deepest appreciation to my committee members, Dr. Yu Chong Tai, Dr. P. P. Vaidyanathan, Dr. Rustem Ismagilov and Dr. Hyuck Choo. Their insightful comments and suggestions have allowed me to explore more in depth and to improve my work.

A large portion of my Ph.D. work has been done in collaboration with Dr. Ana Rodriguez's group at New York University. I would like to thank Dr. Rodriguez for her help and guidance. I always had a great time visiting her lab at NYU and I also want to thank Dr. Ricardo Leitao, Dr. Cristina Fernandez, Jessey Erath and Maureen Ty for their help.

I have greatly benefited from everyone in the Biophotonics group. I learned so much from Dr. Guoan Zheng and I thank him for his help and inspirations. I thank Dr. Shuo Pang and Chao Han for their help and also for being great office mates. Dr. Lap Man Lee, Dr. Benjamin Judkewitz, Mooseok Jang, Xiaoze Ou, Jinho Kim, Dr. Jaehee Jung, Dr. Ying Min Wang, Roarke Horstmyer, Edward Zhou and Dr. Jiangtao Huangfu also deserve my sincerest thanks. None of this would have been possible without our amazing manager, Anne Sullivan. I cannot thank her enough for all the things she has done for us. I also thank the undergraduate members of the group (Samuel, Nandini, Karen and Donghun). I feel very lucky to have been able to work with such a nice, brilliant and interesting group of people.

I thank the staffs at Kavli Nanosciences Institute at Caltech, especially Bophan Chimm, Melissa Melendes and Steven Martinez for their help. Alireza Ghaffari's support the Watson cleanroom facilities were invaluable.

I have been blessed with a great group of friends and colleagues here at Caltech. I want to express my appreciation to every single one of them for making my life at Caltech so enjoyable and memorable. Also, I want to thank my dear friends in Korea and in the States for their warm support.

Last but not least, I thank my parents for their limitless support and love. My family is the reason I strive every day. I would like to dedicate this thesis to my beloved parents.

ABSTRACT

Optical microscopy is an essential tool in biological science and one of the gold standards for medical examinations. Miniaturization of microscopes can be a crucial stepping stone towards realizing compact, cost-effective and portable platforms for biomedical research and healthcare. This thesis reports on implementations of bright-field and fluorescence chip-scale microscopes for a variety of biological imaging applications. The term “chip-scale microscopy” refers to lensless imaging techniques realized in the form of mass-producible semiconductor devices, which transforms the fundamental design of optical microscopes.

Our strategy for chip-scale microscopy involves utilization of low-cost Complementary metal Oxide Semiconductor (CMOS) image sensors, computational image processing and micro-fabricated structural components. First, the sub-pixel resolving optofluidic microscope (SROFM), will be presented, which combines microfluidics and pixel super-resolution image reconstruction to perform high-throughput imaging of fluidic samples, such as blood cells. We discuss design parameters and construction of the device, as well as the resulting images and the resolution of the device, which was $0.66\ \mu\text{m}$ at the highest acuity. The potential applications of SROFM for clinical diagnosis of malaria in the resource-limited settings is discussed.

Next, the implementations of ePetri, a self-imaging Petri dish platform with microscopy resolution, are presented. Here, we simply place the sample of interest on the surface of the image sensor and capture the direct shadow images under the illumination. By taking advantage of the inherent motion of the microorganisms, we achieve high resolution ($\sim 1\ \mu\text{m}$) imaging and long term culture of motile microorganisms over ultra large field-of-view ($5.7\ \text{mm} \times 4.4\ \text{mm}$) in a specialized ePetri platform. We apply the pixel super-resolution reconstruction to a set of low-resolution shadow images of the microorganisms as they move across the sensing area of an image sensor chip and render an improved resolution image. We perform longitudinal study of *Euglena gracilis* cultured in an ePetri platform and image based analysis on the motion and morphology of the cells. The ePetri device for imaging non-motile cells are also demonstrated, by using the sweeping illumination of a light emitting diode (LED) matrix for pixel super-resolution reconstruction of sub-pixel shifted shadow images. Using this prototype device, we demonstrate the detection of waterborne parasites for the effective diagnosis of enteric parasite infection in resource-limited settings.

Then, we demonstrate the adaptation of a smartphone's camera to function as a compact lensless microscope, which uses ambient illumination as its light source and does not require the incorporation of a dedicated light source. The method is also based on the image reconstruction with sweeping illumination technique, where the sequence of images are captured while the user is manually tilting the device around any ambient light source, such as the sun or a lamp. Image acquisition and reconstruction is performed on the device using a custom-built android application, constructing a stand-alone imaging device for field applications. We discuss the construction of the device using a commercial smartphone and demonstrate the imaging capabilities of our system.

Finally, we report on the implementation of fluorescence chip-scale microscope, based on a silo-filter structure fabricated on the pixel array of a CMOS image sensor. The extruded pixel design with metal walls between neighboring pixels successfully guides fluorescence emission through the thick absorptive filter to the photodiode layer of a pixel. Our silo-filter CMOS image sensor prototype achieves 13- μm resolution for fluorescence imaging over a wide field-of-view ($4.8 \text{ mm} \times 4.4 \text{ mm}$). Here, we demonstrate bright-field and fluorescence longitudinal imaging of living cells in a compact, low-cost configuration.

TABLE OF CONTENTS

Acknowledgements	iii
Abstract.....	v
Table of Contents	vii
List of illustrations and/or tables.....	9
Chapter 1. Introduction	15
1.1 Conventional Microscopy	15
1.2. Modern Lensless Microscopy techniques.....	17
1.2.1 Digital Inline holography	18
1.2.2 Optofluidic Microscopy.....	19
1.2.3 Shadow imaging	20
1.3 CMOS image sensors for lensless microscopy.....	21
1.4 Organization of this thesis.....	22
Bibliography	24
Chapter 2. Sub-pixel resolving optofluidic microscope (SROFM)	26
2.1 Imaging principle.....	26
2.1.1 Pixel super-resolution reconstruction.....	26
2.1.2 Microfluidic scanning for pixel super-resolution reconstruction	28
2.1.3 Fundamental limits of sub-pixel resolving optofluidic microscopy.....	30
2.2 Construction of SROFM device.....	37
2.3 Monochromatic imaging	38
2.3.1 Motion vector estimation.....	38
2.3.2 SROFM imaging of biological samples.....	41
2.3.3 Imaging rotating samples	42
2.3.4 Resolution of SROFM.....	44
2.4 Color SROFM based on RGB illumination.....	45
2.5 Malaria screening with SROFM	47
2.5.1 Device optimization for blood cell imaging	48
2.5.2 Sample preparation	50
2.5.3 SROFM imaging of malaria infected red blood cells.....	51
2.6 Discussion.....	52
Bibliography	55
Chapter 3. Sub-pixel resolving motion microscopy (SPMM)	57
3.1 ePetri : self-imaging culture dish	57
3.2 SPMM Working principle and Device design.....	58
3.3 SPSM imaging of <i>Euglena gracilis</i>	60
3.4 Motion artifacts in SPMM.....	63
3.4.1 Scanning direction	63
3.4.2 Rotation.....	64
3.5 Longitudinal imaging of <i>Euglena gracilis</i>	66
3.6 Conclusion	69
Bibliography	71
Chapter 4. Sub-pixel perspective sweeping microscopy (SPSM).....	72
4.1 Imaging principle.....	72
4.2 Waterborne parasite detection with SPSM	74
4.2.1 Background.....	74

4.2.2 Device Construction	75
4.2.3 Color SPSM imaging of waterborne parasites.....	78
4.2.4 Identification of parasite cysts.....	80
4.3 Discussions	82
Bibliography	83
Chapter 5. Smartphone-based chip-scale microscope for portable imaging	84
5.1 Background.....	84
5.2 Working principle.....	86
5.3 Device construction.....	87
5.3.1 Hardware design	87
5.3.2 Android Application design	88
5.3.3 Motion tracing and image reconstruction	89
5.4 Portable imaging with smartphone microscope.....	92
5.5 Discussions	95
Bibliography	97
Chapter 6. Fluorescence chip-scale microscopy with silo-filter image sensor.....	99
6.1 Background.....	99
6.1.1 Optical requirements for fluorescence detection	99
6.1.2 Epifluorescence microscopy	101
6.1.2 Fluorescence on-chip microscopy.....	102
6.2 Fluorescence imaging with uniform filter coating	103
6.3 Fluorescence imaging with silo-filter sensors	105
6.3.1 Imaging system design	106
6.3.2 Fabrication of silo-filter structures.....	107
6.3.3 Performance and fluorescence collection efficiency	108
6.3.4. Resolution limit of Silo-filter structure	110
6.4 Fluorescence live-cell imaging with Silo-filter image sensors	111
6.5 Discussions	114
Bibliography	115
Chapter 7. Summary.....	116

LIST OF ILLUSTRATIONS AND/OR TABLES

<i>Number</i>	<i>Page</i>
Figure 1 - 1. Diagram of Olympus BX41 transmitted and reflected light microscope equipped for epifluorescence illumination.	16
Figure 1 - 2. Schematic diagram of different generations of optofluidic microscopy systems. (a) Aperture-based OFM uses multiple line scans of sample collected through a small aperture on the pixel of the image sensor. (b) FZP-OFM is based on the line scans by the focused illumination created by diffractive optical elements mounted on the microfluidic channel. (c) Sub-pixel resolving OFM, which will be discussed later in this theses uses multiple direct shadow images and computational image processing to obtain high resolution images.	20
Figure 1 - 3. CMOS image sensors with different optical formats. Top Aptina 5.2 - μm 1.3 Megapixel sensor with 1280×1024 pixels (top left), Aptina 2.2- μm 5 Megapixel sensor with 1944×2592 pixels (top right) and Samsung 1.12- μm 12 Megapixel sensor with 4208×3120 pixels mounted on a interconnect module (bottom left).	22
Figure 2 - 1. Block diagram representation of the image acquisition model in pixel super-resolution reconstruction process.	27
Figure 2 - 2. Sub-pixel scanning of images by microfluidic channel mounted on top of the image sensor.	29
Figure 2 - 3. Sub-pixel shifts of microfluidically scanned object with different channel alignment angles. When the angle is too small, the sample does not scan enough through y direction (Left). At $\theta = 26.5^\circ$ where $\tan\theta = 12$, $[dx, k, dy, k]$ values are repeated, yielding an undesirable motion vector. Flow velocity of $v_0=500 \mu\text{m/s}$, frame rate $f=800\text{fps}$, pixel size $D=2.2 \mu\text{m}$ and total number of frame $N=100$ was used.	30
Figure 2 - 4. Schematic diagram of SROFM image acquisition model.	32
Figure 2 - 5. SROFM image acquisition with synthetic images. Original image of line pairs with line width l is propagated to sample height z via angular spectrum analysis. The resulting shadow images are digitally scanned over the image sensor and the corresponding low resolution sequence is processed with pixel super-resolution with varying parameters.	33
Figure 2 - 6. Resolution of SROFM. (a-b) Vertical summed pixel values of reconstructed images plotted over varying line pair widths. First line width that can be resolved into three dark lines are considered as the resolution limit. (c) Resolution with varying sample height, sensor's pixel size and fill factor.	34
Figure 2 - 7. Schematics of the SROFM device. (a) A sample, depicted as a cell in the figure, is flown in a microfluidic channel on top of an image sensor and the LR projection images are recorded. (b) Image reconstruction from low resolution sequence to high resolution image. Scale bar indicates $5 \mu\text{m}$. (c) Photograph of an actual sub-pixel resolving optofluidic microscope (SROFM) device and the image sensor. Current SROFM device composed of the CMOS sensor-based SROFM chip and camera head. The SROFM chip measures $1 \text{ cm} \times 1 \text{ cm}$ and the total device, $5 \text{ cm} \times 3 \text{ cm} \times 3 \text{ cm}$ in size. (d) Illustration of a SROFM sensor that has microfluidic channel mounted on top of a CMOS image sensor.	38
Figure 2 - 8. Improvement of the HR image with the non-linear motion vector estimation. (a) Measurement of motion vector from the raw sequence shows the error between the linearly estimated motion vector and the actual motion of the object. (b) The raw image of the sample. (c) HR image reconstructed with the linearly estimated motion vector. The streaks and jagged	

- edges in the image result from the discrepancy between the motion vector used in reconstruction and the actual location of the object. (d) HR image reconstructed with the non-linear motion vector measured with the methods described above. All scale bars indicate $10\mu\text{m}$ 40
- Figure 2 - 9. Motion estimation of microspheres smaller than the pixel size ($1\mu\text{m}$ microspheres). (a) Raw LR image showing the channel structure. (b) Normalized raw image with the contrast enhanced. The response of the pixels under the red line, which is parallel to the channel wall, is processed to obtain the motion vector. (c) Time resolved response of the line of pixels show the microspheres passing through each pixel. The slope of streaks ($\Delta x/\Delta t$) indicates the motion vector in x direction and $\Delta y/\Delta t$ can be calculated from the slope of the red line in (b). (d) HR image of the microspheres reconstructed with the motion vector obtained from (c). All scale bars indicate $20\mu\text{m}$ 41
- Figure 2 - 10. Images obtained from the SROFM device. Entamoeba invadens cysts (a-b). Raw low resolution (LR) images from the sensor (Top row), High resolution (HR) images reconstructed from the sequence of LR images (Middle row) and conventional bright field microscope images taken with $20\times$ objective lens (Bottom row). 40 to 50 LR frames were used to reconstruct each HR image. 42
- Figure 2 - 11. Sequential HR images of rotating cells (scale bar $10\mu\text{m}$). (a) Cells flowing with rotational movement allow the SROFM to capture images of different projections, revealing the three-dimensional inner cellular structures. (b) HR sequence of an Entamoeba invadens cyst traveling with in-plane rotation. Note that the highlighted part of the sample is rotating in the sequence. The length of the dark spot in the highlighted region is also decreasing in the time lapse, indicating that the sample has out-of-plane rotation as well. (c) Sample translating with out-of-plane rotation. The highlighted regions with the same color reveal that the pairs of images are rotated 180 degrees out-of-plane of each other. Each pair of images is distinct from the others, showing the complex inner structure of the cell from a different projection plane. 43
- Figure 2 - 12. Resolution of the SROFM prototype obtained with $0.5\mu\text{m}$ microspheres. (a) Intensity profile of the $0.5\mu\text{m}$ microsphere from image reconstructed with an enhancement factor of 10 and pixel size of $3.2\mu\text{m}$ (inset). (b) Intensity profile of the same sphere reconstructed with an enhancement factor of 13 (inset). (c) Intensity profile of the $0.5\mu\text{m}$ microsphere imaged with enhancement factor of 10 and pixel size of $2.2\mu\text{m}$ (inset). FWHMs of the profiles in (a) and (b) are $0.8\mu\text{m}$, $0.66\mu\text{m}$ and $0.59\mu\text{m}$ respectively. 45
- Figure 2 - 13. Color SROFM using sequential RGB LED illumination. 46
- Figure 2 - 14. Color response of our SROFM device. Light transmission through a $27\mu\text{m}$ channel containing different concentrations of Trypan blue dye. This figure demonstrates agreement with the Beer-Lambert law of light absorption, validating SROFM's color imaging capabilities. 47
- Figure 2 - 15. Schematics and prototypes of our color SROFM device. (a) Schematics of color SROFM system showing sequential RGB LED illumination and SROFM device controlled by a computer. (b) Detailed view of color imaging area where the sample, blood cells, is flowing in the channel on top of the sensor's pixel grid while the illumination is varied in color. (c) Low resolution image of blood cells in a SROFM device directly taken from the CMOS image sensor. (d) Conventional bright field microscope image of the same field of view, taken with a $10\times$ objective lens. Scale bars indicate $20\mu\text{m}$ 49
- Figure 2 - 16. (a) Drop-and-flow scheme for high-throughput imaging of blood cells. (b) Channel design for blood cell imaging 50
- Figure 2 - 17. SROFM images of *P. falciparum*-infected and naïve RBC. (a) Red, green, blue and combined color images of *P. falciparum* schizont-stage RBCs stained with Toluidine blue,

- showing a distinct purple spot within each RBC, which appears as dark spots in the green channel. (b) Images of naïve RBCs show clear differences with the infected RBCs. Naïve RBCs were also stained with Toluidine blue as a control. 51
- Figure 2 - 18. Color SROFM and conventional microscope images of *P. falciparum*-infected and naïve RBC. (a) *P. falciparum* schizont stage RBC images taken with color SROFM system. (b) naïve RBC images taken with color SROFM. (c-d) Bright field microscope images of *P. falciparum*, trophozoite-stage, schizont-stage and Naïve RBCs stained with Toluidine blue. Images are taken with (c) 40× and (d) 100x objective lens. Scale bars indicate 5 μm 52
- Figure 3 - 1. Schematic diagram of ePetri device for SPSM imaging of motile microorganisms. (a) ePetri dish imaging platform is composed of an ePetri chip, camera module and a control computer. A Peltier module and a heat sink are used to maintain the temperature of the chip. (b) Schematic diagram of a single ePetri dish chip. Sample is dispensed into a chip and a drop of oil is used to prevent evaporation of the medium. 59
- Figure 3 - 2. Raw (a) and reconstructed (b) images of *Euglena gracilis* using SPMM method with $n=5$. (c) A conventional microscope image of a *Euglena gracilis* taken with a 10x objective lens. The scale bar indicates 10 μm . (d) The line traces of a small bright feature in the reconstructed image Inset corresponds to the area highlighted in (b). 62
- Figure 3 - 3. Motion of an *Euglena gracilis* cell over 25 frames (a) and the motion vector obtained via our tracing program (b). 62
- Figure 3 - 4. Artifacts in image reconstruction and improved images. Cells moving in horizontal direction show missing information in y direction and (c) a different sequence of the same cell with adequate motion vector showing a well-reconstructed image. (d) Motion vector for *Euglena gracilis* corresponding to images (a)-(c). The scale bar indicates 10 μm 63
- Figure 3 - 5. Cells with large rotational movement show artifacts at the two ends of the cell (b). Reconstructed image with rotation compensation (c). Rotation angle measured by the angle of the microorganism. The scale bar indicates 10 μm 65
- Figure 3 - 6. Cells with large rotational movement show artifacts at the two ends of the cell (b). Reconstructed image with rotation compensation (c). Rotation angle measured by the angle of the microorganism. The scale bar indicates 10 μm 65
- Figure 3 - 7. Longitudinal imaging of *Euglena gracilis* on ePetri dish. (a), (b) Large FOV images of *Euglena gracilis* at 1hr and 4.5 hrs, respectively. Yellow line shows traces of each cell for 1 second. (Scale bar 200 μm) (c) Growth in cell population counted with our cell counting software (blue) and manually counted (green, yellow). (d) High resolution images of *Euglena gracilis* reconstructed with SPMM method (selected). Scale bar indicates 20 μm 67
- Figure 3 - 8. Motion tracking and shape analysis using ePetri. (a-b) Euglenas cultured in spring water (a) and in euglena medium. Scale bar indicates 200 μm . (b) shows difference in their motion and the cell sizes. (c) Motility distribution of the cells. (d) Aspect ratio (major axis / minor axis) distribution of the cells. 69
- Table 3 - 1. Cell counting results and percentage difference between the machine count and two manual count results. 68
- Figure 4 - 1. Schematic of the working principle of SPSM color imaging. (a) While the target objects rest on the surface of the image sensor, we sequentially turn on each LED in the RGB LED array illumination above and take sequences of low-resolution images. (b) Each low-resolution sequence is reconstructed into three monochromatic high-resolution images using

	the pixel super-resolution algorithm. The red, green, and blue channels are then combined into a single color image.	74
Figure 4 - 2.	(a) Lens-less SPSM imaging system prototype. (b) A CMOS image sensor with a microfluidic chamber mounted on the sensor surface for sample loading (top). A sample slide can be made directly on the image sensor (bottom).	76
Figure 4 - 3.	Full field-of-view ($5.7 \text{ mm} \times 4.3 \text{ mm}$) of <i>E. invadens</i> cysts with iodine staining. The inset shows part of the reconstructed image.	77
Figure 4 - 4.	SPSM and $20\times$ objective microscope images of Giardia, Cryptosporidium, and Entamoeba cysts. We imaged unstained cysts, iodine-stained, and methylene blue-stained cysts.	78
Figure 4 - 5.	Digital refocusing of SPSM. (a) Refocusing is based on the difference in sub-pixel shift at different height planes. (b) Digitally refocused images of parasite cysts. Entamoeba (blue), giardia (red), and cryptosporidium (black) can be found in different z-planes.	80
Figure 4 - 6.	Images used in the identification experiments. $20\times$ objective microscope (Left) and SPSM (Right) images of Cryptosporidium (top), Entamoeba (center) and Giardia cysts (bottom) used for the blind experiment and the automatic cell identification experiments.	81
Table 4 - 1.	Results of cell-type identification tests with conventional and SPSM images.	82
Figure 5 - 1.	Working principle of the smartphone-based chip-scale microscope. (a) Using sunlight as the light source for imaging, the user holds the smartphone with the back camera module facing the sun, slowly moves the device to capture multiple images with varying angle of illumination. (b) The prototype device uses the back camera module of an android phone. We remove the lens module of the camera and place the sample directly on the surface of the image sensor. The inset shows the image sensor module with the lens removed.	86
Figure 5 - 2.	Shadow images of the reference target under the indirect and direct illumination. (a) The target image taken under the room light with multiple fluorescent bulbs and (b) under a flashlight. The target (cross-mark) is $200 \mu\text{m} \times 200 \mu\text{m}$ in size.	87
Figure 5 - 3.	Layout of pixel geometry. Due to the debayering process in the camera module, we selected green pixels out of RGB bayer pattern and rotated the image 45° to obtain real images. The effective pixel size increases by factor of $\sqrt{2}$	88
Figure 5 - 4.	Imaging process of with the custom-built application. (a) Upon start, user can select to acquire new data using the camera, or load acquired images from the memory. (b) When capturing new data set, the user points the camera towards the sun and start capturing images. Reference target (a cross mark) shown in the upper left corner of the field of view is traced in each frame and the measured shifts are plotted over the camera view. Captured images are saved in the data storage, under a specified folder. Once the capturing if finished, user can choose to close the camera and return to the main window or to capture the data again. The sample used in this demonstration is unstained blood smear. (c) From the main window, user can select the load images button and load one of the acquired images from the gallery. The application prompts the user to select a smaller region to reconstruct. (d) Once a target region is selected, the application returns to the main window and plots the low resolution images of the selected region. The user clicks start processing button, and the application crops the entire low resolution sequence and pre-process the data to normalize the background and plots the measured tilt angles. (d) Once the pre-processing is done, user can start	

- reconstruction. (e) The final high-resolution image is shown in the application and automatically saved to the data storage. 89
- Figure 5 - 5. Raw and reconstructed images of 2.5 μm microspheres. (a) 100 frames of low resolution images were taken while we manually tilt the device. (b) The tilt angle for each image is measured by the shift of target object. (c) Reconstructed images show bright centers of the microspheres. 90
- Figure 5 - 6. Microsphere (2.5 μm and 1.75 μm) images taken under various illumination sources. Under (a) LED flashlight in a smartphone, (b) Fluorescent light bulb (compact type, 15W) and (c) sunlight (clear sky, 2pm). For all experiments, we placed an IR filter and a ND filter (2OD) above the image sensor. For (a) and (b), images were taken at 30 cm away from the light source. 91
- Figure 5 - 7. Microsphere images taken under different scanning motion. (a) Careful x, y scanning by monitoring the target tracing results, and (b) Random scanning by continuously tilting the device without target tracing. Insets show the tracing results. Both images were taken under sunlight illumination. Scale bar indicates 5 μm 92
- Figure 5 - 8. Wright-Giemsa stained blood smear. (a) A full FOV image of a blood smear made on the image sensor. Image sensor measures 4.5 mm \times 3.6 mm and the scale bar indicates 1 mm. (b) Raw and (c) reconstructed high resolution image of the region highlighted in (a). Images are reconstructed in the custom-built application. Scale bar indicates 20 μm 93
- Figure 5 - 9. Blood smear images taken under various illumination sources. Under (a) sunlight (clear sky, 2pm), (b) Fluorescent light bulb (Spiral type, 15W) and (c) LED flashlight in a smartphone. For all experiments, we placed an IR filter and a ND filter (2OD) above the image sensor. For (b) and (c), images were taken at 30cm away from the light source. 94
- Figure 5 - 10. (a) Images captured with 500-nm polystyrene microspheres on the image sensor. We used 1.12- μm pixel sensors (effective low-resolution pixel size of 1.58 μm) (b) Magnified images of the microsphere marked in (a). We used 13x and 8x enhancement for high resolution reconstruction. One pixel in each image measures 120 and 200 nm, respectively. (b) Line trace of a microsphere images with 13x and 8x enhancement. In both cases, the center of the microsphere is resolved. 94
- Figure 5 - 11. Portable microscopy of fresh-water microorganisms for water quality monitoring. (a) We took the fresh-water sample directly from a koi pond. 20- μL of sample was dispensed on the image sensor and the particles were let settle down for few minutes before image acquisition. (b) Conventional microscope images of same sample taken with 20 \times (0.4 Numerical Aperture) objective lens. (c-d) Reconstructed images of green algae found in the pond. The green algae found in the sample are different species of *Scenedesmus*, a genus of *Chlorophyceae*. All scale bars indicate 20 μm 95
- Figure 6 - 1. Fluorescence absorption and emission spectrum of Alexa 594 fluorochrome and the transmission characteristics of a commercial filter set typically used for detection of red fluorochromes such as Alexa 594, Texas red and mCherry. This plot is obtained from Chroma spectra viewer (<http://www.chroma.com/spectra-viewer?fluorochromes=49&set=757&showDetails=1>)..... 101
- Figure 6 - 2. Schematics of a wide-field epifluorescence microscope equipped with a fluorescent filter cube. 102
- Figure 6 - 3. Bright-field and fluorescence imaging system using a filter coated CMOS imager. (a) Schematic diagram of the proposed imaging system consisting a red LED array, high power LED for fluorescence excitation. (b) Compact chip-scale fluorescence microscope in action. 104

- Figure 6 - 4. Fluorescence(a), bright-field(b) and overlay(c) images of stool smear sample of a *Giardia lamblia* infected patient. The sample is treated with immunofluorescence stain targeted for giardia. Marked cells in (c) indicate giardia cysts..... 105
- Figure 6 - 5. Fluorescence and bright field imaging configurations. (a-b) CMOS sensors coated with uniform filter layer. The fluorescence emission will blur out to several adjacent pixels. Bright-field shadow images will also deteriorate due to the increased distance between the pixel array and the sample. (c-d) Fluorescence and bright-field imaging with silo-filter sensors. Metal grid structure for pixelation in the filter layer guides fluorescence emission and relays focal plane through the filter layer. 106
- Figure 6 - 6. Schematic diagram of the SF structure for fluorescence chip-scale microscope. 107
- Figure 6 - 7. Fabrication process for silo-filter structures on a commercial CMOS image sensor. 108
- Figure 6 - 8. SEM micrograph of fabricated metal grid structure. Scale bar in (a) indicates 10 μm 108
- Figure 6 - 9. Transmission of light at varying incidence angles for uniform filter and silo-filter with 560 nm (green) and 625 nm (red) plane wave illumination. The transmission curve of the Orasol® Red filter (3 μm) is shown (inset). 109
- Figure 6 - 10. (b) Bright-field and fluorescent images of fluorescent (2.5 μm) and non-fluorescent (2.0 μm) microbeads in UF and SF sensors. Results are confirmed with 10 \times objective microscope images..... 110
- Figure 6 - 11. Resolution of silo-filter CMOS sensor. (a-c) Point spread functions of 2.5- μm fluorescent microbeads on 8- μm uniform filter coating (a), and 6- μm silo-filter coating. One pixel in all images are 5.2 μm . In (b) the microbead was located on top of the pixel and (c) in between two pixels. (d) Corresponding full-width-half at maximum values of point spread functions in (a-c). 111
- Figure 6 - 12. Bright-field and fluorescence images of living cells taken with a SF sensor chip. The sample is MCF-7 cells stained with SYTO-64 nucleic acid stain. (a) Full FOV bright-field and fluorescence overlay image. (b-c) Overlay and fluorescence images of region highlighted in (a). (d-f) SF sensor bright-field, fluorescence and overlay images. (g) 20 \times objective microscope image of the same type of cells on a conventional petri dish. 112
- Figure 6 - 13. Bright-field and fluorescence images of mCherry-HEK293 cells taken with a SF sensor chip. (a-b) Full FOV fluorescence and overlay image. (c-e) Brightfield, fluorescence and overlay images of region highlighted in (a,b). 113
- Figure 6 - 14. Time-lapse sequence showing migration and mitosis (b,boxed) of HEK 293-mCherry cells..... 113

INTRODUCTION

Optical microscopes are one of the most widely used equipment in biological science and medicine. Since its invention in the 17th century, optical microscopes have unveiled many secrets of nature, including the discoveries of cells as the building blocks of life. Microscopes has continuously improved with new technologies developed to optimize, improve and break its own limits. However, the fundamental working principle of light microscopy remains unchanged, thus most microscopes require the same key structural components that are rather bulky and expensive. Among many directions in the evolution of microscopes, miniaturization is an exciting topic as well as a challenging problem, which this thesis will be focused on.

As an introduction to this thesis, we will first review the basic principle and concepts in light microscopy and discuss the fundamental limitations. Then, we will give an overview of some of the recent efforts to transform the microscopes and the technical innovations that enable these transformations. Finally, we will introduce our approach in constructing “chip-scale microscopes” and outline the organization of this thesis.

1.1 Conventional Microscopy

Modern compound microscopes typically consists of an illuminator, a condenser, sample stage, objective lens, detector and several light conditioning components (Figure 1 - 1)[1]. Most modern microscopes are equipped with the Köhler illumination setup, which was first introduced in 1893 by August Köhler. Köhler illumination setup utilizes collector lens above the lamp so that the image of the lamp filament can be focused on the condenser diaphragm at the front focal plane of the condenser. Because the light source is not focused at the sample plane, the illumination can be uniform and extended over the imaging field-of-view (FOV). The specimen, usually mounted on a glass slide with a coverslip, resides on a translation stage that allows for positioning and focusing of the specimen. The objective lens is the most important and perhaps the most costly image-forming object in a microscope which determines various imaging parameters such as magnification, resolution and FOV. Modern microscopes typically employ infinitely-corrected objectives, which project rays in parallel bundles. These rays are focused at the detector plane by a tube lens. This scheme allows for insertion

of auxiliary optical elements, such as polarizers, prisms and filters, between the parallel optical path between the objective and tube lens.

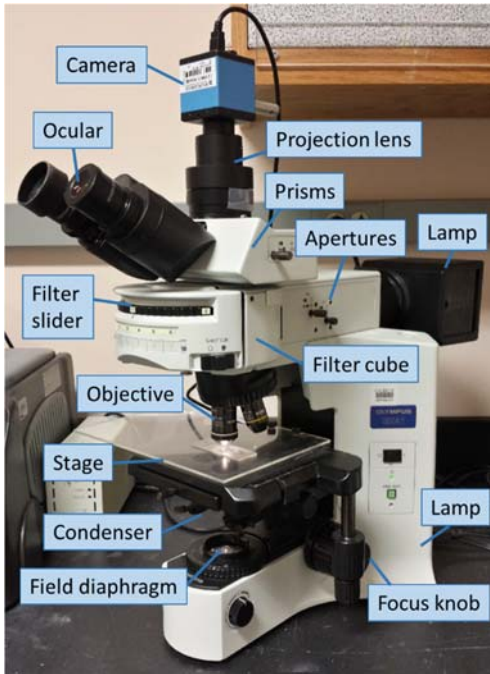


Figure 1 - 1. Diagram of Olympus BX41 transmitted and reflected light microscope equipped for epi-fluorescence illumination.

Several parameters of imaging is determined by the objective lens used in the microscope. Magnification of infinity-corrected optical microscope systems is determined by the ratio of the focal lengths of the tube lens and the objective lens. Numerical aperture (NA) is the measure of the objective lens's ability to collect light and resolve fine features and is defined as the angle of collection cone.

$$NA = n \sin \theta$$

Where n is the refractive index and θ is the half cone angle. The highest theoretical numerical aperture achievable is 1.51, with an immersion oil of refractive index $n=1.51$. In a diffraction limited system, NA determines the size of the airy disk pattern formed by imaging a point source through the objective lens. Resolution, the smallest resolvable distance between two objects, is defined by Rayleigh's criterion as:

$$R = \frac{0.61\lambda}{NA}$$

where λ is the wavelength. Resolution limit for 0.4 NA objective lens (20 \times) will be 850 nm for mid-spectrum wavelength of 550 nm and 240 nm for 1.4 NA 100 \times oil immersion lens. In the digital images, the detector needs to sample the images at high enough spatial sampling rate in order to achieve the full resolution capabilities of a microscope. According to the Nyquist sampling theorem, projected airy disk pattern should fit at least two detector pixels. Thus, for a 0.4-NA 20 \times objective lens with the 850 nm resolution limit, the projected airy disk size will be 17 μm , and the detector pixels should be smaller than 8.5 μm .

In conventional microscopes, the higher NA objective lens indicates higher magnification, smaller field-of-view (FOV) and smaller depth-of-focus. When imaged through an eyepiece, the FOV size is determined by the objective magnification and the field-number (FN) of the eyepiece, which typically ranges between 18-26 mm. In the digital images, size of the detector (CCD or CMOS image sensor) limits the FOV sizes. Typically for a 20 \times objective lens, the eyepiece of FN=22 will provide the FOV diameter of 1.1 mm and the detector FOV with a 2/3-inch image sensor (11 mm-diagonal) will be 0.55 mm (diagonal)[2]. The complex relationships between the NA, resolution, FOV and DOF makes it challenging to increase the FOV without sacrificing the resolution. For a large FOV, applications such as whole-slide scanners in digital pathology, precision mechanical stages are used for 2-dimensional scanning and autofocusing of the sample, which further increases the system cost.

Objective lenses for microscopy have continuously evolved into more complex form to provide higher NA and better correction for optical aberrations arising from the interaction of light with glass lenses[3]. Modern microscope objectives can correct for most aberrations, thanks to added complexity in lens systems and advanced manufacturing techniques. However, as the number of lens elements in an objective lens increases, so does the cost. High cost and large size of the microscopes result from the use of complex objective lens for magnification of the images. Changes in the fundamental design of microscopes is needed in order to achieve cost reduction and miniaturization of microscopy without loss of imaging performance.

1.2. Modern Lensless Microscopy techniques

There is a growing interest in low-cost miniaturized microscopy systems for biomedical research, point-of-care analysis and field diagnostics. A portable miniature microscope, produced at

scale at existing semiconductor foundries and capable of imaging blood cell or parasite morphology in high resolution, would bring affordable healthcare diagnostics to less developed populations in rural settings, where it is too costly to deploy expensive conventional microscopes and skilled technicians. In order to achieve this goal, various imaging strategies that remove objective lenses have been demonstrated. Lensless imaging strategies may not only reduce the size and the cost of the systems, but also bypass inherent limitations of lenses, such as optical aberrations and the trade-off between the resolution and the field-of-view.

In recent years, two classes of on-chip microscopy methods have been extensively reported to address these needs. The first method, optofluidic microscopy (OFM)[4-9], scans target objects across an aperture array using a microfluidic flow. The second method, inline holography [10-14], computationally renders images of target objects from interferometry measurements of the objects' scattered light field. Both methods achieve resolutions better than the sensor pixel size, but each has its respective strengths and tradeoffs. In addition to digital inline holography and OFM, a shadow imaging method based on direct contact of the sample and the detector has also been demonstrated [15, 16]. In this Section, we will review these lensless imaging techniques in detail.

1.2.1 Digital Inline holography

The concept of in-line holography was first proposed by Gabor[10] in 1948, with a simple set up composed of a spherical-wave illumination, the sample, and the detector. The interference pattern between the unscattered reference wave and the wave scattered by the sample is used to reconstruct the wavefront at the object plane. With the development of high-resolution digital image sensors, digital hologram recording and the numerical reconstruction method has been developed, yielding a new tool for biological microscopy that simplifies the conventional microscopes and overcomes the limitation of lenses[11, 17].

In a typical digital inline holographic microscopy set-up, a coherent light source in combination with a small pinhole, is used to create a spherical wave that illuminates the object. The magnified diffraction pattern is projected onto the detector array placed farther away from the object. The reconstruction process yields both the intensity and the phase image of the object. The resolution in digital inline holography is directly related to size and position of the image sensor, the SNR of the captured hologram and the sensor's pixel size, dynamic range and the pixel density. The digital inline

holography approach works well with samples prepared on glass slides and represents a good direct alternative to conventional microscopy.

Due to the simplicity of the set-up, compact imaging systems based on digital inline-holography has been extensively reported recently [12, 13, 18]. Compact inline holography set-up is achieved by reducing the distance between the sample and the detector, where loss of hologram resolution due to reduced magnification is mitigated by computationally improving hologram images with pixel super-resolution algorithm. However, the holographic reconstruction based on iterative phase retrieval algorithm relies on the priori knowledge of the object in order for the solution to converge more rapidly [19, 20]. Thus, the reconstruction method does not work well with contiguously connected samples at high density. Multiple holographic measurements at varying distances between the sample and the detector has been used to recover images of highly confluent samples[21], with the expense of increased computational burden for the reconstruction process.

1.2.2 Optofluidic Microscopy

The concept of optofluidic microscopy (OFM) was first proposed and demonstrated by Heng *et al.*[22], and Cui *et al.*[4]. OFM achieves a chip-scale lensless imaging based on the combination of microfluidics and the near-field scanning imaging, by mounting a microfluidic channel directly on the image sensor pixel array with sub-micron apertures. The specimen flowing in the microfluidic channel is translated over the aperture array on an image sensor, at which the light transmission through the biological sample is collected (Figure 1 - 2a). OFM scheme achieves high resolution lensless imaging by exploiting the time domain in the acquisition process. In this case, the optical resolution is determined by the size of the apertures fabricated on the image sensor pixels, and the highest sharpness is achieved at the floor of the microfluidic channel [4, 23]. The use of microfluidic channel greatly simplifies the sample scanning step. Instead of mechanical raster scanning, OFM uses a long linear aperture array and the microfluidic channel aligned with a small tilt angle with respect to the sensor's pixel grid to achieve full x-y scanning without complex scanning systems. Also, it works directly with fluid samples and has the potential for integration with streamlined and high throughput microfluidic systems. Color imaging can be achieved by using color CMOS image sensors with apertures fabricated on RGB pixels[6].

The second generation of OFM utilizes diffractive optical elements to create an array of focused light spots within the microfluidic channel, through which the samples is scanned[9, 24]. This scheme

allows for fluorescence imaging with the resolution determined by the size of the illumination focal spot created by the Fresnel zone plates (FZP)[9]. The scanning-based strategy is identical to that of an aperture-based OFM, except that the light collection is more efficient and the plane of highest imaging acuity is at the focal plane of the FZPs, which can be predesigned. For fluorescence imaging, an absorptive color filter layer is coated on top of the image sensor to reject the background excitation light.

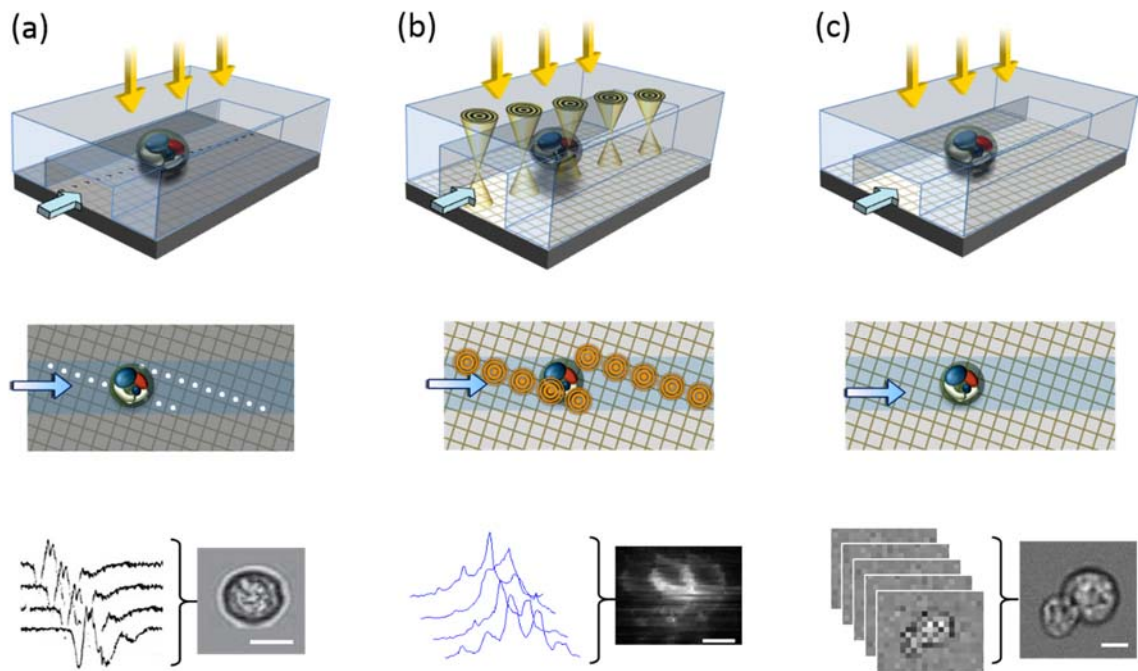


Figure 1 - 2. Schematic diagram of different generations of optofluidic microscopy systems. (a) Aperture-based OFM uses multiple line scans of sample collected through a small aperture on the pixel of the image sensor. (b) FZP-OFM is based on the line scans by the focused illumination created by diffractive optical elements mounted on the microfluidic channel. (c) Sub-pixel resolving OFM, which will be discussed later in this theses uses multiple direct shadow images and computational image processing to obtain high resolution images.

1.2.3 Shadow imaging

Another simple approach for lensless imaging is to directly couple the sample of interest with the image sensor [15, 25, 26]. When the specimen is placed in contact with the pixel array of the image sensor and illuminated, the direct shadow created by the sample can be collected at the photodiode of each pixel. This imaging scheme is often referred to as contact imaging, or shadow imaging. The illumination is often absorbed, scattered or refracted by the sample, which results in

reduced or increased signal at each pixel underneath the sample[15]. For luminescent samples, emitted light can be directly captured by the sensor [26].

In this scheme, the imaging resolution is limited to the twice the pixel size of the sensor, as defined by the Nyquist theorem. Considering that the size of the pixels in the image sensors are in the orders of micrometers, the resolution in direct shadow imaging is yet to compete with the sub-micron resolutions achieved with conventional microscopy. Also, the image quality is dependent on the contrast of the sample and the distance between the sample and the detector [16]. One unique advantage of contact imaging is the high collection efficiency due to the very short distance between the sample and the detector. In an ideal case, the contact imaging system can collect light from solid angle of 2π , which corresponds to collection efficiency of 50% for light emitting samples[16].

1.3 CMOS image sensors for lensless microscopy

The lensless microscopy techniques discussed in the previous Section all utilize a simple configuration; an illumination, sample and a detector. A complementary metal-oxide semiconductor (CMOS) image sensor constructs a crucial component of these imaging systems, which detects the light field generated by the sample.

The advances in CMOS image sensor technology has been a major driving force for the development of low cost chip-scale microscopes. Solid state image sensors were first developed in 1960, in the form of a two dimensional array of photodetecting pixels, which convert incident photons into photoelectrons. Charge coupled device (CCD) type devices have traditionally been more dominant in the market due to higher sensitivity and less noise during the charge-transfer readout scheme, until CMOS type active pixel sensors (APS) were developed and scaled down[27, 28]. CMOS APS type devices include multiple transistors in each pixel for in-pixel charge conversion, amplification and memory-like readout[29]. The readout scheme of CMOS image sensors allow for high speed readout with flexible region-of-interest at low power consumption. Also, due to the compatibility with standard MOS fabrication technologies, CMOS APS technology can easily be integrated with other functionalities, which further reduces the size and the cost[28, 29].

Pixel sizes in CMOS sensors have shrunk dramatically over the last decade as the CMOS process has scaled down. Smaller pixels allow for smaller imaging module with higher imaging resolution at lower material cost. However, small pixels also results in smaller “bucket” for collecting photons, which results in lower dynamic range and signal-to-noise ratio[30, 31]. In addition, as the

pixel size shrinks down, fill factor, the area percentage of the photodiode within each pixel, also reduces due to the fixed amount of area required for transistors and interconnects. Reduced fill factor can be corrected by the addition of a microlens array layer, which focuses light onto the photodiode region of each pixel and thereby increases the effective fill factor. Innovations in the pixel structures, such as stack reduction, light pipes, and backside illumination geometry, lead to further improvement in the fill factor, quantum efficiency and optical cross-talk[32-34]. State-of-the art low-cost CMOS image sensors for mobile imaging applications typically employ pixel sizes smaller than $2\ \mu\text{m}$, even reaching sub-micron pixels. This is almost an order of magnitude reduction from the first generation of commercial CMOS APS sensors.

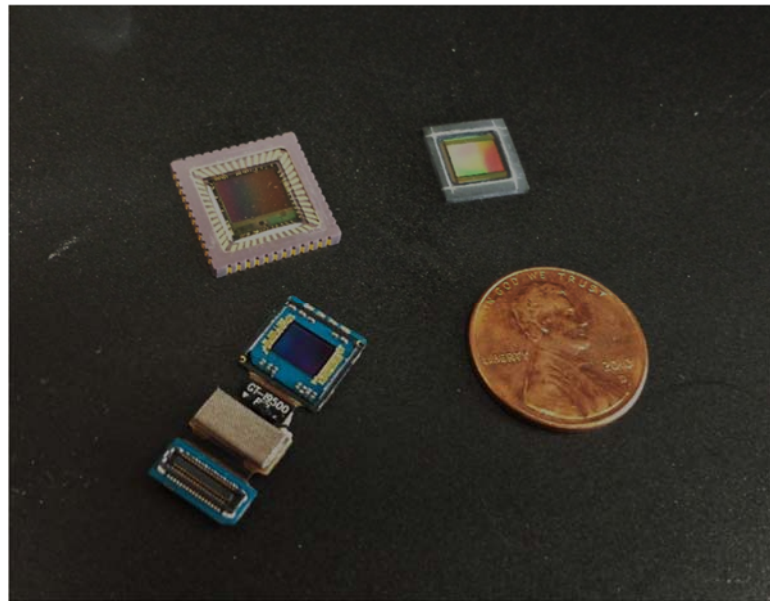


Figure 1 - 3. CMOS image sensors with different optical formats. Top Aptina $5.2\text{-}\mu\text{m}$ 1.3 Megapixel sensor with 1280×1024 pixels (top left), Aptina $2.2\text{-}\mu\text{m}$ 5 Megapixel sensor with 1944×2592 pixels (top right) and Samsung $1.12\text{-}\mu\text{m}$ 12 Megapixel sensor with 4208×3120 pixels mounted on a interconnect module (bottom left).

1.4 Organization of this thesis

This thesis presents construction of bright-field and fluorescence chip-scale microscopes based on lensless imaging using low-cost CMOS image sensors. Our approach for bright-field chip-scale microscope is to apply computational image processing technique to improve the resolution of direct shadow imaging. We also demonstrate fluorescence capabilities of chip-scale microscopes, where we focus on the fluorescence collection geometry at the image sensor for construction of compact and low-cost fluorescence imaging system.

Four versions of bright-field microscopes will be presented throughout Chapter 2 to 5, based on different strategies for image acquisition and the types of the samples. In Chapter 2, we first discuss the use of pixel super-resolution reconstruction for resolution enhancement in chip-scale microscopy. Then, the sub-pixel resolving optofluidic microscopy will be introduced as a new version of OFM, which uses microfluidic scanning of sample for image reconstruction. In Chapter 3, we will demonstrate a chip-scale microscope for imaging motile microorganisms, where we use the inherent motion of the microorganisms to perform pixel super-resolution reconstruction. Here, we will also introduce the concept of ePetri, which is a compact imaging system for long-term monitoring of live cells. Then, in Chapter 4, we discuss the construction of sweeping-illumination ePetri system for imaging static objects and the application of our prototype system for waterborne parasite detection. Chapter 5 presents a smart-phone based chip-scale microscopy using ambient illumination, targeted for portable imaging applications.

Fluorescence version of our chip-scale microscope will be presented in Chapter 6. We will first demonstrate the low-resolution fluorescence imaging using absorptive filter-coated image sensors. We then discuss the design and fabrication of silo-filter CMOS sensors, a new pixel design which compensates for resolution loss in fluorescence contact imaging.

BIBLIOGRAPHY

1. Davidson, M.W. and M. Abramowitz, *Optical Microscopy*, in *Encyclopedia of Imaging Science and Technology*. 2002, John Wiley & Sons, Inc.
2. Kenneth R. Spring, T.J.F.a.M.W.D. *Introduction to Charge-Coupled Devices (CCDs)*.
3. Bennett, A.H., *The Development of the Microscope Objective*. Journal of the Optical Society of America, 1943. **33**(3): p. 123-123.
4. Cui, X., L. Lee, X. Heng, W. Zhong, P. Sternberg, D. Psaltis, and C. Yang, *Lensless high-resolution on-chip optofluidic microscopes for Caenorhabditis elegans and cell imaging*. Proceedings of the National Academy of Sciences, 2008. **105**(31): p. 10670.
5. Lee, L., X. Cui, and C. Yang, *The application of on-chip optofluidic microscopy for imaging Giardia lamblia trophozoites and cysts*. Biomedical Microdevices, 2009. **11**(5): p. 951-958.
6. Pang, S., X. Cui, J. DeModena, Y.M. Wang, P. Sternberg, and C. Yang, *Implementation of a color-capable optofluidic microscope on a RGB CMOS color sensor chip substrate*. Lab on a Chip, 2010. **10**(4): p. 411-414.
7. Zheng, G., S.A. Lee, S. Yang, and C. Yang, *Sub-pixel resolving optofluidic microscope for on-chip cell imaging*. Lab on a Chip, 2010. **10**(22): p. 3125-3129.
8. Lee, S.A., R. Leitao, G. Zheng, S. Yang, A. Rodriguez, and C. Yang, *Color Capable Sub-Pixel Resolving Optofluidic Microscope and Its Application to Blood Cell Imaging for Malaria Diagnosis*. PLoS ONE, 2011. **6**(10): p. e26127.
9. Pang, S., C. Han, L.M. Lee, and C. Yang, *Fluorescence microscopy imaging with a Fresnel zone plate array based optofluidic microscope*. Lab on a Chip, 2011. **11**(21): p. 3698-3702.
10. Gabor, D., *A new microscopic principle*. Nature, 1948. **161**(4098): p. 777-778.
11. Xu, W., M. Jericho, I. Meinertzhagen, and H. Kreuzer, *Digital in-line holography for biological applications*. Proceedings of the National Academy of Sciences of the United States of America, 2001. **98**(20): p. 11301.
12. Bishara, W., T. Su, A. Coskun, and A. Ozcan, *Lensfree on-chip microscopy over a wide field-of-view using pixel super-resolution*. Optics Express, 2010. **18**(11): p. 11181-11191.
13. Seo, S., T. Su, D. Tseng, A. Erlinger, and A. Ozcan, *Lensfree holographic imaging for on-chip cytometry and diagnostics*. Lab on a Chip, 2009. **9**(6): p. 777-787.
14. Su, T.-W., A. Erlinger, D. Tseng, and A. Ozcan, *Compact and Light-Weight Automated Semen Analysis Platform Using Lensfree on-Chip Microscopy*. Analytical Chemistry, 2010. **82**(19): p. 8307-8312.
15. Honghao, J., P.A. Abshire, M. Urdaneta, and E. Smela. *CMOS contact imager for monitoring cultured cells*. in *Circuits and Systems, 2005. ISCAS 2005. IEEE International Symposium on*. 2005.
16. Honghao, J., D. Sander, A. Haas, and P.A. Abshire, *Contact Imaging: Simulation and Experiment*. Circuits and Systems I: Regular Papers, IEEE Transactions on, 2007. **54**(8): p. 1698-1710.
17. Garcia-Sucerquia, J., W. Xu, M. Jericho, and H. Kreuzer, *Immersion digital in-line holographic microscopy*. Optics letters, 2006. **31**(9): p. 1211-1213.
18. Bishara, W., U. Sikora, O. Mudanyali, T.-W. Su, O. Yaglidere, S. Luckhart, and A. Ozcan, *Holographic pixel super-resolution in portable lensless on-chip microscopy using a fiber-optic array*. Lab on a Chip, 2011. **11**(7): p. 1276-1279.
19. Koren, G., F. Polack, and D. Joyeux, *Iterative algorithms for twin-image elimination in in-line holography using finite-support constraints*. Journal of the Optical Society of America A, 1993. **10**(3): p. 423-433.

20. Fienup, J.R., *Reconstruction of an object from the modulus of its Fourier transform*. Optics Letters, 1978. **3**(1): p. 27-29.
21. Greenbaum, A., U. Sikora, and A. Ozcan, *Field-portable wide-field microscopy of dense samples using multi-height pixel super-resolution based lensfree imaging*. Lab on a Chip, 2012. **12**(7): p. 1242-1245.
22. Heng, X., D. Erickson, L. Baugh, Z. Yaqoob, P. Sternberg, D. Psaltis, and C. Yang, *Optofluidic microscopy --- method for implementing a high resolution optical microscope on a chip*. Lab on a Chip, 2006. **6**(10): p. 1274-1276.
23. Wang, Y.M., G. Zheng, and C. Yang, *Characterization of acceptance angles of small circular apertures*. Optics Express, 2009. **17**(26): p. 23903-23913.
24. Lee, L.M., *The implementation of optofluidic microscopy on a chip scale and its potential applications in biology studies*, in *Bioengineering*. 2012, California Institute of Technology.
25. Moscelli, N., S. van den Driesche, W. WitarSKI, S. Pastorekova, and M.J. Vellekoop, *An imaging system for real-time monitoring of adherently grown cells*. Sensors and Actuators A: Physical, 2011. **172**(1): p. 175-180.
26. Beiderman, M., T. Tam, A. Fish, G.A. Jullien, and O. Yadid-Pecht, *A Low-Light CMOS Contact Imager With an Emission Filter for Biosensing Applications*. Biomedical Circuits and Systems, IEEE Transactions on, 2008. **2**(3): p. 193-203.
27. Ohta, J., *Smart CMOS image sensors and applications*. 2010: CRC Press.
28. Fossum, E.R., *CMOS image sensors: electronic camera-on-a-chip*. Electron Devices, IEEE Transactions on, 1997. **44**(10): p. 1689-1698.
29. El Gamal, A. and H. Eltoukhy, *CMOS image sensors*. Circuits and Devices Magazine, IEEE, 2005. **21**(3): p. 6-20.
30. Tian, H., *Noise analysis in CMOS image sensors*. 2000, Stanford University.
31. Chen, T., P.B. Catrysse, A. El Gamal, and B.A. Wandell. *How small should pixel size be?* in *Electronic Imaging*. 2000. International Society for Optics and Photonics.
32. Agranov, G., R. Mauritzson, J. Ladd, A. Dokoutchaev, X. Fan, X. Li, Z. Yin, R. Johnson, V. Lenchenkov, and S. Nagaraja. *Pixel continues to shrink, pixel development for novel CMOS image sensors*. in *Proceedings of the 2009 International Image Sensor Workshop*. 2009.
33. Fontaine, R., *The Evolution of Pixel Structures for Consumer-Grade Image Sensors*. Semiconductor Manufacturing, IEEE Transactions on, 2013. **26**(1): p. 11-16.
34. Fontaine, R. *Recent innovations in CMOS image sensors*. in *Advanced Semiconductor Manufacturing Conference (ASMC), 2011 22nd Annual IEEE/SEMI*. 2011.

SUB-PIXEL RESOLVING OPTOFLUIDIC MICROSCOPE (SROFM)

In this chapter, we report on the implementation of a sub-pixel resolving optofluidic microscope (SROFM) by applying pixel super-resolution algorithms in a new and simplified OFM scheme. We first give an overview of the entire imaging scheme, and then define in detail some of the more critical hardware design requirements and image processing techniques used, including methods for sub-pixel-shift estimation and a shift-and-add pixel super-resolution algorithm. We then present SROFM images of various biological samples, including various different three-dimensional projections of rotating objects and characterize the resolution limit of SROFM. Next, we show color imaging capabilities of SROFM using switching RGB illumination. We implement this color SROFM for high-throughput imaging of stained blood sample, for detection of malaria infection. Finally, we conclude with a discussion on possible biomedical and bioscience applications for SROFM.

2.1 Imaging principle

2.1.1 Pixel super-resolution reconstruction

In digital imaging, the image resolution depends on the physical layout of the camera – both the optical arrangements and the detector elements. “High-resolution” often indicates that the pixel density within a digital image is high, therefore revealing more details of the original view. The image capturing process can be modeled as low-pass filtering of the original analog image by the imaging system’s point-spread-function (PSF) followed by the down-sampling process by the detector’s pixel sizes and some additive noises. Increasing the image resolution can be achieved by improving the lens system and the detector, with the expense of the cost and size of the camera system.

As an alternative approach, signal processing techniques have been developed to enhance the resolution of digital images by using multiple frames of low-resolution images. These methods are referred to as “super-resolution reconstruction”, “multiframe super-resolution” and “pixel-super resolution.” In this thesis, we will use the term “pixel super-resolution reconstruction” in order to avoid confusion with the super-resolution microscopy techniques discussed in Section 1.2.1. The pixel-super resolution technique was first introduced in the 1980s[1] and since then, numerous algorithms have been proposed [2-4]. In general, pixel super-resolution approaches rely on combining information from multiple sub-pixel-shifted low resolution (LR) images to create a single high

resolution (HR) image. Effectively, pixel super-resolution approaches take advantage of over-sampling in the time domain (capturing a sequences of images rather than a single image) to compensate for under-sampling in the spatial domain, for which the resolution is limited by the image sensor pixel size. The major advantage of this approach is that it can utilize the existing imaging systems, thus achieving resolution improvement with low cost. To capture such a sequence of shifted LR images, either a fixed detector could image a spatially translating object, or a translating detector or multiple detectors could image a fixed object. In either case, the success of the applied pixel super-resolution algorithm for HR image restoration depends critically on the precise control over and knowledge of the relative sub-pixel shifts between subsequent LR images.

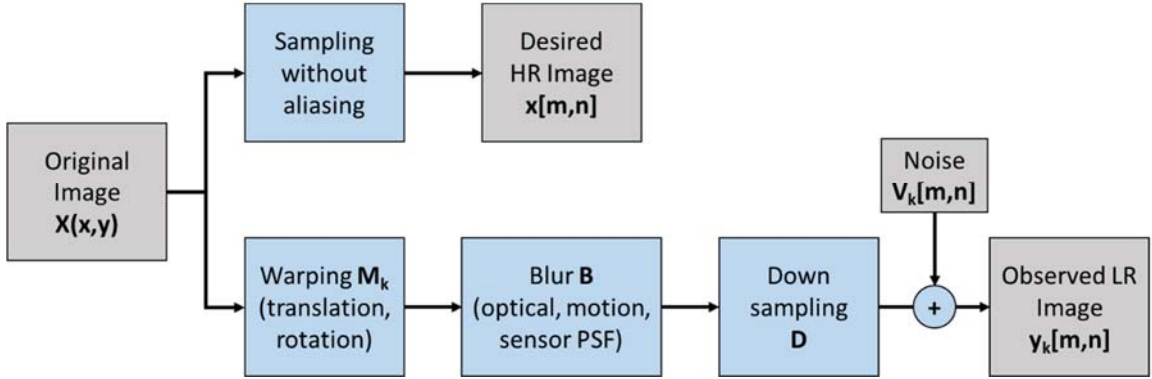


Figure 2 - 1. Block diagram representation of the image acquisition model in pixel super-resolution reconstruction process.

The image reconstruction algorithm can be analyzed by constructing an observation model. The image observation model can be represented as Figure 2 - 1. We will use matrix notations to represent the images in the pixel domain as commonly used in general pixel super-resolution models. Desired HR image of size $[mL \times mL]$ is written in lexicographical notation as the vector \mathbf{x} of size $[m^2L^2 \times 1]$. The k^{th} LR image, denoted in lexicographic notation as \mathbf{y}_k of size $[L^2 \times 1]$ can be obtained by warping, blurring and down sampling the HR image \mathbf{x} .

$$\mathbf{y}_k = \mathbf{D}\mathbf{B}_k\mathbf{F}_k\mathbf{x} + \mathbf{V}_k \quad \text{for } k = 1, \dots, N. \quad (2,1)$$

Matrix \mathbf{F}_k is the warp matrix of size $[M^2L^2 \times M^2L^2]$, \mathbf{B}_k is the blur matrix of size $[M^2L^2 \times M^2L^2]$, \mathbf{D} represents the decimation matrix of size $[L^2 \times M^2L^2]$ and \mathbf{V}_k represents a lexicographically ordered noise vector of size $[L^2 \times 1]$. M is the resolution enhancement factor,

which denotes the factor of reduction in the physical dimension of the pixels between the LR and HR images.

In most cases, the noise is assumed to be white, which means the auto-correlation of the noise $E\{V_k V_k^T\} = \sigma^2 I$. Also, considering the case of single camera system without motion blur, all the blur operations can be assumed to be the same, i.e., $\forall k, B_k = B$. Both B and F_k can be assumed to be block circulant matrices, representing a linear space invariant blur and a purely translational warp operations, thus being commutative. The Maximum-Likelihood estimation of \mathbf{x} can be done by solving following least-squares expression.

$$\hat{\mathbf{x}} = \text{ArgMin}\{\sum_{k=1}^N [\mathbf{y}_k - DBF_k \mathbf{x}]^T [\mathbf{y}_k - DBF_k \mathbf{x}]\} \quad (2,2)$$

Taking the first derivative of above equation with respect to \mathbf{x} and equating to zero, we can obtain \mathbf{x} from solving the linear system of

$$RB\hat{\mathbf{x}} = P \quad (2,3)$$

Where $R = \sum_{k=1}^N F_k^T D^T D F_k$ and $P = \sum_{k=1}^N F_k^T D^T \mathbf{y}_k$. Since D is a decimation matrix, $D^T D$ is a diagonal matrix. Also, F_k represents a translational warp, thus each column in F_k will have value of 1 at the corresponding displacement position and 0 elsewhere (the same for each row of F_k^T). The matrix $F_k^T D^T D F_k$ will have non-zero values only at the main diagonal entries, and thus R becomes invertible. Each diagonal entry of R corresponds to one pixel in the super-resolution image and the vector P is simply the addition of low resolution measurements after interpolation and motion compensation. The computation for R and P is basically a shift-and-add process based on the known sub-pixel shifts of each LR frame. High resolution image $\hat{\mathbf{x}}$ can be computed from deconvolving $R^{-1}P$ with the blur matrix B , which can be the more demanding part in terms of computation.

2.1.2 Microfluidic scanning for pixel super-resolution reconstruction

Pixel super-resolution algorithm is a compelling technique for resolution improvement in lensless imaging techniques, where the pixel size of the detector limits the imaging resolution. Recently, Bishara *et al.* combined inline holography with the pixel super-resolution approach to effectively shrink their image pixel size and thereby attain higher resolution images[5]. Interestingly, not only is this pixel super-resolution approach adaptable for use in OFM and shadow imaging as

well, but it also greatly simplifies the microscopy scheme. More specifically, the microfluidic flow of the samples across the sensor suffices for generating sub-pixel shifts and precludes the need for an additional precision scanning setup. Furthermore, the resolution enhancement provided by the aperture arrays employed in current OFM system can be replaced by the enhancement provided by applying the pixel super-resolution algorithm. Without the aperture arrays, the OFM would be an even simpler on-chip microscopy design, consists solely of a microfluidic channel emplaced upon a commercial 2D sensor chip. We will refer to this technique as “sub-pixel resolving optofluidic microscopy (SROFM)” from here on.

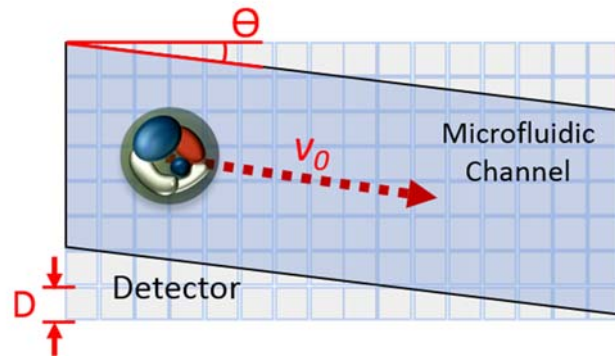


Figure 2 - 2. Sub-pixel scanning of images by microfluidic channel mounted on top of the image sensor.

For 2D scanning of a sample, microfluidic channel can be mounted on the image sensor surface with a small angle θ with respect to the pixel grid. Assuming all pixels are identical, for an object flowing in the microfluidic channel with a velocity of v_0 , the sub pixel shift between each frame can be denoted as below

$$d_x = \frac{v_0 \cos \theta}{Df} - \left\lfloor \frac{v_0 \cos \theta}{Df} \right\rfloor, \quad d_y = \frac{v_0 \sin \theta}{Df} - \left\lfloor \frac{v_0 \sin \theta}{Df} \right\rfloor \quad (2,4)$$

where D is the pixel size of the detector and f is the frame rate of the detector. For N frames, the sample has to be shifted at least one pixel in both direction, yielding

$$\frac{v_0 \sin \theta}{Df} > 1 \quad (2,5)$$

Also, the channel alignment angle θ should be carefully chosen such that the sub-pixel shifts over N frames ($[d_{x,k}, d_{y,k}], k = 1, \dots, N$) show uniform distribution over $[0, 1]$ interval. Typically, if the channel is aligned to integer number of pixels in x and y direction, that is, $\tan \theta = k/l$, where k and l are integers smaller than \sqrt{N} , the corresponding sub-pixel motion vector will likely overlap with other frames.

Figure 2 - 3 shows simulated sub-pixel shifts of linearly scanned object with different channel alignment angles. Flow velocity of $v_0 = 500 \mu\text{m/s}$, frame rate $f = 800 \text{ fps}$, pixel size $D = 2.2 \mu\text{m}$ and total number of frame $N = 100$ was used. Frame number k of each $[d_{x,k}, d_{y,k}]$ pair is marked in the plots as the label. When θ is too small, the sample does not scan enough through y direction (Figure 2 - 3 Left). At $\theta = 10^\circ$, $[d_{x,k}, d_{y,k}]$ show uniform distribution within the pixel space. At $\theta = 26.5^\circ$ where $\tan \theta = 1/2$, $[d_{x,k}, d_{y,k}]$ values are repeated, yielding an undesirable motion vector.

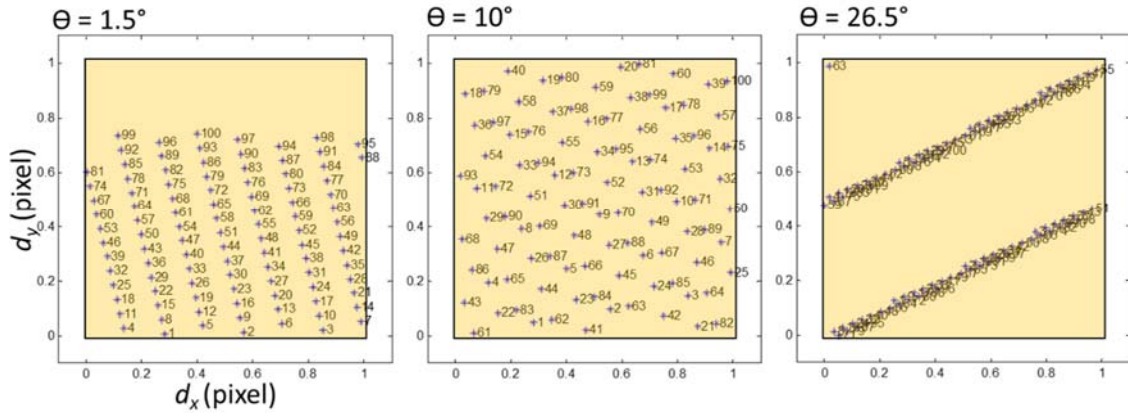


Figure 2 - 3. Sub-pixel shifts of microfluidically scanned object with different channel alignment angles. When the angle is too small, the sample does not scan enough through y direction (Left). At $\theta = 26.5^\circ$ where $\tan \theta = 1/2$, $[d_{x,k}, d_{y,k}]$ values are repeated, yielding an undesirable motion vector. Flow velocity of $v_0=500 \mu\text{m/s}$, frame rate $f=800\text{fps}$, pixel size $D=2.2 \mu\text{m}$ and total number of frame $N=100$ was used.

2.1.3 Fundamental limits of sub-pixel resolving optofluidic microscopy

It is worthwhile to consider the fundamental limits of resolution improvement in SROFM on pixel super-resolution reconstruction. The optical resolution in pixel super-resolution reconstructed images depend on the resolution of the low-resolution sequence, the enhancement factor used in the reconstruction and the precision of image registration. It has been shown that there exist fundamental limits to actual improvement in image resolution with the increasing enhancement factor [6, 7]. Lin

and Shum [7] have stated that the resolution improvement limit was $m = 5.7$ for an ideal case with noise-free images and perfect registration. In this study, the limit of enhancement factor, beyond which the resolution of the reconstructed image is more or less the same, is derived from analyzing the deviation of reconstructed high resolution image from the real solution, which was estimated via applying the perturbation theorem. For simplification of the problem, they assumed unlimited number of LR images, the detector has pixel fill factor of 1 with the pixel PSF of a box function and the sub-pixel shifts was limited to translational movement. In reality, the resolution improvement limit is also governed by complex relationships between the reconstruction algorithm, imaging system's PSF, measurement SNR, detector's nonlinearity and dynamic range, nature of motion and the image content[7-9].

Another important factor in determining the resolution limit of SROFM is the degradation of the direct shadow images due to finite distance between the sample and the detector surface. In aperture-based OFM, the resolution degradation over increased distance (H) from the image sensor was characterized by measuring the PSF associated with the individual aperture with a near field scanning microscope tip as a point source [10]. It was shown that for a 1- μm aperture, the resolution degrades from 0.9 μm at $z = 0.1 \mu\text{m}$ to 3 μm at $z = 2.5 \mu\text{m}$. For shadow images, the contrast of the shadow will degrade as the sample moves away from the surface of the image sensors due to diffraction. Ji *et al.*[11] have used ray tracing simulations and experimental verifications to show that the contrast of shadow images degrades and the blurring at the edges of the object increases as the sample to detector distance increases.

In consideration of these two factors, we can construct a model of the image acquisition process of SROFM based on pixel super-resolution reconstruction of shadow images (Figure 2 - 1). The original image of the sample $\mathbf{x}(x, y)$ will be blurred by the optical blur function $\mathbf{w}(x, y, z)$ at distance z between the sample and the detector. The shadow image at the plane of the image sensor can be expressed as a convolution between the sample image and the blur function. The image sensor has unique pixel function, which we denote as $\mathbf{a}(x, y)$. The k^{th} LR frame with motion vector $\mathbf{d}_k = [d_{x,k}, d_{y,k}]$ can be expressed as

$$\mathbf{y}_k(\mathbf{m}) = \int_{\mathbf{y}_k} \mathbf{x}_z(\mathbf{r}) \cdot \mathbf{a}(\mathbf{r} - \mathbf{m} + \mathbf{d}_k) d\mathbf{r} \quad (2,6)$$

where shadow image at distance z is $\mathbf{x}_z(\mathbf{r}) = \mathbf{x}(\mathbf{r}) * \mathbf{w}(\mathbf{r}, z)$ ($\mathbf{r} = (x, y) \in \mathbf{R}^2$ and $\mathbf{m} = [m, n] \in \mathbf{Z}^2$). At $z = 0$, the blur function $\mathbf{w}(\mathbf{r}) = \delta(\mathbf{r})$. In the simplest case, we can assume the pixel function $\mathbf{a}(x, y)$ to be a rectangular function with width of S , which is the square root of the fill factor of the image sensor pixel.

$$\mathbf{a}(x, y) = \begin{cases} S^{-2}, & |x|, |y| \leq S/2 \\ 0, & \text{otherwise} \end{cases} \quad (2,7)$$

In reality, the pixel function varies with the architecture of the CMOS sensors and can be experimentally measured or estimated as a 2D Gaussian function[12].

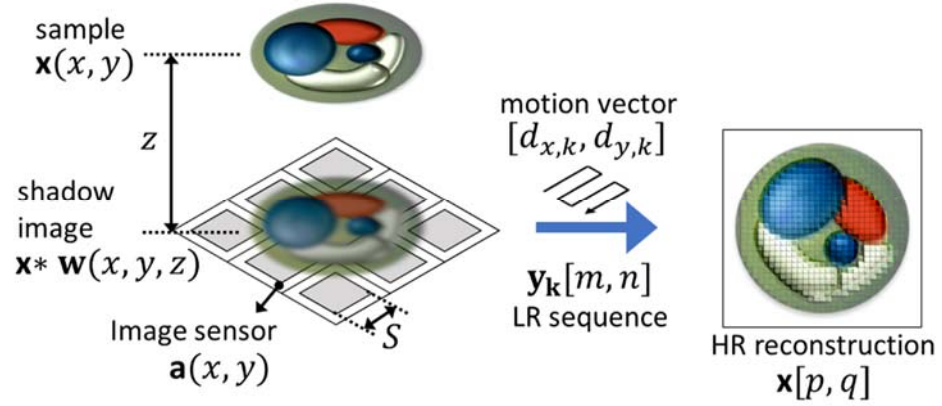


Figure 2 - 4. Schematic diagram of SROFM image acquisition model.

To determine the resolution limit of SROFM, we used numerical analysis to simulate the image acquisition process (Figure 2 - 4 and Figure 2 - 5). With a synthetic image $\mathbf{x}(x, y)$, we numerically computed the shadow image by applying angular spectrum method[13, 14] and computed the LR sequence $\mathbf{y}_k(m, n)$ from equation (2,6). We then reconstructed high resolution image $\mathbf{x}(p, q)$ with a magnification factor of M , where $\mathbf{p} = [p, q] = \frac{1}{M} \mathbf{m}$. We assumed the ideal raster scanning motion with $d_x = d_y = \frac{1}{M}$ of M^2 frames. The performance of reconstruction can be assessed with various methods depending on the type of images. With photography images, the performance of pixel super-resolution is typically measured by the amount of deviation from the real solution. In evaluating a photography system, the resolution can be measured by maximum spatial frequency components that can be resolved. Here, we used a line pair object as the sample image and evaluated the resolution

minimum line width that can be distinguished in the reconstructed high resolution image. With a set of parameters chosen to imitate our experimental settings, we can find a minimum resolvable line width, optimal enhancement factor and degradation of resolution over increasing sample height.

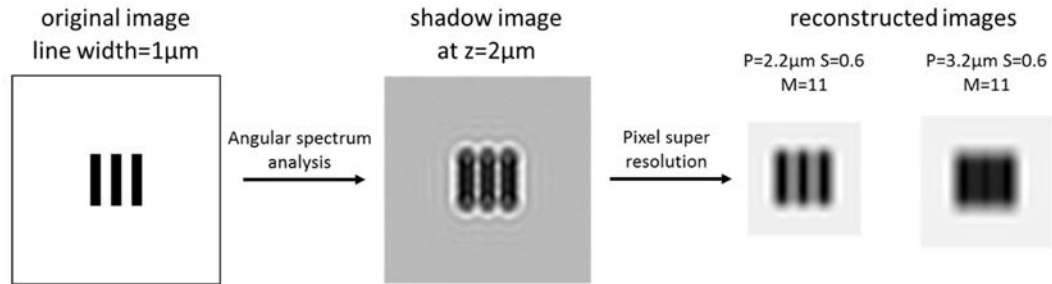


Figure 2 - 5. SROFM image acquisition with synthetic images. Original image of line pairs with line width l is propagated to sample height z via angular spectrum analysis. The resulting shadow images are digitally scanned over the image sensor and the corresponding low resolution sequence is processed with pixel super-resolution with varying parameters.

To determine the imaging resolution, we ran the simulation with line pair images of different line widths. In the reconstructed images, we took the summation of all pixel values in direction parallel to the line pattern to find the smallest line widths that can be resolved (Figure 2 - 6a,b). We experimented on the effect of the pixel size P , length portion of the photodiode in a pixel S , and the distance from the sample and the detector z . We assumed the light source is a white light with uniform spectrum within 400 nm to 700 nm. The enhancement factor M was fixed to 11. Figure 2 - 6c shows resolution limit obtained from our numerical analysis. The resolution can be explained in two regimes; with small z , the limit is determined by the physical layout of the image sensor. When the distance increases, resolution is limited by the blur of the shadow images. In small z regime ($z < 5\mu$ m in our case), smaller pixel and smaller fill factor yields higher resolution. Note that $[P, S]$ of $[3.2, 0.6]$ shows higher resolution than $[2.2, 1.0]$. This suggests that the actual size of the photodiode (PS) determines the resolution and the smaller photodiode size may be preferred in SROFM. As the sample moves further away from the detector, the resolution is determined by the resolution of the shadow image itself, regardless of the image sensor's physical layout.

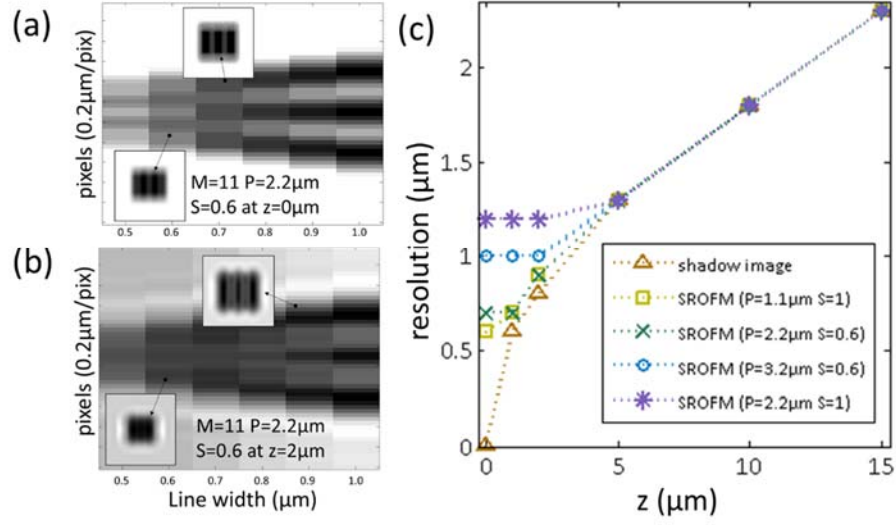


Figure 2 - 6. Resolution of SROFM. (a-b) Vertical summed pixel values of reconstructed images plotted over varying line pair widths. First line width that can be resolved into three dark lines are considered as the resolution limit. (c) Resolution with varying sample height, sensor's pixel size and fill factor.

In an ideal case where a sample of infinitesimal thickness is placed right on the image sensor, we can assume that the shadow image is unblurred ($\mathbf{w}(\mathbf{r}) = \delta(\mathbf{r})$) and is identical to the original image. For an ideal line object with line width of l ($\mathbf{x}(x) = \text{rect}\left(\frac{x}{l}\right)$, $l < S$), this problem can be simplified to 1D where image acquisition process becomes a convolution between two square functions. Shift-and-add reconstruction process with linear 1D scanning (sub-pixel shift $d_{x,k} = \frac{1}{M}k$) also becomes simple as below;

$$\mathbf{y}_k(x) = \int_{-0.5S}^{0.5S} \text{rect}\left(\frac{u}{S}\right) \text{rect}\left(\frac{x+u}{l}\right) du \quad (2,8)$$

$$\mathbf{y}_k[m] = \mathbf{x}[k + (m - 1)M] \quad (2,9)$$

Equation (2.8) is simply a trapezoidal function with the FWHM of $\max(S, l)$. In order to resolve two lines of the same width, the center-to-center distance of two lines, $2l$, has to be at least S . Thus, the minimum resolvable linewidth will be

$$R = \frac{SP}{2} \quad (2,10)$$

where P is the actual physical size of the pixel. The fill factor of small pixel image sensors are known to be less than 50%. From pixel structures published in literatures[15, 16], we choose $S = 0.6$ for a 2.2- μm pixel sensor. In this case, the smallest resolvable line pair width is 660 nm. This result agrees with the numerical analysis in Figure 2 - 6b. Note that this value is still an estimate, since the shape and the pitch of pixel function may vary and this analysis is restricted to line objects.

In order to resolve features at the size of $\frac{S}{2}$ LR pixels, size of the HR pixels ($\frac{1}{M}$ * LR pixel) has to satisfy the Nyquist criterion. Thus the enhancement factor should be

$$M > \frac{4}{S} \quad (2,11)$$

Since the resolution is limited to $\frac{S}{2}$ low-resolution pixels, increasing the enhancement factor beyond this value will not yield higher resolution in the resulting images.

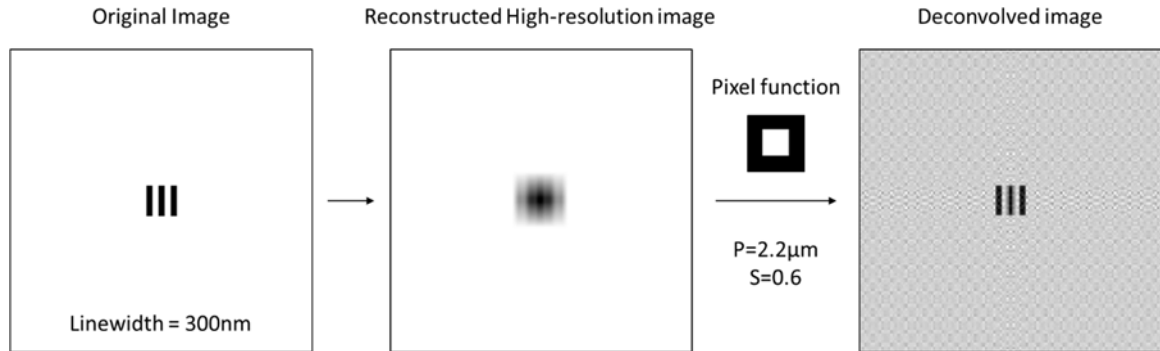


Figure 2 - 7. Deconvolution of images with pixel function yields sub-pixel resolution imaging beyond the pixel size limit.

However, this resolution limit can be overcome by simple deconvolution process (Figure 2 - 7). Since the imaging process is a 2D convolution between the shadow image and the pixel function, the shadow image can be reconstructed by deconvolving the obtained high resolution image with the pixel function $\mathbf{a}(x, y)$. In this case, we can resolve features that are far smaller than the pixel size. The resolution limit of the final images will be determined by the precision of the pixel function and

the noise. The pixel function of image sensors vary with the physical design of pixels in the different types of sensors. It can be obtained experimentally by near-field scanning methods, in which case the PSF of the near-field scanning microscopes would determine the precision of the pixel function. In the presence of noise, the image reconstruction is highly dependent on the deconvolution algorithm.

In actual SROFM, several other factors in the acquisition process may affect the image quality and worsen the resolution limit. First of all, the image registration with microfluidic scanning is not ideal as raster scanning. In our reconstruction algorithm, when the upsampled LR frames are shifted by the measured sub-pixel shift, we use bilinear interpolation for the sub-pixel shift values beyond the accuracy of high resolution pixel size ($\frac{1}{M}$). Although the bilinear interpolation provides better image registration than rounding the sub-pixel shifts to integer multiples of $\frac{1}{M}$, there exists artifacts and blur caused by the bilinear interpolation which further decreases the image quality. In addition, since microfluidic scanning is continuous, images can be blurred by the motion of sample during the camera exposure time. This motion blur can be reduced by decreasing the exposure time with higher illumination intensity and can be suppressed by motion deblurring processes [17]. Other motion artifacts, such as rotation and the errors in the motion estimation can be the source of image quality degradation. Also, a finite separation between the sample and the detector, whether in the form of the passivation layer of the detector, floating of the sample within the microfluidic channel or the thickness of the sample itself, causes the resulting images to be the “near field” of the sample which may vary from the image at the plane of focus within the sample as in conventional light microscopy. In addition, the realistic limitations can be exerted by the image sensor; noise, nonlinearity of the sensor response and limited dynamic range. These imperfections tends to get worse as the pixel size shrinks down [9, 15, 18], which may become a crucial trade-off in practical situations. The performance of SROFM, or other chip-scale microscopy techniques based on pixel super-resolution reconstruction, is the result of complex trade-offs between various parameters, artifacts and computations. Although the theoretical limits provide useful design parameters for constructing chip-scale microscopes, the actual resolution of the system that is determined experimentally, which will be discussed throughout this thesis, may serve as a more practical measure for the performance of our systems.

2.2 Construction of SROFM device

The SROFM technique involves flowing a sample within a microfluidic channel directly above the surface of a CMOS image sensor (Figure 2 - 8a). A sequence of pixel-size-limited LR direct-projection images of the sample, in which the sample within subsequent LR images is shifted by a sub-pixel amount, is captured and processed using the pixel super-resolution algorithm to produce a single HR image. The microscopy scheme is based on the OFM technique described in Section 1.2.2, except that it does not require a metal layer or an aperture array.

The SROFM sensor chip is compact, measuring approximately $1.5 \text{ cm} \times 1.5 \text{ cm}$ in size (Figure 2 - 8b), and consists of a polydimethyl-siloxane (PDMS) microfluidic channel of width between $50 \text{ }\mu\text{m}$ and $300 \text{ }\mu\text{m}$ and height between $5 \text{ }\mu\text{m}$ and $27 \text{ }\mu\text{m}$, with an inlet and an outlet hole, bonded directly to an inexpensive, commercially available CMOS image sensor. The color filter array and microlens array inherent in the sensor were removed via oxygen plasma cleaning at 150W for 10 min . Polydimethyl siloxane (PDMS) microfluidic substrate was fabricated by conventional soft lithography as described in ref.[19]. The PDMS channel was $50 \text{ }\mu\text{m}$ in width and $5.5 \text{ }\mu\text{m}$ in height, and was chemically treated with Poly-ethylene glycol(PEG) and UV exposure to render the surface hydrophilic, with the recipe described in ref [20]. We used two types of image sensors, Aptina MT9T001 and Aptina MT9P031 sensors, with the pixel sizes of $3.2 \text{ }\mu\text{m}$ and $2.2 \text{ }\mu\text{m}$, respectively. We designed the channel height to be just slightly larger than the dimensions of the samples being imaged to ensure the samples flowed as close as possible to the sensor's active sensing layer. The microfluidic channel was attached to the CMOS sensor at an angle between 10 to 30 degrees with respect to the rows of the CMOS pixel grid to ensure that the captured LR image sequence contained the necessary sub-pixel translations in both the x and y directions. Our choice of angle struck a balance between using a smaller angle with an imaging-area-of-interest with fewer pixel rows (and hence higher frame rate) and using a larger angle to obtain sufficient displacement along the y-direction with fewer frames. Our experiments were conducted under the light intensity of 1.2 W/m^2 (comparable to room light) provided by a conventional LED lamp and we employed a single frame exposure time of 0.3 ms .

For imaging, a liquid containing an adequate concentration of target objects is introduced into the channel from the inlet and the pressure difference between the inlet and outlet and the capillary action induce a flow, delivering the samples across the sensor pixel grid of the CMOS sensor. Samples were typically imaged at a flow velocity of $200 \text{ }\mu\text{m/s}$, with a frame rate of 500 fps and a field-of-view

(FOV) of $250\ \mu\text{m}$ by $3\ \text{mm}$. Note that the ultimate throughput limitation of SROFM is the speed of the CMOS image sensor. Even with our sensors (Aptina MT9T001), assuming the same fixed data transfer rate, with a more restricted FOV of $50\ \mu\text{m}$ by $100\ \mu\text{m}$ and maximum frame rate of $75000\ \text{fps}$, our current device could image a continuous stream of cells at a rate of $1300\ \text{HR images/sec}$ with each image possibly containing multiple cells; to further increase the throughput of our device, we could use a high speed global shutter CMOS image sensors.

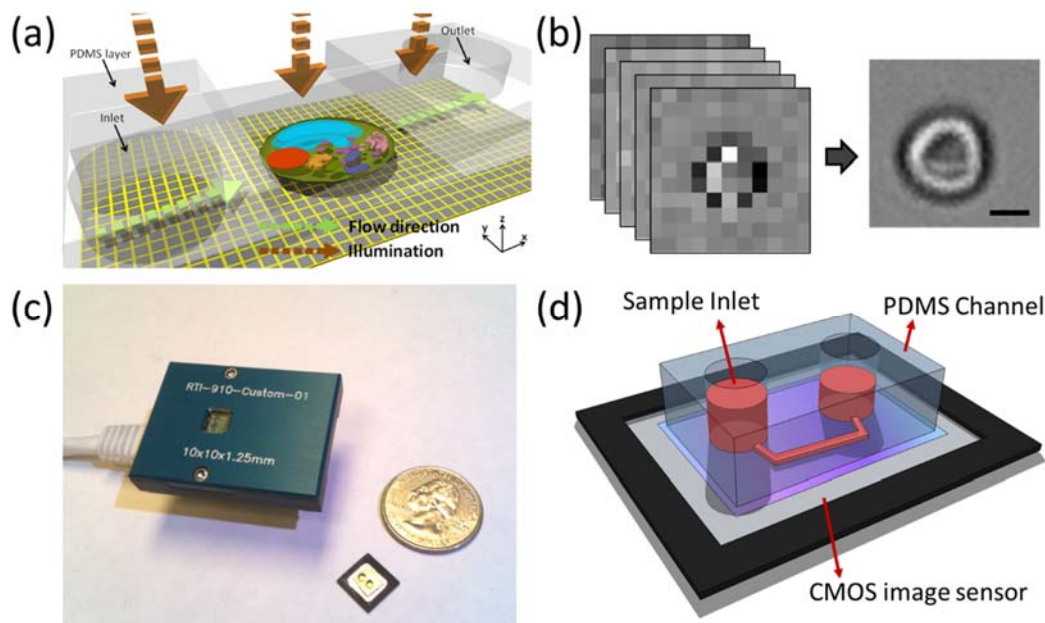


Figure 2 - 8. Schematics of the SROFM device. (a) A sample, depicted as a cell in the figure, is flown in a microfluidic channel on top of an image sensor and the LR projection images are recorded. (b) Image reconstruction from low resolution sequence to high resolution image. Scale bar indicates $5\ \mu\text{m}$. (c) Photograph of an actual sub-pixel resolving optofluidic microscope (SROFM) device and the image sensor. Current SROFM device composed of the CMOS sensor-based SROFM chip and camera head. The SROFM chip measures $1\ \text{cm} \times 1\ \text{cm}$ and the total device, $5\ \text{cm} \times 3\ \text{cm} \times 3\ \text{cm}$ in size. (d) Illustration of a SROFM sensor that has microfluidic channel mounted on top of a CMOS image sensor.

2.3 Monochromatic imaging

2.3.1 Motion vector estimation

In pixel super-resolution techniques, the quality of the reconstructed HR image depends largely on the knowledge of the precise sub-pixel shifts between subsequent images, collectively termed the motion vector of the LR image sequence. While the motion vector of a LR image sequence is in theory a known set of values in pixel super-resolution schemes involving precision scanning stages or actuators, implementation of a compact, microscanning system would not only be difficult and costly, but also prone to structural stability issues that could affect the accuracy of the motion vector.

In contrast, the motion vector in SROFM can be estimated, quite accurately, by analyzing the rough position of the sample across the LR image sequence since the flow of the sample is highly stable within the microfluidic channel (low Reynolds number). For the simplest assumption of a sample flowing at constant velocity, the motion vector can be calculated from the location of the sample in the first and the last frames. However, in many cases, the sample's motion is not strictly uniform or purely translational due to the geometry of the sample itself, defects in the microfluidic channel or changes in the flow rate. To compensate for this non-uniform motion, we developed several fast image processing techniques to estimate the motion vector from the LR sequence.

For highly scattering samples, we developed and used the following technique to generate a motion vector for a LR image sequence. First, the background of each LR image is subtracted and the contrast is enhanced. Highly absorbing objects in LR images appear darker than the background, thus we can use this information to determine the location of the sample within each LR frame. To do this, we binarize the image using a single threshold computed from the entropy of the image histogram. The geometric centroid of each of these binarized images from the LR image sequence is then computed and the entire array of centroids is low pass filtered to account for both the smooth flow pattern of the sample and the quantization error from binarizing and computing the centroid of each individual LR image.

For samples with lower contrast or bright spots, the motion vector is calculated in a similar manner, except the images are binarized with two thresholds. We calculate the background noise level and binarize the image by converting any pixel that is above or below the noise level to 0 while making the rest 1. Also, in order to avoid errors due to the geometry of the sample, we use the pixel coordinate of the bounding box of the object and low pass filter the data to obtain sub-pixel shift values.

For microspheres that are smaller than a pixel size, it is more difficult to distinguish a pixel response that results from the shadowing of the microsphere from the sensor's background noise. In this case, we obtain the motion vector by observing the blinking of the pixels on the expected pathway of microspheres (parallel to the channel wall). From the raw data, we can obtain the pixel coordinates where the microspheres are expected to flow through. This pathway can be any line of pixels within the channel that are parallel to the channel wall, since the microspheres follow the laminar flow of the solution. We then extract the time variation of the pixel response on the pathway, which shows

the blinking of the pixels as the microsphere moves across each pixel, and calculate the motion vector from the slope $(\Delta x/\Delta f, \Delta y/\Delta f)$.

These techniques that we developed for motion estimation, essential for reconstruction of a HR image, allow the motion of the sample to be estimated from only the LR image sequence. With this technique, the requirement for uniform and laminar flow or use of a precision scanning or stepping detector or light source is eliminated.

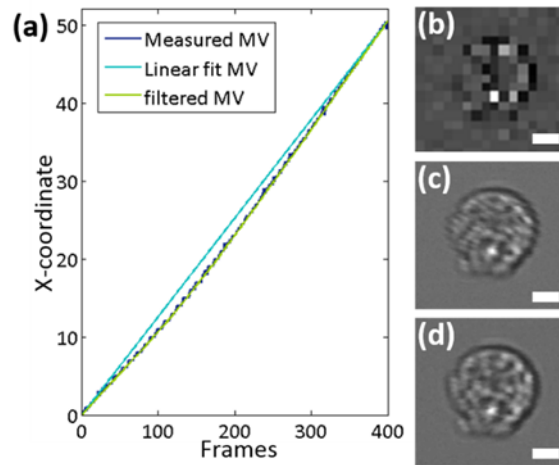


Figure 2 - 9. Improvement of the HR image with the non-linear motion vector estimation. (a) Measurement of motion vector from the raw sequence shows the error between the linearly estimated motion vector and the actual motion of the object. (b) The raw image of the sample. (c) HR image reconstructed with the linearly estimated motion vector. The streaks and jagged edges in the image result from the discrepancy between the motion vector used in reconstruction and the actual location of the object. (d) HR image reconstructed with the non-linear motion vector measured with the methods described above. All scale bars indicate $10\mu\text{m}$.

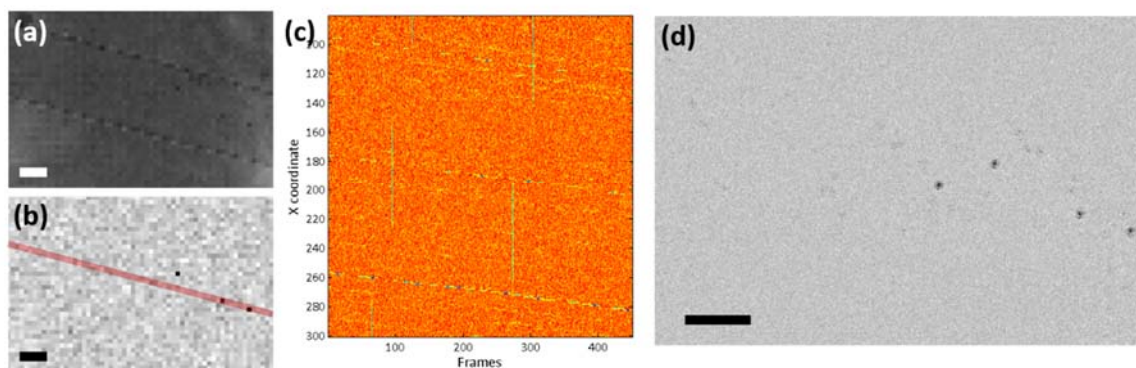


Figure 2 - 10. Motion estimation of microspheres smaller than the pixel size ($1\mu\text{m}$ microspheres). (a) Raw LR image showing the channel structure. (b) Normalized raw image with the contrast enhanced. The response of the pixels under the red line, which is parallel to the channel wall, is processed to obtain the motion vector. (c) Time resolved response of the line of pixels show the microspheres passing through each pixel. The slope of streaks ($\Delta x/\Delta f$) indicates the motion vector in x direction and $\Delta y/\Delta f$ can be calculated from the slope of the red line in (b). (d) HR image of the microspheres reconstructed with the motion vector obtained from (c). All scale bars indicate $20\mu\text{m}$.

2.3.2 SROFM imaging of biological samples

Once the motion vector of the LR image sequence is calculated, a shift-and-add pixel super-resolution algorithm can be applied to reconstruct a single HR image[21]. Such an algorithm consists of shifting each LR image by the relative sub-pixel shift given by the computed motion vector and adding them all together to fill a blank HR image grid of enhancement factor of n , where each n -by- n pixel area of the HR image grid corresponds to a single 1-by-1 pixel area of the LR image grid. The wiener deconvolution method is then used to remove pixel blurring in the final HR image. Figure 2 - 11 shows both LR and HR SROFM images of several biological samples: *Entamoeba invadens* cysts ($d\sim 25\mu\text{m}$, Figure 2 - 11a,b), *Trypanosoma cruzi* ($l\sim 15\text{-}30\mu\text{m}$, $w\sim 1\text{-}3\mu\text{m}$, Figure 2 - 11c), *Giardia lamblia* trophozoites ($l\sim 15\text{-}30\mu\text{m}$, Figure 2 - 11d,f) and human red blood cells ($d\sim 8\mu\text{m}$, Figure 2 - 11f). Taking into account the Nyquist sampling criteria, the resolution limit of each LR image should be $6.4\mu\text{m}$ for $3.2\mu\text{m}$ -pixel sensors (Figure 2 - 11a-c) and $4.4\mu\text{m}$ for $2.2\mu\text{m}$ -pixel sensors (Figure 2 - 11d-f). Note that each individual LR image contains very little spatial information about the sample other than its rough location and size, but each HR image is clearly improved in resolution. Conventional microscope images taken with a $20\times$ objective (Figure 2 - 11a-e) and $40\times$ objective (Figure 2 - 11f) are also shown for comparison.

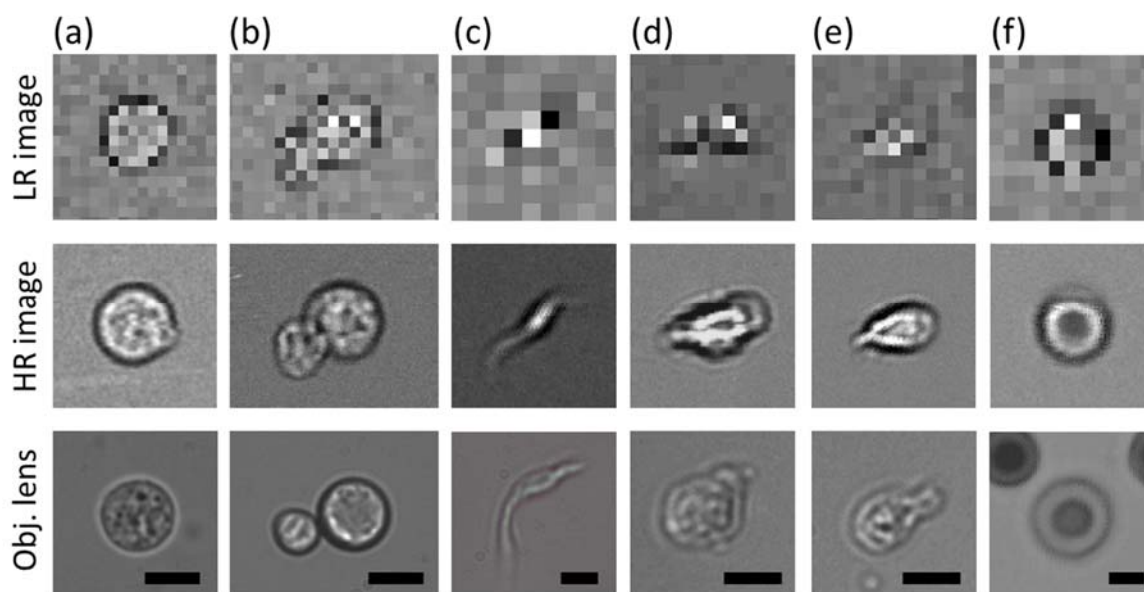


Figure 2 - 11 . Images obtained from the SROFM device. *Entamoeba invadens* cysts (a-b). Raw low resolution (LR) images from the sensor (Top row), High resolution (HR) images reconstructed from the sequence of LR images (Middle row) and conventional bright field microscope images taken with 20 \times objective lens (Bottom row). 40 to 50 LR frames were used to reconstruct each HR image.

2.3.3 Imaging rotating samples

SROFM is not only simpler than the previous aperture-based OFM, but also more robust and able to image samples flowing with non-uniform translational motion and even rotation. Since the motion vector of a LR image sequence with SROFM is estimated from the image sequence itself, precise flow control is no longer required. Hence, whereas aperture-based OFM would utilize an additional electrokinetic driving scheme to ensure uniform flow, SROFM devices can be used with a drop-and-flow scheme, where a small volume of liquid sample is injected from the inlet and drawn into the channel by capillary action and the pressure difference between inlet and outlet. Even though the flow rate will gradually decrease as pressure between the inlet and the outlet equalizes, a non-uniform motion vector can be estimated and used to reconstruct a high quality HR image. Furthermore, SROFM can image samples flowing with rotational movement, as long as the rate of rotation is slow relative to the image capture frame rate. Figure 2 - 12b shows the sequence of HR images of a cell near the channel side wall, flowing with both in-plane and out-of-plane rotation.

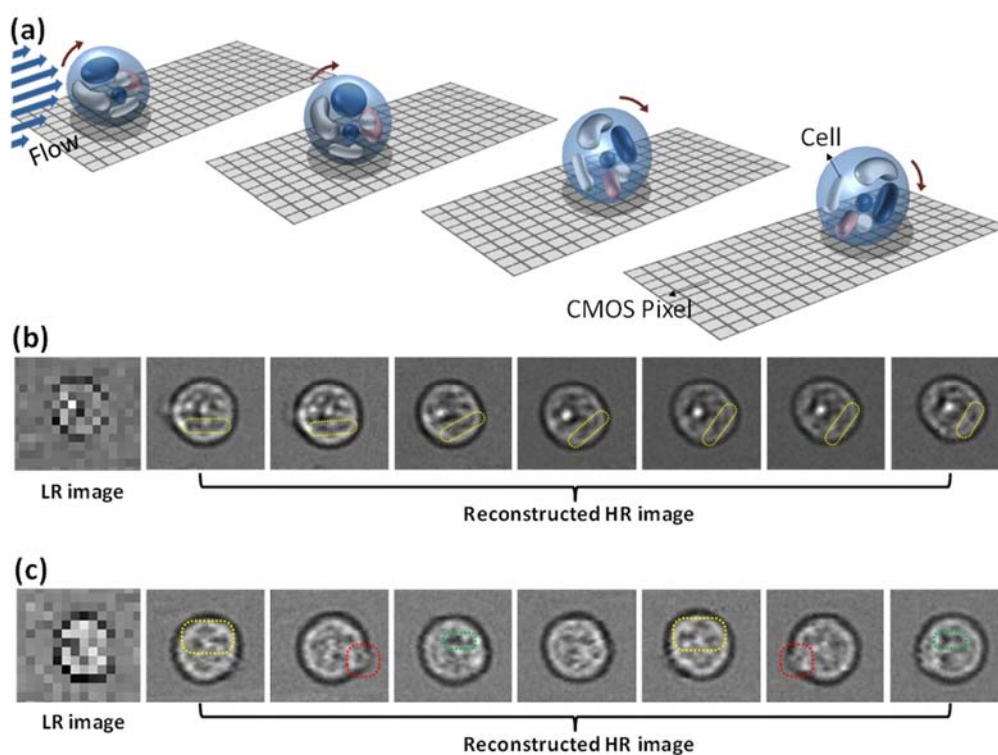


Figure 2 - 12. Sequential HR images of rotating cells (scale bar 10 μm). (a) Cells flowing with rotational movement allow the SROFM to capture images of different projections, revealing the three-dimensional inner cellular structures. (b) HR sequence of an *Entamoeba invadens* cyst traveling with in-plane rotation. Note that the highlighted part of the sample is rotating in the sequence. The length of the dark spot in the highlighted region is also decreasing in the time lapse, indicating that the sample has out-of-plane rotation as well. (c) Sample translating with out-of-plane rotation. The highlighted regions with the same color reveal that the pairs of images are rotated 180 degrees out-of-plane of each other. Each pair of images is distinct from the others, showing the complex inner structure of the cell from a different projection plane.

SROFM's ability to image samples with rotational movement provides us with the unique opportunity to image samples from different perspectives. When cells rotate out-of-plane while flowing through the channel, we can observe the cells from different projections, and hence better resolve their three-dimensional inner structures. The requisite rotational motion for such imaging is naturally provided by the interaction of the cell with the non-uniform flow velocity profile of pressure-driven laminar fluid flow in the microfluidic channel. Figure 2 - 12 shows sequential HR images of an *Entamoeba invadens* cyst rolling in the channel. Note that pairs of images highlighted with the same color are mirror images of each other, indicating that the cell has rotated 180 degrees along the direction of flow. These images reveal the three-dimensional location of each of the dark and bright spots in the cyst, as well as its external morphology. 350 frames of the LR image sequence were used to reconstruct the HR images, with 50 LR frames used for each HR frame. The motion blur due to

the rotation within each 50 frames is not itself significant in the HR images, but if the rate of rotation of the sample is too fast relative to the translational movement, then the rotation blur would degrade the image quality. Additional modification in the design of the microfluidic channel could help control the rotation of the sample to achieve consistent rotational imaging without significant motion-blur. As such, we can perform rotational imaging with SROFM without any additional scanning stages or multiple light sources. The flexible ability of SROFM in imaging samples that are rotating or flowing with non-uniform velocities is a significant advantage over other designs.

2.3.4 Resolution of SROFM

The optical resolution of the device was experimentally investigated by imaging 500 nm microspheres with our SROFM device. We used 500 nm blue-dyed microspheres (Polysciences) to enhance the contrast of the microspheres images. The microspheres were flown through a 1.5 μm -thick PDMS channel. We used two image sensors with pixel size of 3.2 μm and 2.2 μm . The full-width half maximum (FWHM) of 0.80 μm was obtained with EF of 10 for 3.2- μm sensor and 590 nm under EF of 10 at 2.2- μm sensor (Figure 2 - 13). This suggests that the optical resolution of the device was $\sim 0.8 \mu\text{m}$ and 0.66 μm for SROFM systems with 3.2- μm and 2.2- μm sensors, respectively. This limit was obtained by the fact that two spots would need to be at least 3 high resolution pixels apart to be distinguished. As a reference, resolution of a conventional microscope resolution with 0.4NA 20 \times objective lens is 0.84 μm . The experimental resolution agrees with the predicted values in 2.1.3. However, the bright centers of the microspheres were clearly resolved in the 2.2- μm sensor and not in the 3.2- μm sensor. It is due to the relative size ratio between the object and the sensor. 500-nm microspheres are too small compared to the photodiode size of 3.2- μm sensor, hence the bright center and the dark rim are averaged out and the microsphere acts as an absorbing object which blocks the illumination light. In 2.2- μm sensor, the photodiode size is small enough to resolve the lensing effect caused by the microsphere. We can observe the blinking of the pixels in the LR sequence as the microsphere passes through.

We further note that resolution deteriorates as the distance between the sample and sensor surface increases. Verification of this relationship has been examined in Ref. [19]. By numerical analysis, we expect the point spread function with 500 nm microsphere will spread out to FWHM of 1.8 μm at the center of 5.5 μm channels. The resolution can be improved by using higher EF, which requires more precise control of sample movement over a longer scanning length. The reduction of sensor pixel size can also improve image resolution further. However, this improvement approach is

expected to yield diminishing returns for pixel sizes beyond our current sensor pixel size, without a tandem effort to push the blood cells closer to the channel floor to mitigate the resolution deterioration associated with the sample-to-sensor-surface distance.

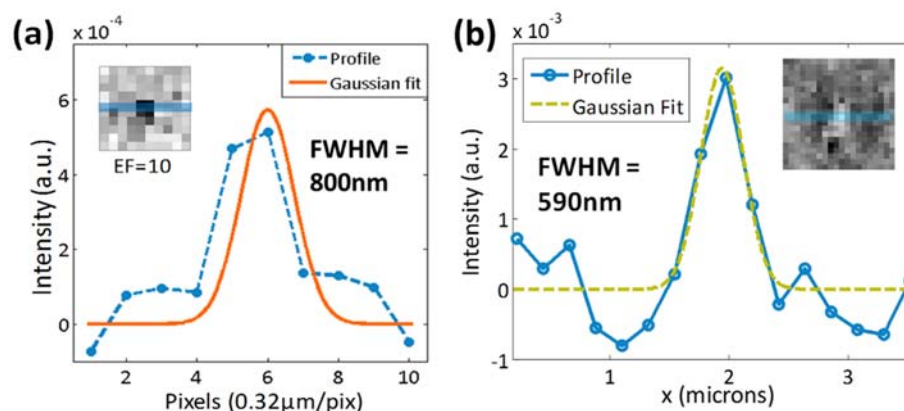


Figure 2 - 13. Resolution of the SROFM prototype obtained with $0.5\mu\text{m}$ microspheres. (a) Intensity profile of the $0.5\mu\text{m}$ microsphere from image reconstructed with an enhancement factor of 10 and pixel size of $3.2\mu\text{m}$ (inset). (b) Intensity profile of the same sphere reconstructed with an enhancement factor of 13 (inset). (c) Intensity profile of the $0.5\mu\text{m}$ microsphere imaged with enhancement factor of 10 and pixel size of $2.2\mu\text{m}$ (inset). FWHMs of the profiles in (a) and (b) are $0.8\mu\text{m}$, $0.66\mu\text{m}$ and $0.59\mu\text{m}$ respectively.

2.4 Color SROFM based on RGB illumination

In on-chip microscopy, color imaging can be a crucial component in order to detect and identify different functional structures within biological specimens with staining. Typically, color imaging can be done with the use of filters, by putting an array of RGB filters on the pixel grid of image sensors. However, since SROFM achieves highest resolution with samples flown near the sensor's surface, we removed the additional filter layer between the sample and the sensor for the sake of the imaging resolution. Instead, we accomplished color imaging by using three-color sequential illumination. In our color SROFM scheme, RGB LEDs were used with sequential switching to generate 3 separate color image sequences, which were later combined into a single full-color high resolution image.

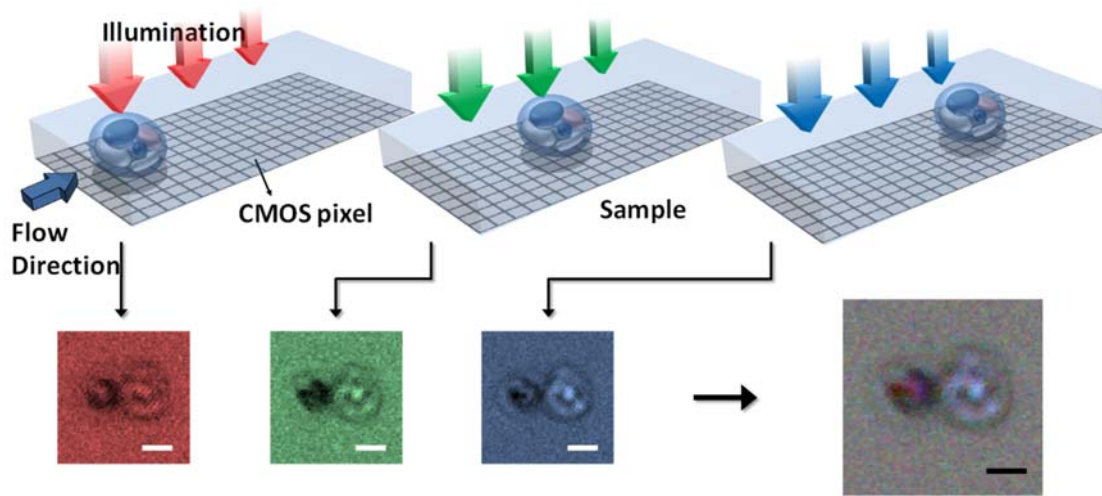


Figure 2 - 14. Color SROFM using sequential RGB LED illumination.

To verify the color capability of the RGB illumination method with SROFM, we measured the light transmission through the microfluidic channel with different concentrations of Trypan blue dye. By the Beer-Lambert law, light transmission through an absorbing dye can be expressed as:

$$T = T_0 e^{-n\sigma l} \quad (2,12)$$

where T_0 is the light transmission in the absence of a sample, n is the concentration of the dye, σ is the absorption cross-section of the dye and l is the optical path length through the sample. Signal through the $27 \mu\text{m}$ -channel filled with the Trypan blue dye with concentration varying from 0 to 0.4% was measured for all three illumination wavelengths of 625 nm, 525 nm and 475 nm. With increasing concentration of dye, we expect the absorption to increase linearly too, with the slope corresponding to the absorption cross-section σ for each illumination wavelength. Figure 2 - 15 confirms that the logarithm of signal transmission through Trypan blue dye is proportional to the concentration of the dye and that the relative values of σ for the three wavelengths agree with the known absorption spectrum of Trypan blue dye.

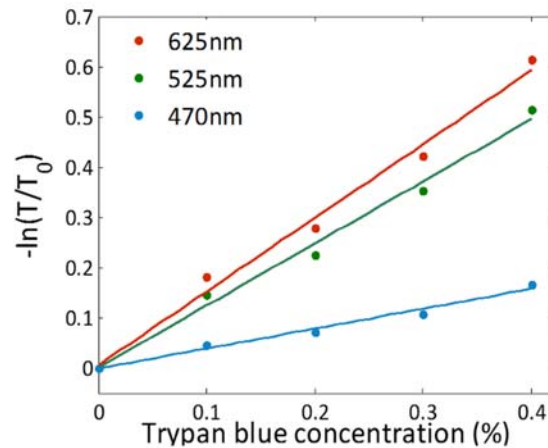


Figure 2 - 15. Color response of our SROFM device. Light transmission through a 27 μm channel containing different concentrations of Trypan blue dye. This figure demonstrates agreement with the Beer-Lambert law of light absorption, validating SROFM's color imaging capabilities.

2.5 Malaria screening with SROFM

The combination of high resolution imaging and flow-cytometry scheme implies that the OFM system may be suitable for diagnostic imaging of blood samples. For many diseases involving blood-borne parasites and blood cell deformations, the gold standard of diagnosis is with optical microscopy, where a large number of blood cells needs to be imaged with high optical resolution [22]. However, in rural and developing areas, microscopy-based diagnosis suffers from its bulkiness and the cost, which hinder the effort to eradicate for poverty-related diseases like malaria [23]. For such challenging environments, portable "dipstick" devices based on immunochromatographic methods have been developed[24] with inherent limitations in the detection sensitivity and diagnosis accuracy[22]. SROFM combines the high sensitivity of microscopic diagnosis and the accessibility and low-cost of a portable device, offering a good potential alternative for the field diagnosis of malaria. Also, flow cytometry-like screening of blood sample can potentially provide a quantitative analysis of infection and classification of parasites. In Section 2.3, we have demonstrated monochromatic imaging of various biological samples using SROFM devices with a sub-micron resolution at its plane of highest acuity. In order to utilize the SROFM device in malaria diagnosis, color imaging with higher resolution would need to be achieved for detection and identification of the stained parasites within the RBCs.

To demonstrate the potential application of our color SROFM device for malaria field diagnostics, we imaged red blood cells (RBCs) infected with *P. falciparum*. Imaging-based diagnosis

of Giemsa-stained blood is the most widely used diagnosis method for malaria in the field. However, to avoid additional processing steps in sample preparation, we searched for a dye that, unlike Giemsa, does not require previous fixation of cells. In order for SROFM to be utilized for the diagnosis of malaria in the field, the ability to detect the color-stained parasites in high resolution is necessary since identification of plasmodium species by appearance is an essential part of the diagnosis for the treatment and the control of the disease.

2.5.1 Device optimization for blood cell imaging

Our prototype color SROFM system for blood cell imaging is depicted in Figure 2 - 16. The illumination, image acquisition and image processing were controlled by a laptop computer. Three light emitting diodes (LED) with wavelengths of 625 nm, 525 nm and 475 nm were used for illumination with a switching rate of 8Hz. LEDs and the diffuser plate were placed about 5 cm above from the sensor in order to provide enough room for the pipetting the samples into the system. The illumination intensity of 0.3, 0.18 and 0.28 W/m² was used for red, green, and blue, respectively. Fig 1B shows the circuit board for the sensor (EPIX inc.) and a SROFM chip, which consisted of a CMOS image sensor and a poly-dimethylsiloxane (PDMS) microfluidic channel mounted on top (Fig 1C), with a total size of approximately 1 cm by 1 cm. In all blood-cell imaging experiments, we used Aptina MT9P031 5 megapixel image sensors with the pixel size of 2.2 μm . The chip is mounted on a commercial camera (EPIX inc) with cat-5 Ethernet cable connection to a commercial PCI board (EPIX inc). For data acquisition, we used a commercial software (EPIX XCAP LTD) with 3GB frame buffer and the processing was performed with a custom software written in Matlab.

The pre-treated whole blood sample was injected into the inlet of the device and flowed through the channel. As the blood cells flowed across the channel, low resolution images were obtained from the image sensor with a region of interest (ROI) of 300 by 80 pixels. The CMOS image sensor used in the experiment provided a maximum frame rate of 838 fps with this ROI size. We typically used 800fps with an exposure of 0.1ms to ensure that the motion-blur from the movement of the blood cells within a single frame was less than 100 nm. We alternated the RGB light sources at a switching rate of 8Hz. This allowed us to acquire 100 low-resolution frames between each color switch for pixel super-resolution reconstruction with an enhancement factor of 10. With our device design and pre-treatment conditions, a drop-and-flow scheme allowed for a flow rate of 500-1000 $\mu\text{m}/\text{s}$, with an average of approximately 50 cells within the imaging ROI at any time. (Figure 2 - 16c). With the current values of sample flow rate and low resolution imaging frame rate, the system can scan

approximately 400 cells/sec for monochromatic imaging and 100 cells/sec for color imaging. This scan rate can be increased by further optimizing channel dimensions and sample concentrations.

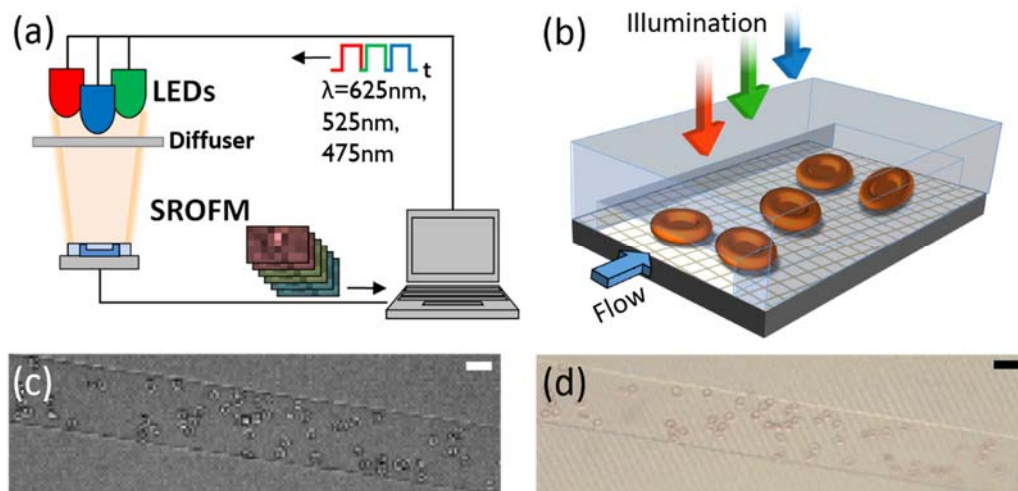


Figure 2 - 16. Schematics and prototypes of our color SROFM device. (a) Schematics of color SROFM system showing sequential RGB LED illumination and SROFM device controlled by a computer. (b) Detailed view of color imaging area where the sample, blood cells, is flowing in the channel on top of the sensor's pixel grid while the illumination is varied in color. (c) Low resolution image of blood cells in a SROFM device directly taken from the CMOS image sensor. (d) Conventional bright field microscope image of the same field of view, taken with a 10x objective lens. Scale bars indicate 20 μm .

For reconstruction of high resolution images, the center-of-mass of each cell was tracked by motion vector calculation as described in Section 2.3.1. We used the obtained motion vector as a reference point for image registration. To constitute a color image, we simply superposed the R, G, and B images by overlapping their center-of-mass. To check for misregistration of RGB images, we also superposed 2 sequential R images by the same approach and check for image shift/distortion.

In order to reduce in-plane rotation of the cells, inertial focusing of the blood cells was introduced by putting obstacles along the walls in the beginning part of the channel[20]. This reduced the number of cells near the channel walls which were more likely to rotate due to the asymmetric flow differentials near the channel walls. The surfaces were heparinized by flushing the channel with 100 units of heparin in PBS. This treatment facilitated the flow by enhancing the wettability and prevented cells from attaching to the surface, which can cause blockage of the channel and/or disturbance in the flow. In addition, an array of micropillars with diameter and spacing of 15 μm were placed near the inlet to block any clumped cells from entering the channel.

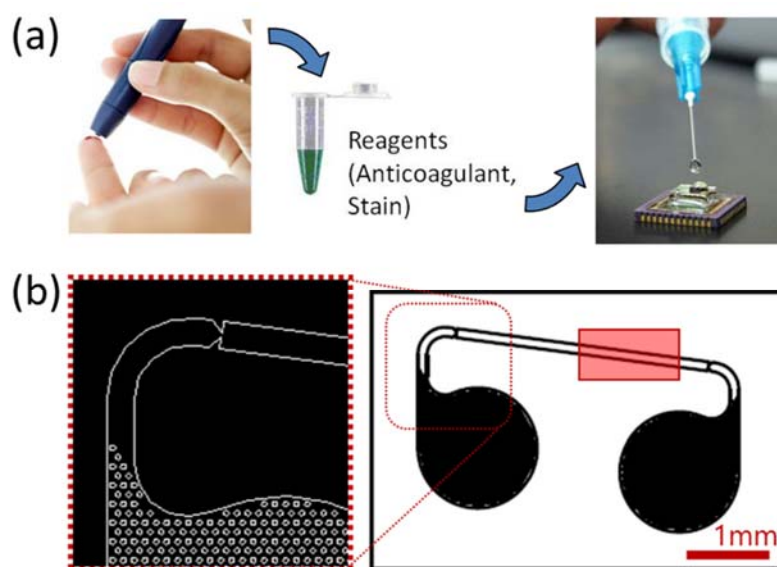


Figure 2 - 17. (a) Drop-and-flow scheme for high-throughput imaging of blood cells. (b) Channel design for blood cell imaging

2.5.2 Sample preparation

For malaria infected blood cells, we purified cultures of *P. falciparum* to obtain infected RBCs (iRBCs) in the schizont or late trophozoite stage at a concentration >98%. Samples were treated with 2% Toluidine blue, to stain the *P. falciparum* parasites within. The samples were live-stained in solution, as opposed to using blood smears. Cells were imaged without washing of the dye, since the background color contribution from the staining solution is negligible due to the small thickness of the channel. *P. falciparum* 3D7 strain was cultured in vitro following standard procedures. Mature *P. falciparum*-infected erythrocytes, including schizonts and late trophozoites, were isolated from the interphase of a 90%/40% Percoll gradient. As control, uninfected erythrocytes were prepared in parallel. After isolation, cells were diluted to ~ 50000 cells/ml in PBS with 100 units of heparin. This dilution prevents overlapping of the cells in the channel. Then the sample was incubated with 2% Toluidine blue for 10 min before imaging.

For direct imaging of human whole blood sample, a peripheral blood sample was diluted to 1:50 with Phosphate buffered saline (PBS), in order to prevent overlapping of the cells in the channel and heparin was added to a final concentration of 100 U/ml to prevent clogging. Human whole blood sample used in all experiments were obtained from New York Blood Center.

2.5.3 SROFM imaging of malaria infected red blood cells

Figure 2 - 18 shows color images of *P. falciparum* iRBCs at the schizont-stage and naïve RBCs taken with the SROFM device. The images show clear differences between the schizont-stage and naïve RBCs, with the bright purple spots in the iRBCs indicating the presence of parasites. Additionally, we conducted the same experiment with *P. falciparum* ring-stage iRBCs, but we were not able to achieve a clear differentiation in that experiment. We believe that the unsuccessful identification of *P. falciparum* ring-stage iRBCs possibly resulted from the weak color contrast from the live-stained blood samples.

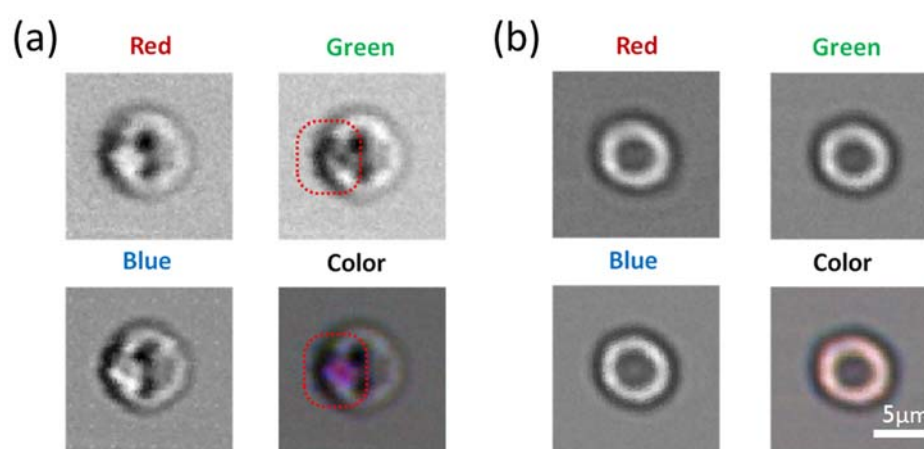


Figure 2 - 18. SROFM images of *P. falciparum*-infected and naïve RBC. (a) Red, green, blue and combined color images of *P. falciparum* schizont-stage RBCs stained with Toluidine blue, showing a distinct purple spot within each RBC, which appears as dark spots in the green channel. (b) Images of naïve RBCs show clear differences with the infected RBCs. Naïve RBCs were also stained with Toluidine blue as a control.

As an initial study for the diagnostic potential of this technology, we performed a blind experiment with SROFM images of naïve and schizont-stage RBCs. In the experiment, we asked 4 experienced malaria researchers to identify the cell type for 30 randomized images of naïve and schizont stage erythrocytes (13 and 17 images). The researchers were able to make the right identification in 88% of the cases. The current result of successfully detecting schizont-stage iRBCs is not yet sufficient for diagnosing *P. falciparum* infections, which require detecting the earlier ring-stage iRBCs. However, the results suggest that the SROFM may be able to identify other types of plasmodium parasites that exist in the schizont-stage in peripheral blood of patients. *P. vivax* is an excellent example as this variety can be diagnosed from schizont-stage iRBCs.

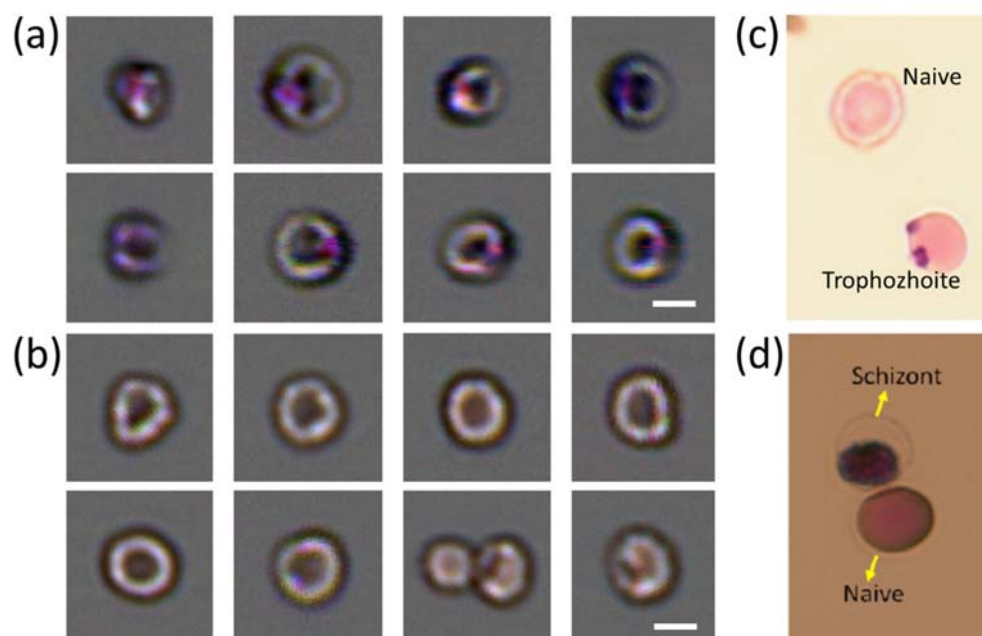


Figure 2 - 19. Color SROFM and conventional microscope images of *P. falciparum*-infected and naïve RBC. (a) *P. falciparum* schizont stage RBC images taken with color SROFM system. (b) naïve RBC images taken with color SROFM. (c-d) Bright field microscope images of *P. falciparum*, trophozoite-stage, schizont-stage and Naïve RBCs stained with Toluidine blue. Images are taken with (c) 40 \times and (d) 100 \times objective lens. Scale bars indicate 5 μ m.

2.6 Discussion

We have developed a compact high-resolution color imaging microscopy device based on SROFM and color illumination. Our device achieved an optical resolution of 660 nm. Our preliminary experiment indicates that color SROFM can potentially be a useful diagnostic tool for identifying malaria infected cells.

SROFM's simplicity, compactness, and cost-effectiveness make it well-suited for drop-and-flow screening of fluidic samples such as blood, urine or water. We believe that the SROFM technique can potentially play a significant role in the eventual development and commercialization of a mass-distributed, portable microscope for point-of-care analysis and third-world diagnostics, for the detection of water-borne parasites, blood-borne parasites and diseases involving blood cell deformations. We have demonstrated high-throughput imaging of preliminary experiment indicates that color SROFM can potentially be a useful diagnostic tool for identifying malaria infected cells.

One advantage of the SROFM technique for malaria diagnosis is that it can operate with a simpler preparation protocol than standard microscopy based on blood smears. A typical blood smear

test requires several steps in film preparation, fixation, staining and washing. In contrast, the SROFM technique employs solution-based preparation protocol where the imaging is directly performed on the samples without requiring slide preparation. The sample preparation protocol for SROFM imaging comprises of a single step of mixing a blood sample with a solution containing buffer, anticoagulants and stain. While a typical blood smear requires a washing step to remove excess dye that was not uptaken by the sample, we found that such a step is not required in our imaging process with the SROFM. This is because the overall height of the microfluidic channel was sufficiently low that the residual dye in the fluid medium did not significantly attenuate light transmission when compared to the light attenuation from the dye within the cells.

We believe that SROFM technique can be a good fit with the technological needs of global healthcare. Portable imaging/diagnostic devices can benefit for healthcare in rural regions where conventional clinical devices are too bulky to transport well or too expensive to employ widely. In addition, electronic devices that can be integrated with telemedicine network can support efficient utilization of scarce medical expertise. For this matter, we believe that the SROFM technique possesses a few key potential advantages in global health applications; (1) Compact size of the SROFM technology allows for the implementation of light-weight and cheap hand-held systems. (2) The technique requires minimal training for operation and the collected raw data can be processed into useful microscopy images with none or very few manual inputs. (3) The principle of operation is inherently simple and robust and thus has a relatively low demand on the computational power it requires for image processing. Although the data acquisition of current SROFM system relies on an Ethernet cable connection and a frame buffer memory in the processor, a new camera system with an on-board memory and a universal serial bus interface can support stable acquisition and transfer of data with low-power portable systems. (4) The final image data is obtained for each individual cells with consistent image parameters, a convenient format for quantitative analysis and application in computer aided diagnosis based on pattern recognition. As such, this technology is potentially an attractive candidate for telemedicine systems in the developing world.

However, further improvement of the technology would need to occur for the method to be truly applicable to malaria diagnostics. For example, SROFM would need to improve in its sensitivity to the point where *P. falciparum* ring-stage iRBCs can be observed. Smaller pixel size may increase the imaging performance of SROFM device. Alternately, a better dye protocol by which stronger staining of iRBCs would need to be developed. In addition to improving its performance, thorough assessment

is needed to determine whether conventional criteria for malaria diagnosis applies for SROFM images, since they may differ from those obtained with conventional light microscopy. Total cost per diagnosis need to be considered in order to compete with current techniques; there is room for cost reduction with the lowering price of CMOS sensors, integration of multiple tests on a single chip and foundry-based mass-production of fluidic channels. However, other practical issues such as reagent shelf-life and the sensor's durability in extreme environments also need to be thoroughly assessed. Along with the technological improvements discussed above, a field-testing of the system will provide better perspective on the aptitude of the technique in the global malaria diagnostics market.

BIBLIOGRAPHY

1. Tsai, R. and T.S. Huang, *Multiframe image restoration and registration*. Advances in computer vision and Image Processing, 1984. **1**(2): p. 317-339.
2. Sung Cheol, P., P. Min Kyu, and K. Moon Gi, *Super-resolution image reconstruction: a technical overview*. Signal Processing Magazine, IEEE, 2003. **20**(3): p. 21-36.
3. Farsiu, S., M. Robinson, M. Elad, and P. Milanfar, *Fast and robust multiframe super resolution*. IEEE Transactions on Image Processing, 2004. **13**(10): p. 1327-1344.
4. Irani, M. and S. Peleg, *Improving resolution by image registration*. CVGIP: Graphical Models and Image Processing, 1991. **53**(3): p. 231-239.
5. Bishara, W., T. Su, A. Coskun, and A. Ozcan, *Lensfree on-chip microscopy over a wide field-of-view using pixel super-resolution*. Optics Express, 2010. **18**(11): p. 11181-11191.
6. Baker, S. and T. Kanade, *Limits on super-resolution and how to break them*. Pattern Analysis and Machine Intelligence, IEEE Transactions on, 2002. **24**(9): p. 1167-1183.
7. Lin, Z. and H.-Y. Shum, *Fundamental limits of reconstruction-based superresolution algorithms under local translation*. Pattern Analysis and Machine Intelligence, IEEE Transactions on, 2004. **26**(1): p. 83-97.
8. Robinson, D. and P. Milanfar, *Statistical performance analysis of super-resolution*. Image Processing, IEEE Transactions on, 2006. **15**(6): p. 1413-1428.
9. Chen, T., P.B. Catrysse, A. El Gamal, and B.A. Wandell. *How small should pixel size be?* in *Electronic Imaging*. 2000. International Society for Optics and Photonics.
10. Cui, X., L.M. Lee, X. Heng, W. Zhong, P.W. Sternberg, D. Psaltis, and C. Yang, *Lensless high-resolution on-chip optofluidic microscopes for Caenorhabditis elegans and cell imaging*. Proceedings of the National Academy of Sciences, 2008. **105**(31): p. 10670-10675.
11. Honghao, J., D. Sander, A. Haas, and P.A. Abshire, *Contact Imaging: Simulation and Experiment*. Circuits and Systems I: Regular Papers, IEEE Transactions on, 2007. **54**(8): p. 1698-1710.
12. Greenbaum, A., W. Luo, B. Khademhosseini, T.-W. Su, A.F. Coskun, and A. Ozcan, *Increased space-bandwidth product in pixel super-resolved lensfree on-chip microscopy*. Sci. Rep., 2013. **3**.
13. Courjon, D., J.-M. Vigoureux, M. Spajer, K. Sarayeddine, and S. Leblanc, *External and internal reflection near field microscopy: experiments and results*. Appl. Opt, 1990. **29**(26): p. 3734-3740.
14. Li, J., Z. Peng, and Y. Fu, *Diffraction transfer function and its calculation of classic diffraction formula*. Optics Communications, 2007. **280**(2): p. 243-248.
15. Fontaine, R., *The Evolution of Pixel Structures for Consumer-Grade Image Sensors*. Semiconductor Manufacturing, IEEE Transactions on, 2013. **26**(1): p. 11-16.
16. Fossum, E.R., *CMOS image sensors: electronic camera-on-a-chip*. Electron Devices, IEEE Transactions on, 1997. **44**(10): p. 1689-1698.
17. Shan, Q., J. Jia, and A. Agarwala. *High-quality motion deblurring from a single image*. in *ACM Transactions on Graphics (TOG)*. 2008. ACM.
18. Agranov, G., R. Murrison, J. Ladd, A. Dokoutchaev, X. Fan, X. Li, Z. Yin, R. Johnson, V. Lenchenkov, and S. Nagaraja. *Pixel continues to shrink, pixel development for novel CMOS image sensors*. in *Proceedings of the 2009 International Image Sensor Workshop*. 2009.
19. Cui, X., L. Lee, X. Heng, W. Zhong, P. Sternberg, D. Psaltis, and C. Yang, *Lensless high-resolution on-chip optofluidic microscopes for Caenorhabditis elegans and cell imaging*. Proceedings of the National Academy of Sciences, 2008. **105**(31): p. 10670.

20. Xuan, X., J. Zhu, and C. Church, *Particle focusing in microfluidic devices*. *Microfluidics and Nanofluidics*, 2010. **9**(1): p. 1-16.
21. Elad, M. and Y. Hel-Or, *A fast super-resolution reconstruction algorithm for puretranslational motion and common space-invariant blur*. *IEEE Transactions on Image Processing*, 2001. **10**(8): p. 1187-1193.
22. Wongsrichanalai, C., M.J. Barcus, S. Muth, A. Sutamihardja, and W.H. Wernsdorfer, *A review of malaria diagnostic tools: microscopy and rapid diagnostic test (RDT)*. *The American journal of tropical medicine and hygiene*, 2007. **77**(6 Suppl): p. 119.
23. Gascoyne, P., J. Satayavivad, and M. Ruchirawat, *Microfluidic approaches to malaria detection*. *Acta Tropica*, 2004. **89**(3): p. 357-369.
24. Moody, A., *Rapid Diagnostic Tests for Malaria Parasites*. *Clin. Microbiol. Rev.*, 2002. **15**(1): p. 66-78.

SUB-PIXEL RESOLVING MOTION MICROSCOPY (SPMM)

Microscopy-based monitoring is a key tool in interrogating the growth and behavior mechanism of living cells or microorganisms. In this chapter, we present a chip-scale microscope specialized for long-term imaging of motile micro-organisms, with the sub-pixel resolution achieved by taking advantage of the inherent motion of the organisms. By applying the pixel super-resolution algorithm to a set of low-resolution images of the microorganisms as they freely move across the sensing area of a CMOS image sensor chip, we can render an improved resolution image of the microorganisms. This self-imaging Petri dish platforms with microscopy resolution, which we term as ePetri[1, 2], can significantly streamline cell cultures and/or other longitudinal biological studies. We perform longitudinal study of *Euglena gracilis* cultured in an ePetri platform and image based analysis on the motion and morphology of the cells. As a miniaturized and automated culture monitoring platform, this ePetri technology can greatly improve studies and experiments with motile microorganisms.

3.1 ePetri : self-imaging culture dish

Imaging provides direct and detailed information about the culture by visualizing the morphological and behavioral changes of each individual cell. In addition, current computational capabilities allows for automated longitudinal imaging and analysis, with low cost, reduced labor and better temporal resolution[3-6]. A standard microscope has long been a standard equipment in conducting imaging-based studies. However, time-resolved imaging using an expensive microscope increases the cost of these experiments. In addition, numerical aperture limitation of the objective lens in a microscope prohibits high-resolution imaging over a large area without the use of additional actuation systems.

Miniaturization of imaging tools for long-term imaging can benefit many scientific researches, such as study on the swimming behavior of flagellated protozoa[7, 8] and behavioral studies using *Caenorhabditis elegans* models[9]. In addition, it can lower the cost of many clinical applications such as sperm counting[10], toxin screening assay using fresh water microorganisms[11], and blood/water-born parasite diagnostics[12]. In these cases, the labor-intensive nature of these experiments and the challenge of efficiently imaging large assays have typically plagued this type of experiment format. A compact low-cost imaging format which automatically image growing cell

cultures can significantly improve Petri dish-based cell culture experiments. We believe that such a self-imaging Petri dish can significantly affect cell culture-based procedures in both medicine and science.

Chip-scale microscopy technology can appropriately address this particular imaging needs by reducing the cost and complexity of a conventional microscopy. However, OFM method relies on translational delivery of the target object by electro-kinetic or laminar flow inside a microfluidic channel, which makes it tough to continuously monitor the same living specimen repeatedly over a long period of time. Fortunately, we believe that the inherent motion of the microorganisms can be used a means to obtain sub-pixel shifts that are required for pixel super-resolution image reconstruction. In this chapter, we will discuss on a strategy that combines key ideas of SROFM and ePetri to appropriately perform microscopy imaging of motile microorganisms. We name this imaging technique sub-pixel motion microscopy (SPMM). Using SPMM, we first demonstrate high resolution imaging by taking advantage of the swimming behavior of motile protozoa *Euglena gracilis*, which is a well-known model organism for cellular tracking studies and many biological assays. Then, we conduct longitudinal study of *Euglena gracilis*, demonstrating microorganism counting, tracking and statistical analysis capabilities using the described ePetri system. Through the proof-of-concept experiments, we show that the ePetri platform using SPMM method allows for inexpensive, miniaturized and minimum-labor culture monitors that can benefit clinical and scientific researches.

3.2 SPMM Working principle and Device design

The SPMM ePetri dish platform takes a very simple geometry; a bare CMOS image sensor and a PDMS well mounted on top. As the microorganisms are cultured in the ePetri dish, the shadow images of the cells are continuously captured through the sensor. The resolution of the raw images is fundamentally limited to be equal to twice the pixel size of the image sensor by the Nyquist criterion (the pixel size is 2.2 μm in our experiment.). The use of SPMM method improves the optical resolution of the final images beyond this limit. SPMM is based on the pixel super-resolution algorithm[13, 14], where low resolution images of the same object with sub-pixel shifts are combined to a higher resolution image. For motile microorganisms, their inherent motion allows themselves to be scanned on the sensor's pixel grid, providing the sub-pixel shifts between each low resolution frame that are essential for the image reconstruction. Collected low resolution images are redistributed into a denser grid of a single high resolution image, with the redistribution vector determined by the

sub-pixel displacement of the cell at each frame with respect to the first frame. We use minimum of m^2 low resolution frames for a single high resolution image reconstruction, where m is the enhancement factor, defined as the size ratio between the original low resolution pixel and the virtual high resolution pixel.

The ePetri system is shown in Figure 3 - 1. Each ePetri chip containing the sample is loaded into a camera board. A customized software controls the camera through a frame grabber and performs subsequent image processing for pixel super-resolution reconstruction. We used Aptina MT9P031 5 megapixel image sensors with the pixel size of $2.2 \mu\text{m}$, which has the total imaging area of $5.7 \text{ mm} \times 4.4 \text{ mm}$. As in OFM systems, the optical resolution of the ePetri is the highest at the floor of the image sensor. In order to keep the microorganisms as close to the sensor surface as possible, we dispensed as little amount of culture medium containing the specimen into an ePetri chip as possible ($< 5 \mu\text{L}$), and confined the vertical location of the microorganisms to less than $100 \mu\text{m}$ from the sensor's surface. A drop of oil was put on top of the culture medium on order to prevent drying during the experiment.

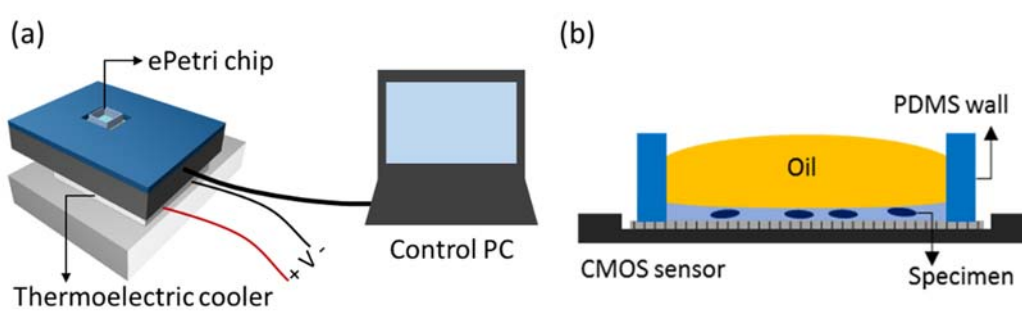


Figure 3 - 1. Schematic diagram of ePetri device for SPSM imaging of motile microorganisms. (a) ePetri dish imaging platform is composed of an ePetri chip, camera module and a control computer. A Peltier module and a heat sink are used to maintain the temperature of the chip. (b) Schematic diagram of a single ePetri dish chip. Sample is dispensed into a chip and a drop of oil is used to prevent evaporation of the medium.

SPMM imaging of motile microorganisms with ePetri platform does not require a use of special light source, and can use the room lighting or natural lighting for illumination. We used a green LED lamp (0.2 W/m^2) in all experiments as an illumination source to keep the phototaxis level identical in all cultures. Under this illumination condition, 0.2 ms exposure for single frame was found to be adequate. Since the camera board can exhibit elevated temperature during the course of long term imaging, we used a Peltier module and a heat sink to dissipate the heat from the board.

We used MT9P031 (2.2 μm pixel, Aptina) image sensors. We removed the color filter and the microlens layer by treating the sensor under oxygen plasma for 10 min (120W). The PDMS wall is prepared by mixing 1:10 with base and curing agent, then spin coated on a 3 in. silicon wafer followed by baking at 80°C for 1 h. The surfaces of ePetri chips are treated with Poly-L-lysine (0.01%, Sigma-Aldrich) for 15 min and washed with distilled water for three times.

3.3 SPSM imaging of *Euglena gracilis*

Pixel super-resolution image reconstruction in SPMM method requires a sequence of shadow images where the target object is continuously translated. The raw images captured through the sensor can be considered as undersampled images of the original object with a known sub-pixel shift between each frame. Upon reconstruction, the low resolution images are enhanced by m times, meaning that the physical size that a single pixel represents decreases by the factor of $1/m$ in the reconstructed high resolution image. This sub-pixel shift ($[d_{x,k}, d_{y,k}]$ for k^{th} image in the sequence) determines the vector in which m^2 different low resolution shadows are redistributed within the denser pixel grid of a single high resolution image. However, unlike SPSM method where a scanning light source creates shadows that are incrementally shifted with the fixed amount of displacement along both x and y direction, SPMM method is based entirely on the inherent motion of the microorganisms. This implies that we need to accurately trace and calculate each microorganism's position in every frame. As such, the sub-pixel shifts, from here on referred to as motion vector, of each cell is obtained by tracing the each cell's rough position throughout the low resolution sequence. Details on the method in which we obtain motion vectors of the microorganisms and circumvent the reconstruction errors caused from the inadequate motion of the cells are discussed later in this paper.

We used *Euglena gracilis* for demonstration of SPMM imaging technique. *Euglena gracilis* is an ellipsoidal protozoan with the dimensions of approximately $60 \times 10 \times 10 \mu\text{m}$. It is well known that its motion is propelled by a long flagellum beating around the body, and it moves in a rototranslatory motion with the speed of about 100-400 $\mu\text{m/s}$ [7, 15, 16]. Its body is slightly tilted with respect to the axis of the movement[15]. Considering the motion parameters of *Euglena gracilis*, we set the imaging frame rate at 180 fps, where we typically used 16 - 25 images to reconstruct a single high resolution image with the enhancement factor $m = 4 - 5$. This length of the sequence represent the image of the cell during approximately 0.1 seconds, which typically gives 10-40 μm displacement of the microorganisms within the sequence and makes it safe to assume that the internal sub cellular

structures are static and the rotation perpendicular to the axis of translation is negligible. Due to the limitations in the data transfer rate of the camera, we used a smaller FOV of 400×200 pixels.

Figure 3 - 2 shows the comparison between the raw and the reconstructed high resolution image of an *Euglena gracilis* with $m = 5$. The motion vector for each *Euglena gracilis* cells were calculated using a simple image processing technique. In the low sequence, the center locations of the organisms were found in each frame with the 0.5 pixel accuracy and then these values are smoothed throughout the sequence to estimate the cell location with sub-pixel accuracy. To reduce the amount of computation in the image reconstruction, each image is cut with a fixed window size around the target cell (17×17 pixels) and used the relative sub-pixel shifts ($[d_{x,k}, d_{y,k}]$) for reconstruction. The raw sequence used for this reconstruction and the measured motion vector is shown in Figure 3 - 3.

Since the basic principle of imaging is similar to SROFM method, the ultimate optical resolution of SPMM is similar to that of SROFM, reported as $0.66 \mu\text{m}$ at best. The optical resolution of SPMM ePetri depends on the pixel size of the sensor, number of low resolution images used for the reconstruction and the motion of the microorganism. However, due to the erratic nature of the inherent motion of a microorganism, such as rotation, sudden change of direction and non-uniform speed, we can expect that the resolution would be poorer than the SROFM method. From the images we obtained with SPMM ePetri, we were able to observe a small bright feature with the FWHM of $0.95 \mu\text{m}$, which is comparable with the resolution of a 0.30 NA 10x objective lens ($0.92 \mu\text{m}$ resolution) used for comparison in Figure 3 - 2(c). With the enhancement factor of 5, Nyquist limit from the pixel sizes in HR image is $0.88 \mu\text{m}$. Using a higher enhancement factor may increase the imaging resolution, but the frame rate also needs to increase in order to acquire enough number of LR images without increase in the motion-induced blur and errors. In addition, the resolution would be poor for larger and thicker microorganisms, due to the increased distance between the imaging plane and the sensor's surface. The lower limit to the size of microorganism that can be imaged is determined by the pixel size of the sensor; cells that are far smaller than the pixel cannot be recognized in the raw image, and thus unable to trace the motion vector. With the $2.2 \mu\text{m}$ pixel sensor, we have previously traced and imaged $0.5 \mu\text{m}$ features (microspheres) using the pixel super-resolution algorithm in Chapter 2.

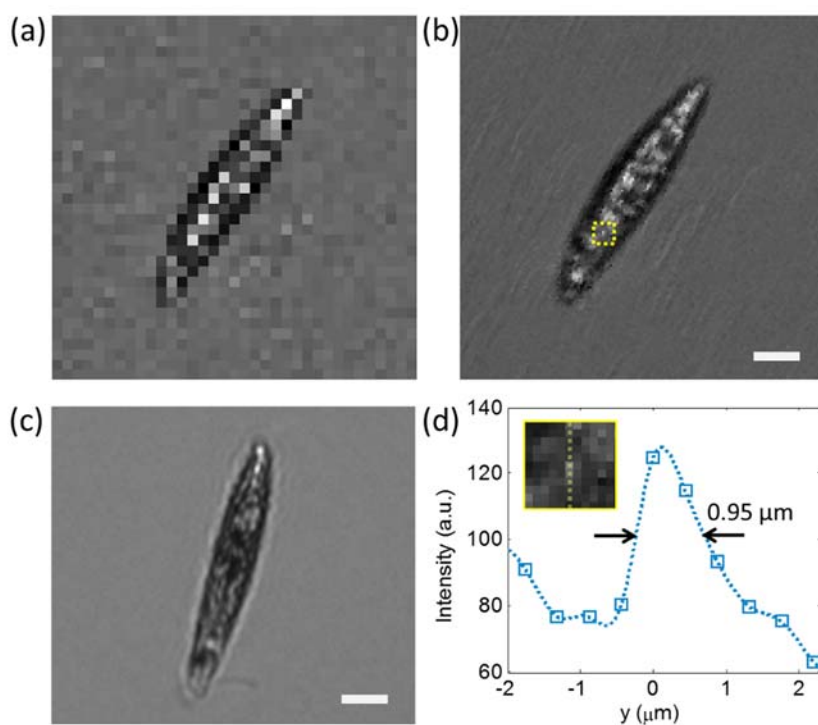


Figure 3 - 2. Raw (a) and reconstructed (b) images of *Englena gracilis* using SPMM method with $n=5$. (c) A conventional microscope image of a *Englena gracilis* taken with a 10x objective lens. The scale bar indicates $10 \mu\text{m}$. (d) The line traces of a small bright feature in the reconstructed image Inset corresponds to the area highlighted in (b).

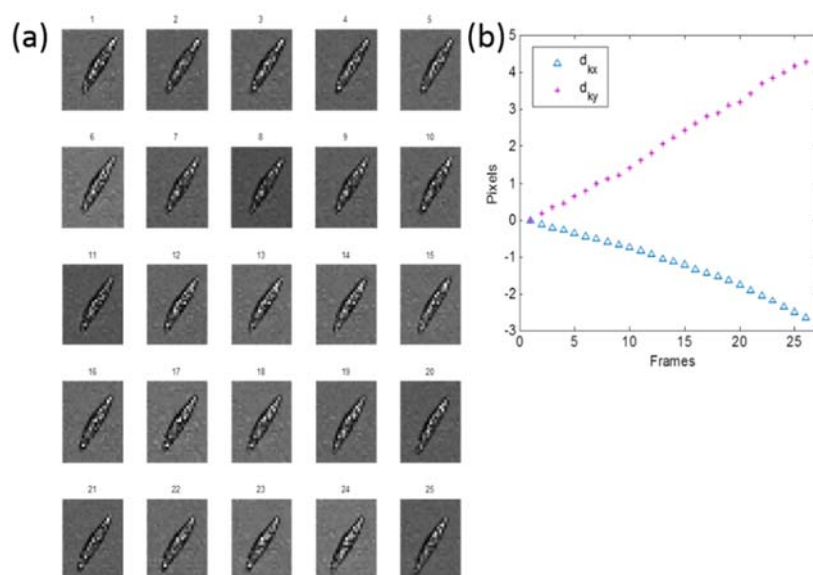


Figure 3 - 3. Motion of an *Englena gracilis* cell over 25 frames (a) and the motion vector obtained via our tracing program (b).

3.4 Motion artifacts in SPMM

3.4.1 Scanning direction

It is worth noting that there exist some criteria in the cellular motion for a proper image reconstruction. In order for the entire part of the cells to be scanned with sub-pixel displacement, the translation of the cells should be at a certain angle with respect to the sensor's pixel grid so that the sample is scanned with shifts in both x and y directions. Assuming the linear translation of the cells within a sequence of N frames, the motion vector should satisfy following condition.

$$\min(|d_{Nx}|, |d_{Ny}|) > 1 \quad (3,1)$$

When such condition is not satisfied, the sample is not entirely scanned and the reconstructed image shows empty pixels in a form of stripes (horizontal when d_{Ny} , vertical when d_{Nx} is not enough), with the period of the enhancement factor n (Figure 3 - 2b). In order to prevent missing information in the image, we obtain the low resolution sequence for a longer amount of time than 0.1 seconds, find the sequence where the angle of motion satisfies the a condition in (1) with minimum N (Figure 3 - 2b,c), or use more frames to satisfy (1).

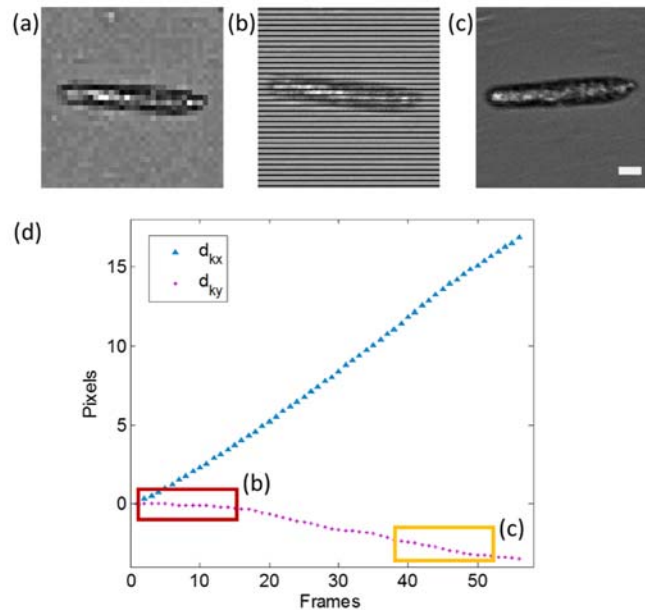


Figure 3 - 4. Artifacts in image reconstruction and improved images. Cells moving in horizontal direction show missing information in y direction and (c) a different sequence of the same cell with adequate motion vector showing a well-reconstructed image. (d) Motion vector for *Euglena gracilis* corresponding to images (a)-(c). The scale bar indicates 10 μm .

3.4.2 Rotation

Rotation of the cells can also cause artifacts in the reconstructed image. Although the rotation in a typical motion of a *Euglena gracilis* during the imaging period of 0.1 seconds is small compared to the translational component, the rotational frequency may increase depending on the condition of the cell and a cell may change its direction abruptly upon incidence with an obstruction. Figure 3 - 5b and Figure 3 - 6b show reconstructed images with periodic rotation artifacts at the tip of the microorganisms. To take the rotation of the cell into an account for the pixel super-resolution reconstruction, it is required to measure the changes in the angle of orientation of the cells in each frame. We used two approaches to measure the angle of a cell; one approach calculates the angle from the shape of the cells in the low resolution images and the other approach calculates it from the displacement of cells between each subsequent frames. For the elongated microorganisms, the rotation angle can be easily measured directly from the raw images (Figure 3 - 5d). For the round cells, we can use the fact that the cells are directed towards the direction of motion and calculate the angle from the motion vector (Figure 3 - 6d). The rotational motion of the microorganisms can be compensated by re-rotating each frame by the angle $-\theta_k$ during the reconstruction process. This rotation process can be described as below.

$$\mathbf{y}_{rk}(x, y) = \mathbf{y}_k(x \cos \theta_k - y \sin \theta_k + md_{k,x}, x \sin \theta_k - y \cos \theta_k + md_{k,y}) \quad (3.2)$$

where \mathbf{y}_{rk} represents k^{th} low resolution image up-sampled by the factor of m and \mathbf{y}_k represents k^{th} low resolution image up-sampled by m , shifted and rotated for prior to reconstruction. With the same set of low resolution sequence used for Figure 3 - 5 and Figure 3 - 6, we can reconstruct rotation-compensated images where the stripe-patterned artifacts are effectively removed. However, it is worth noting that the image blur caused by the cell rotation perpendicular to the axis of translation cannot be computationally removed. We minimize this rotation-induced blur by maximizing the frame rate such that the cell rotation within the low resolution sequence is negligible.

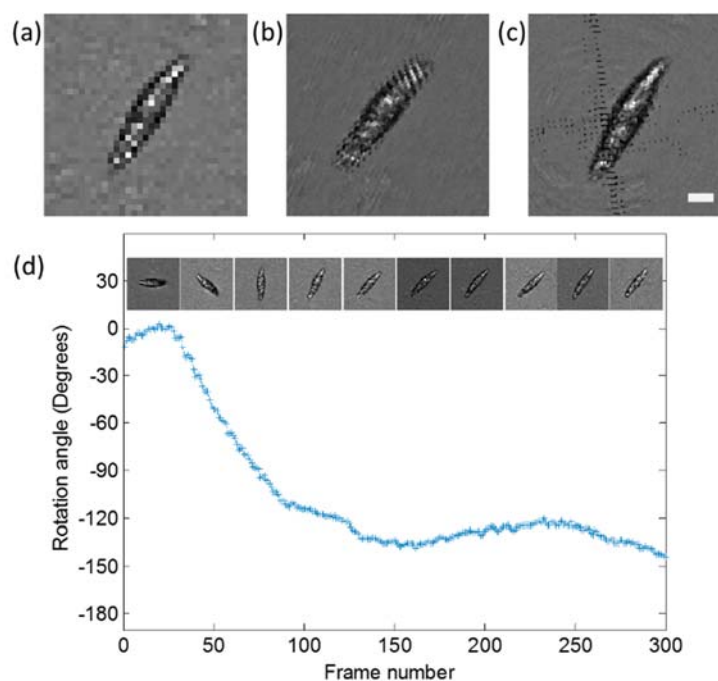


Figure 3 - 5. Cells with large rotational movement show artifacts at the two ends of the cell (b). Reconstructed image with rotation compensation (c). Rotation angle measured by the angle of the microorganism. The scale bar indicates 10 μm .

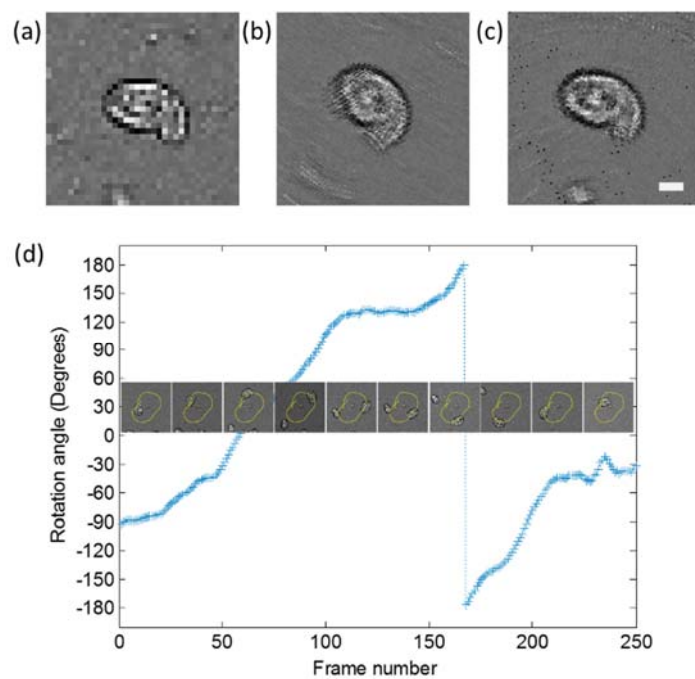


Figure 3 - 6. Cells with large rotational movement show artifacts at the two ends of the cell (b). Reconstructed image with rotation compensation (c). Rotation angle measured by the angle of the microorganism. The scale bar indicates 10 μm .

3.5 Longitudinal imaging of *Euglena gracilis*

To demonstrate longitudinal imaging and motion analysis capabilities, we cultured *Euglena gracilis* protist in our ePetri system. Long term culture monitoring and image-based motion analysis with ePetri system can benefit many biological assays and scientific studies using *Euglena gracilis*. Due to their sensitivity to the changes in the chemical environment, *Euglena gracilis* is used for various microbiological assays, including vitamin B12 assay and aquatic toxicity assays [4, 11, 17]. Their phototactic and gravitactic movement has been intensively studied and utilized as sensors [8, 18]. Their shape also changes under different illumination conditions [3].

Euglena cells were cultured in ePetri platform and continuously imaged for 10 hours. We used two image acquisition modes; Large field of view imaging with low frame rate (16 fps) for continuous monitoring and smaller field of view scanning with higher frame rate (180 fps) for SPMM high resolution image reconstruction. From the large FOV image, statistical analysis on cell counting, tracking (speed and trajectory), size and shape distribution (aspect ratio of the cells) can be obtained for >200 cells. For a closer look into each cell, we performed SPMM imaging by dividing the entire imaging area into smaller windows (400×200 pixels) to obtain sequences with higher temporal resolution. *Euglena gracilis* (Carolina scientific) was cultured in a custom made euglena medium (spring water, 40 L^{-1} wheat grains, 35 L^{-1} rice grains and $5 \text{ cm}^3/\text{L}$ dry skim milk, recipe provided by Carolina scientific) under natural sunlight illumination. All experiment was performed in room temperature where the *Euglena gracilis* are healthy and their reproduction is well promoted.

Figure 4a shows growth of euglena cells cultured in an ePetri system. $5 \mu\text{L}$ of euglena medium containing 140 cells were dispensed into an ePetri chip and cultured at room temperature with a green LED illumination ($0.2 \text{ W}/\text{m}^2$). Two snapshots of the culture at 1 hr and 5 hr show distinct increase in the cell population in the culture. HR images reconstructed using SPMM method reveal details in the shape, size and opacity variations in each microorganisms (Figure 3 - 8). We observed *Euglena gracilis* in various stages of growth including young euglena cells with elongated shapes, old rounded cells, cells undergoing mitosis and non-motile palmella stage cells that are covered with mucilage. However, since SPMM method relies on the movement of the target cells, images of immotile cells such as mitotic, palmella stage and lysed cells cannot be reconstructed with enhanced resolution.

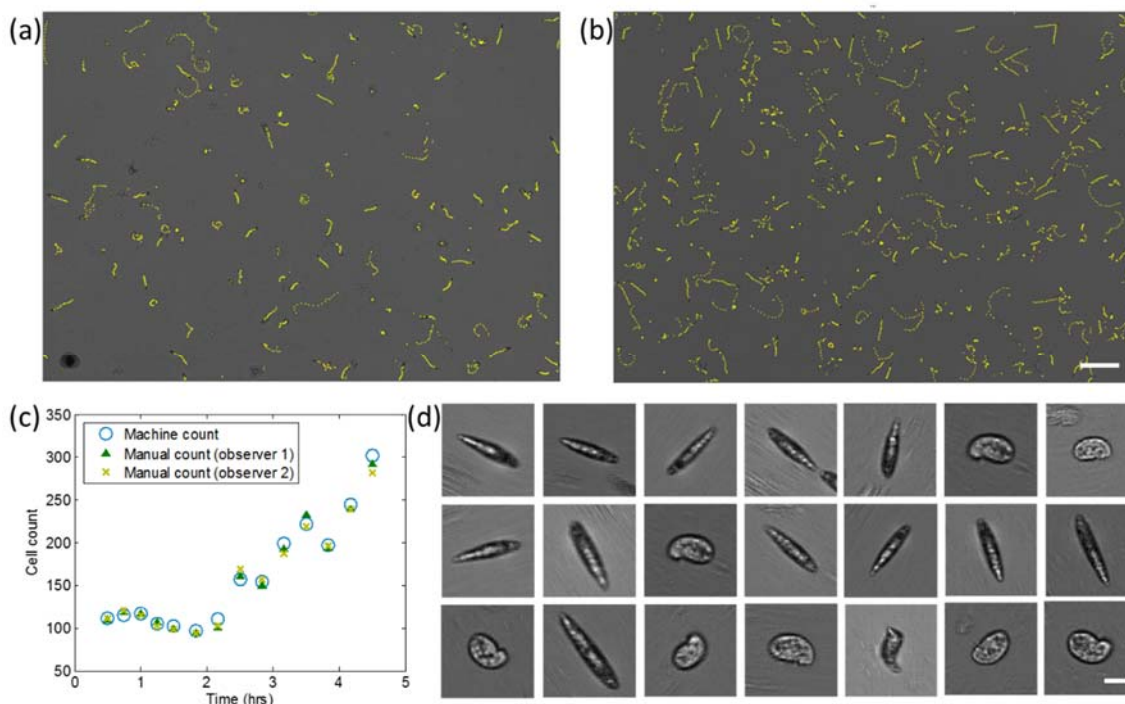


Figure 3 - 7. Longitudinal imaging of *Euglena gracilis* on ePetri dish. (a), (b) Large FOV images of *Euglena gracilis* at 1hr and 4.5 hrs, respectively. Yellow line shows traces of each cell for 1 second. (Scale bar 200 μm) (c) Growth in cell population counted with our cell counting software (blue) and manually counted (green, yellow). (d) High resolution images of *Euglena gracilis* reconstructed with SPMM method (selected). Scale bar indicates 20 μm .

Image analysis for cell counting was performed by first identifying each cell via thresholding the raw gray scale images (euglena cells or the boundary of euglena cells appear darker than the background), converting into binary image and then counting the number of areas within a predefined size range to filter out debris and noises. From the counting results, the growth of the cells showed clear increase with the doubling time of approximately 5 hours. To assure the accuracy of our cell counting software, our results were compared with manual counting results of 2 observers. The results showed the average percent difference of 3.0 % between the manual and the machine count, where percent difference between the observers is 3.1 %. (See Table 3 - 1 and Figure 3 - 7c). Subsequent analysis for cell tracking and shape analysis was performed with simple image processing techniques. We traced each cells for 16 frames (1 second) to obtain the speed of the cells, which is an important parameter for the status of the culture. The mean velocity of the cells remained within 10% variance during the 5 hour culture, indicating that the culture environment in ePetri dish was adequate.

	Machine	Observer A	Observer B	Machine-A (%)	Machine-B (%)	A-B (%)
Image 1	112	112	110	0.00	1.80	1.80
Image 2	121	115	119	5.08	1.67	3.42
Image 3	115	117	117	1.72	1.72	0.00
Image 4	102	105	107	2.90	4.78	1.89
Image 5	99	102	99	2.99	0.00	2.99
Image 6	94	97	94	3.14	0.00	3.14
Image 7	103	111	101	7.48	1.96	9.43
Image 8	169	157	161	7.36	4.85	2.52
Image 9	157	154	150	1.93	4.56	2.63
Image 10	187	199	193	6.22	3.16	3.06
Image 11	219	222	233	1.36	6.19	4.84
Image 12	196	197	194	0.51	1.03	1.53
Image 13	239	245	239	2.48	0.00	2.48
Image 14	282	302	292	6.85	3.48	3.37
Average				3.57	2.51	3.08

Table 3 - 1. Cell counting results and percentage difference between the machine count and two manual count results.

Next we performed differential experiment with two sets of euglena cultures. We used spring water as medium for culture A and the euglena culture medium for culture B. Two cultures were kept in ePetri for > 5 hrs under same temperature and illumination conditions. We used our analysis software to obtain the distribution of the motility and the cell shapes. The result shows that the cells cultured in fresh water have more population of elongated cell types with high aspect ratio and lower motility, whereas larger population of *Euglena gracilis* cultured in the medium showed faster motion and rounded shapes.

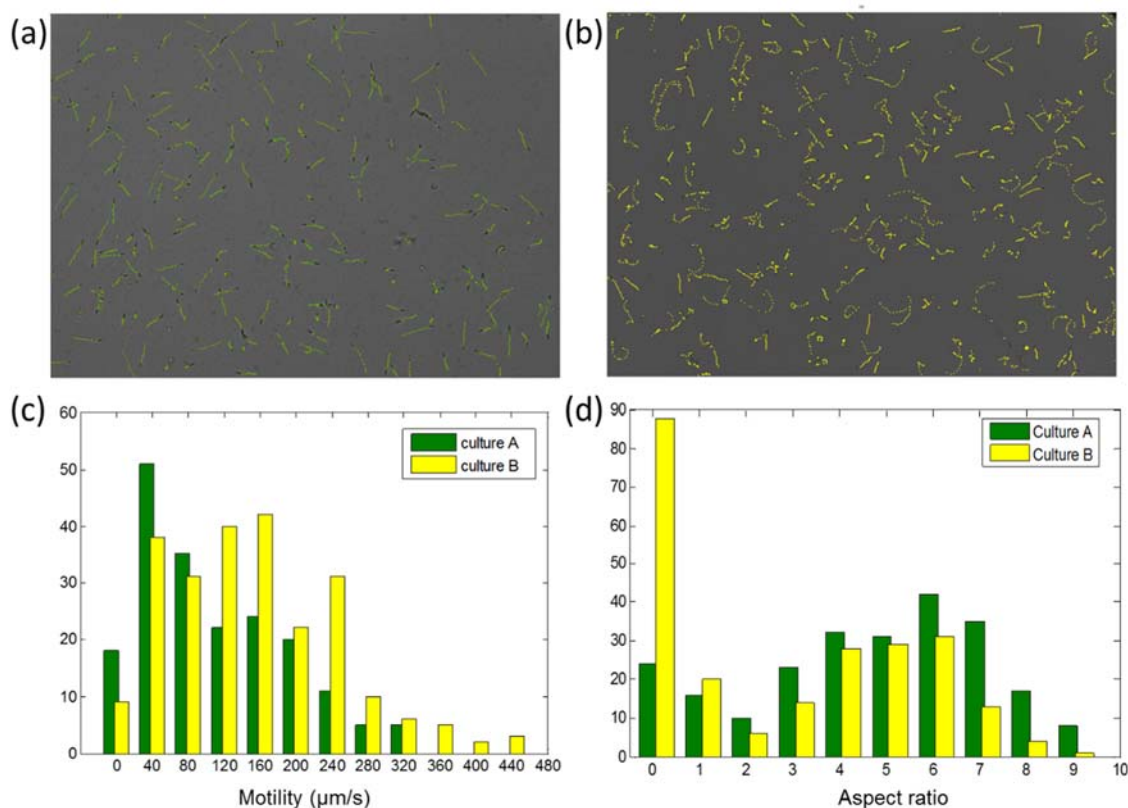


Figure 3 - 8. Motion tracking and shape analysis using ePetri. (a-b) *Euglenas* cultured in spring water (a) and in euglena medium. Scale bar indicates 200 μm . (b) shows difference in their motion and the cell sizes. (c) Motility distribution of the cells. (d) Aspect ratio (major axis / minor axis) distribution of the cells.

3.6 Conclusion

We demonstrated the imaging of motile microorganisms in an ePetri platform by using the inherent motion of the cells for the pixel super-resolution reconstruction. Rototranslatory movement of *Euglena gracilis* allows capturing of sequence shadow images with sub-pixel shifts, which allows for imaging individual cells with the enhanced resolution than the pixel size of the sensors. Using SPMM method, we achieve high resolution imaging over $5.7 \text{ mm} \times 4.4 \text{ mm}$ area without using any optical elements. In addition, we show long term culture of *Euglena gracilis* in a SPMM ePetri platform, and demonstrate image-based analysis for automatic cell counting, motion analysis and shape analysis.

This work, particularly focused on a motile microorganism, shows the versatility of our SPMM ePetri system in the choice of the sample and the type of information collectible through our system. The key advantage of our SPMM ePetri platform is that it lowers the labour and the cost of culture

experiments by miniaturizing and automating the monitoring system. The user can simply dispense the specimen on an ePetri chip and monitor the growth through our software with the minimum access to the culture. It can also improve the quality of experiments a by improving the temporal resolution of the monitoring and allowing for streamlined and parallel process.

BIBLIOGRAPHY

1. Zheng, G., S.A. Lee, Y. Antebi, M.B. Elowitz, and C. Yang, *The ePetri dish, an on-chip cell imaging platform based on sub-pixel perspective sweeping microscopy (SPSM)*. Proceedings of the National Academy of Sciences, 2011.
2. Lee, S.A., G. Zheng, N. Mukherjee, and C. Yang, *On-chip continuous monitoring of motile microorganisms on an ePetri platform*. Lab on a Chip, 2012. **12**(13): p. 2385-2390.
3. Häder, D.-P. and K. Vogel, *Simultaneous tracking of flagellates in real time by image analysis*. Journal of Mathematical Biology, 1991. **30**(1): p. 63-72.
4. Tahedl, H. and D.-P. Häder, *Automated Biomonitoring Using Real Time Movement Analysis of Euglena gracilis*. Ecotoxicology and Environmental Safety, 2001. **48**(2): p. 161-169.
5. Levin-Reisman, I., O. Gefen, O. Fridman, I. Ronin, D. Shwa, H. Sheftel, and N.Q. Balaban, *Automated imaging with ScanLag reveals previously undetectable bacterial growth phenotypes*. Nat Meth, 2010. **7**(9): p. 737-739.
6. Wei, G., P. Cosman, C.C. Berry, F. Zhaoyang, and W.R. Schafer, *Automatic tracking, feature extraction and classification of C. elegans phenotypes*. Biomedical Engineering, IEEE Transactions on, 2004. **51**(10): p. 1811-1820.
7. Ascoli, C., M. Barbi, C. Frediani, and A. Murč, *Measurements of Euglena motion parameters by laser light scattering*. Biophysical journal, 1978. **24**(3): p. 585-599.
8. Richter, P.R., M. Schuster, H. Wagner, M. Lebert, and D.P. Häder, *Physiological parameters of gravitaxis in the flagellate Euglena gracilis obtained during a parabolic flight campaign*. Journal of plant physiology, 2002. **159**(2): p. 181-190.
9. Waggoner, L.E., G.T. Zhou, R.W. Schafer, and W.R. Schafer, *Control of Alternative Behavioral States by Serotonin in Caenorhabditis elegans*. Neuron, 1998. **21**(1): p. 203-214.
10. Su, T.-W., A. Erlinger, D. Tseng, and A. Ozcan, *Compact and Light-Weight Automated Semen Analysis Platform Using Lensfree on-Chip Microscopy*. Analytical Chemistry, 2010. **82**(19): p. 8307-8312.
11. Ahmed, H. and D.-P. Häder, *A fast algal bioassay for assessment of copper toxicity in water using <i>Euglena gracilis</i>*. Journal of Applied Phycology, 2010. **22**(6): p. 785-792.
12. Breslauer, D.N., R.N. Maamari, N.A. Switz, W.A. Lam, and D.A. Fletcher, *Mobile Phone Based Clinical Microscopy for Global Health Applications*. PLoS ONE, 2009. **4**(7): p. e6320.
13. Farsiu, S., M. Robinson, M. Elad, and P. Milanfar, *Fast and robust multiframe super resolution*. IEEE Transactions on Image Processing, 2004. **13**(10): p. 1327-1344.
14. Sung Cheol, P., P. Min Kyu, and K. Moon Gi, *Super-resolution image reconstruction: a technical overview*. Signal Processing Magazine, IEEE, 2003. **20**(3): p. 21-36.
15. Ascoli, C., M. Barbi, C. Frediani, and D. Petracchi, *Effects of electromagnetic fields on the motion of Euglena gracilis*. Biophysical journal, 1978. **24**(3): p. 601-612.
16. Cramer, M. and J. Myers, *Growth and photosynthetic characteristics of Euglena gracilis*. Archives of Microbiology, 1952. **17**(1): p. 384-402.
17. Aoyama, K., K. Iwahori, and N. Miyata, *Application of Euglena gracilis cells to comet assay: evaluation of DNA damage and repair*. Mutation Research/Genetic Toxicology and Environmental Mutagenesis, 2003. **538**(1-2): p. 155-162.
18. Ozasa, K., J. Lee, S. Song, M. Hara, and M. Maeda, *Two-dimensional optical feedback control of Euglena confined in closed-type microfluidic channels*. Lab on a Chip, 2011. **11**(11): p. 1933-1940.

SUB-PIXEL PERSPECTIVE SWEEPING MICROSCOPY (SPSM)

In this chapter, we will discuss an alternative approach to perform pixel super-resolution reconstruction in chip-scale microscopy. Chip-scale microscopy techniques demonstrated in previous chapters (both SROFM and SPMM) rely on physical translation of the sample for resolution enhancement. However, for adherent samples, such as live cells in tissue culture and dried smear film of clinical specimen, translation-based scanning is simply inapplicable. Instead, we can exploit the fact that CMOS image sensors have a thin passivation layer which creates a slight separation between the top surfaces of the sensor to the photodiode layer. Because of this separation, we can translate the shadow of the sample by changing the angle of illumination and use the resulting sub-pixel shifted shadow images to perform pixel super-resolution reconstruction of high resolution images. Here on, we refer to this technique as sub-pixel perspective sweeping microscopy (SPSM) and discuss the implementation of ePetri prototype system using LED array illumination.

4.1 Imaging principle

The working principle of SPSM is illustrated in Figure 4 - 1a. The sample of interest sits still on the surface of a CMOS image sensor. As we discussed in previous chapters, the raw shadow image captured at the image sensor contains limited spatial information about the sample, due to the pixel size of the image sensor being in the order of micrometers range. However, due to the physical layout of the CMOS image sensors, where the top surface of the sensor is passivated with a thin transparent layer, there is a thin separation between the sample and the photodiode of the image sensor pixel. When we change the angle of illumination, this separation allows the corresponding shadow to laterally translate across the pixel array. By using incremental tilt/shift of the illumination in x-y plane, we can obtain series of sub-pixel shifted LR shadow images, which can then be reconstructed into a single HR image with the pixel super-resolution reconstruction.

The sweeping of the illumination angle can be achieved by laterally moving the location of the light source in 2D above the sample. Shadow imaging uses collimated illumination incoherent light, which can be achieved by placing a small light source at a sufficient distance away from the sample. For a light source of a LED ($\sim 1 \text{ mm} \times 1 \text{ mm}$), 5cm separation will result in the illumination angle difference of 1.1° at maximum, which is negligible. At the plane of light source, the scanning can be

easily achieved by using a 2D array of LEDs[1] or using a display panel as a light source[2]. In this chapter, we used a low-cost LED matrix for the sweeping light source, by sequentially turning on each LED in the matrix to perform sub-pixel raster scanning of the shadow images. The amount of sub-pixel shift of the shadow is proportional to the separation thickness of the sample and the image sensor. The sub-pixel shift can be expressed as ;

$$d_x = d_y = \frac{zH}{LP} \quad (4,1)$$

Where H is the distance between the illumination and the image sensor, z is the height of the imaging plane from the sensor plane, L is the pitch of the LEDs in the LED matrix and P is the pixel size in the image sensor. Number of LEDs in the matrix determines the maximum enhancement factor for the reconstruction process. Also, as in SROFM and SPMM scheme, the sub-pixel shift has to be at least 1 LR pixel, thus the illumination matrix needs to be designed such that

$$\frac{mH}{L} > \frac{P}{z_{\min}} \quad (4,2)$$

Where z_{\min} is the thickness of the separation layer. This thickness varies between the image sensor architecture. For the image sensor we used, this thickness is less than a micrometer. In our LED array, the pitch of the LED array is 7.5 mm and has 8×8 LEDs. We placed the LED 3.5cm away from the image sensor to satisfy this condition. Color imaging can be achieved by simply using RGB illumination, by acquiring each sequence at each color channel and then combining the image into one (Figure 4 - 1b). Note that SPSM only works with static objects (static for the time required to acquire raw sequence).

Reconstruction algorithm is similar to the pixel super-reconstruction used in SROFM and SPSM in Chapter 2-3. In SPSM, the sub-pixel shift in each frame is already known, thus the motion estimation step is unnecessary. In fact, since SPSM is based on precise raster scanning, the loss of resolution due to mis-registration of the LR images and error due to motion-blur is prevented. Also, we can simplify the registration step by only using the sub-pixel shift of integer multiples of $\frac{1}{M}$, without the bilinear interpolation step. However, the sweeping illumination scheme results in cross-hatch patterned image artifacts with thick samples, due to the varying sub-pixel shift in different height planes.

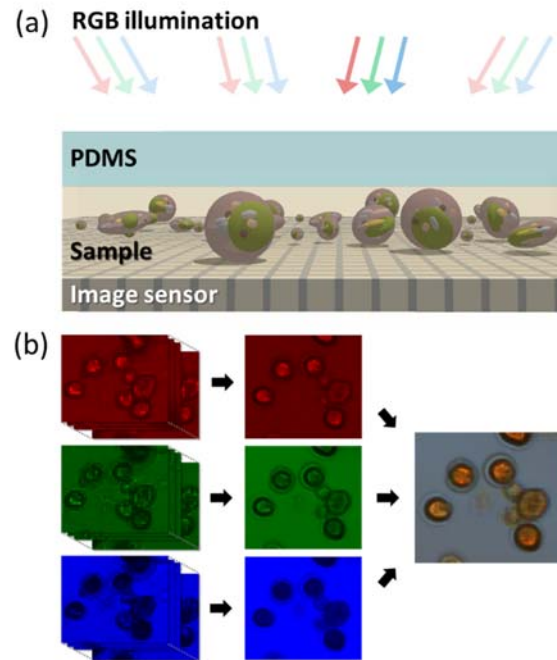


Figure 4 - 1. Schematic of the working principle of SPSM color imaging. (a) While the target objects rest on the surface of the image sensor, we sequentially turn on each LED in the RGB LED array illumination above and take sequences of low-resolution images. (b) Each low-resolution sequence is reconstructed into three monochromatic high-resolution images using the pixel super-resolution algorithm. The red, green, and blue channels are then combined into a single color image.

4.2 Waterborne parasite detection with SPSM

In this Section, we demonstrate a compact portable imaging system based on SPSM for the detection of waterborne parasites in resource-limited settings. The SPSM was originally designed to serve as a ePetri platform to image confluent culture of adherent cells grown on the surface of a CMOS image sensor[2]. Here, we show that its general and simple-to-use microscopy imaging capabilities can be used more broadly. Specifically, in this thesis, we show imaging and identification of waterborne parasites with the SPSM imaging system using a RGB LED array illumination. The three types of parasite cysts – Entamoeba, Giardia, and Cryptosporidium – are imaged and identified using the system. We further developed an automatic image reconstruction and screening method that can potentially be applied to digitalized diagnostic tests.

4.2.1 Background

Waterborne protozoan parasite infections occur worldwide and pose a public health risk in both developed and developing countries[3, 4]. Outbreaks of these diseases are typically transmitted via the fecal-oral route in association with contamination of drinking water and food, and poor sanitation

at recreational water venues[4]. Symptoms typically involve severe diarrhea and fever, which can be life-threatening for young children, immune-deficient patients, and those living in the developing parts of the world[3]. In cases of outbreaks, rapid and accurate identification of the infection is important for the effective treatment and management of disease transmission. Among many species of protozoan parasites, *Giardia lamblia*, *Cryptosporidium parvum*, and *Entamoeba histolytica* are common etiological agents in most outbreaks.

The gold standard for the diagnosis of these parasitic infections is microscopic analysis of stool samples, complemented by polymerase chain reaction (PCR) or antigen detection technology for confirmation. Direct or concentrated stool smears are stained and examined under a microscope to identify the parasites in their cyst forms. Although simple and effective, imaging-based examination requires microscopes and trained microscopists on-site and the sensitivity and specificity of the tests are variable, depending on laboratory personnel expertise. Tests based on PCR or antigen detection techniques can be more reliable[5], but involve specialized laboratories (medium-sized clinical facilities) with advanced equipment, and thus are unsuitable for field settings. For point-of-care diagnostics, rapid immunoassay kits have been developed, but are currently not available in a multiplex assay form (*Giardia* and *Cryptosporidium* combined only[6]). In rural settings or emergency outbreak scenarios, imaging-based tests can still be a reliable and cost-effective solution for rapid diagnosis, provided that the imaging device and the screening process can be miniaturized and simplified.

Here, we show that its general and simple-to-use microscopy imaging capabilities can be used more broadly. Specifically, in this study, we show imaging and identification of waterborne parasites with the SPSM imaging system using a light emitting diode (LED) array illumination. We demonstrate color imaging capability using a three-channel RGB LED array for identification of stained parasites. The three types of parasite cysts – *Entamoeba*, *Giardia*, and *Cryptosporidium* – are imaged and identified using the system. We further developed an automatic image reconstruction and screening method that can potentially be applied to digitalized diagnostic tests.

4.2.2 Device Construction

Figure 4 - 2 shows the imaging system used in the experiment. The prototype SPSM system consists of a CMOS camera, an 8×8 RGB LED array and a control board. For imaging, we load the sample directly on the CMOS image sensor so that the light transmitted through the sample can be

collected at the photodetector of each pixel in the image sensor. We used two schemes for sample loading. In one, microfluidic chambers were designed to contain a set volume of liquid sample and to hold the target object at the sensor's surface. The specimen could simply be pipetted into the chamber and allowed to settle for 5 min before imaging. In the other scheme, we made a wet film of the sample by placing a drop of liquid on the sensor and covering it with a cover glass or a transparent film. With both methods, the image sensor is reusable after flushing the channel and/or washing the sensor chip. Considering the low-cost of the semiconductor image sensors, the device can also be disposable.

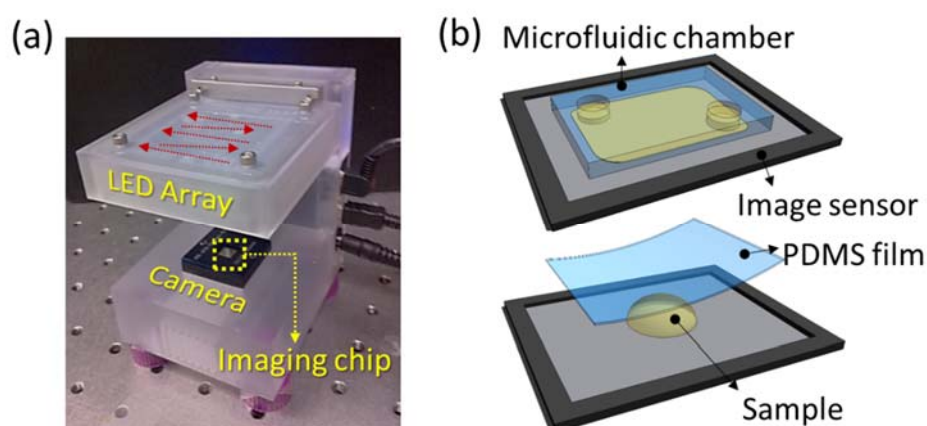


Figure 4 - 2. (a) Lens-less SPSM imaging system prototype. (b) A CMOS image sensor with a microfluidic chamber mounted on the sensor surface for sample loading (top). A sample slide can be made directly on the image sensor (bottom).

Once the sample is loaded onto the sensor, we sequentially turn on each LED in the 8×8 LED array. As the illumination scans, the image sensor captures the light transmitted through the sample under each LED. The raw images have low resolution (limited by the pixel size of the image sensor) but each frame of raw sequence is shifted with respect to the next due to the varying angle of incidence in the scanning illumination. The pixel super-resolution reconstruction accounts for the different spatial information in the each of 64 low resolution images and restores a single HR image ($8 \times$ reduction in the pixel dimensions). For color imaging, we use three color LED illuminations to obtain red, green, and blue channels and then combine the images into a color image. We use custom software that controls the LED array and the camera for the image capture. Once the data is acquired, the user can reconstruct high-resolution images of any area of interest with the software.

We used three types of parasite cysts for imaging. *G. lamblia* and *E. invadens* cysts were obtained from in vitro cultures of trophozoites[7, 8]. *E. invadens* is used as a model for *E. histolytica* because it can be induced to form cysts in vitro[9]. *C. parvum* oocysts were purchased from Excelsior Sentinel, Inc. Cysts were stained in suspension in Lugol's iodine (0.005%) or methylene blue (4.4 μM) before use.

Our optimized SPSM system used Aptina MT9P031 image sensors (2592×1944 pixels, pixel size $2.2 \mu\text{m}$) as its sensing substrates. We removed the cover glass and the microlens array on each sensor surface (oxygen plasma cleaning, 120 W, 10 min) for direct access to the sensor pixels. Polydimethylsiloxane (PDMS) microfluidic channels were fabricated via a standard soft-lithography procedure and bonded onto the image sensor after oxygen plasma treatment (40 W, 30 s). Image sensors were reused after cleaning with deionized water in an ultrasonic bath for 30 s.

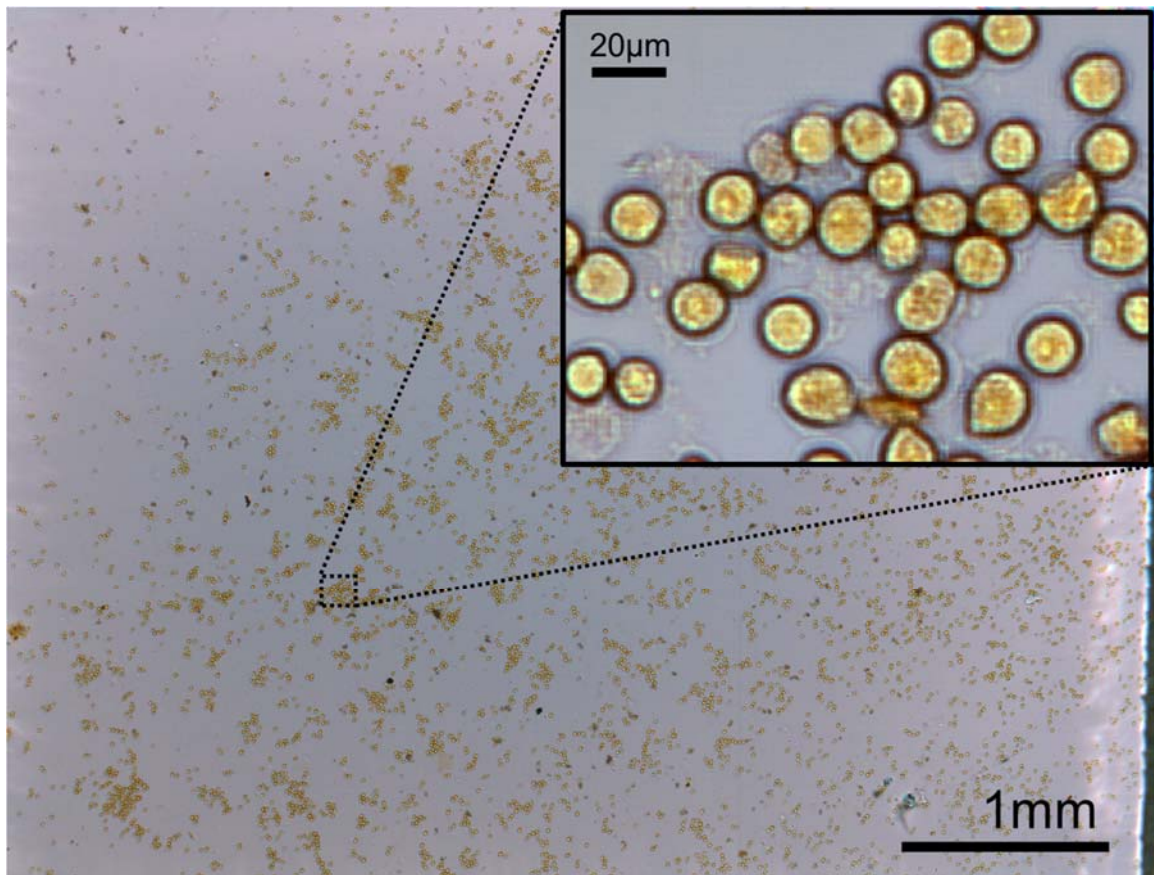


Figure 4 - 3. Full field-of-view ($5.7 \text{ mm} \times 4.3 \text{ mm}$) of *E. invadens* cysts with iodine staining. The inset shows part of the reconstructed image.

4.2.3 Color SPSM imaging of waterborne parasites

Figure 4 - 3 shows a full-field image taken with our chip-scale microscope. A wet film of the *E. invadens* cysts was made directly on an image sensor by the method illustrated in Figure 4 - 2b. Previously, we have experimentally demonstrated 0.66 μm resolution with the SPSM technique (with 13×13 scanning and 2.2 μm pixels), comparable to conventional microscope images taken using a 20 \times objective lens with a NA of 0.4. With 8×8 scanning, we expect that the resolution will be limited to three high-resolution pixels, which is 0.83 μm . The imaging area in the sensor measures 25 mm^2 , whereas the FOV of a 20 \times objective lens (Olympus, Plan N, NA 0.4) measures approximately 1 mm^2 . The data acquisition time is 2 min for 192 frames (64 frames for each color) and the raw sequence of the full FOV measures 930 megabytes.

Due to the large file size, the reconstruction of the full FOV takes a few minutes using a personal computer with an Intel i3 processor. However, the full-field high-resolution images are too large (20736 \times 15552 pixels) to display on one screen. Instead, the user can zoom to a smaller area of interest, and the image can be reconstructed within a few seconds. Additionally, we implemented an automatic image reconstruction software, which detects all particles in the FOV from the raw image and returns reconstructed images cropped around each particle. The automatic detection and reconstruction further improves the reconstruction speed and can be streamlined with the image screening process for diagnosis.

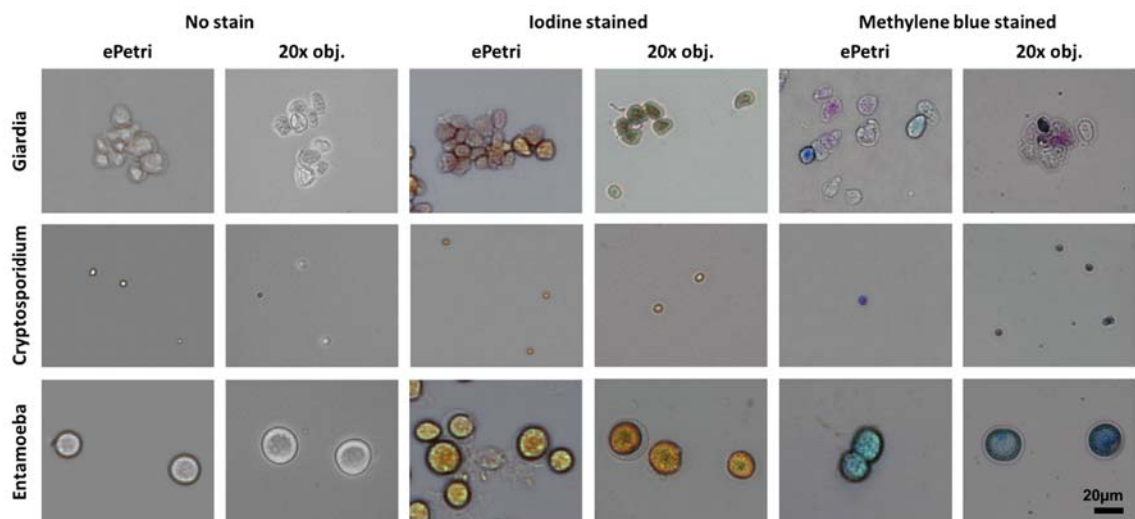


Figure 4 - 4. SPSM and 20 \times objective microscope images of *Giardia*, *Cryptosporidium*, and *Entamoeba* cysts. We imaged unstained cysts, iodine-stained, and methylene blue-stained cysts.

To demonstrate the imaging capabilities, we imaged three species of enteric parasite cysts with different types of staining (Figure 4 - 4). Entamoeba, Cryptosporidium, and Giardia can be found in the stool of infected patients in cyst form, and the recovery of these cysts is a crucial part of the diagnosis. Iodine and methylene blue staining are widely used for the distinction of these cysts from other particles and debris in the fecal smear. In Giardia, different degrees of encystation are observed and differentiated by the varying intensity of staining, which is clearly observed in the SPSM images. The comparison with a 20× objective lens microscope images shows that our SPSM images provide enough resolution and color for the identification of these parasite cysts, especially with appropriate staining.

Our chip-scale microscope is advantageous for imaging a large number and a wide variety of target samples. Unlike digital-holography based techniques, the SPSM technique does not impose constraints on the target object, such as confluency or scattering properties. With the SPSM, confluent cells and high-density smears can be imaged without the loss of resolution. Thus, we can screen more cells within the fixed imaging area. Additionally, the sample preparation steps and the resulting images of the SPSM technique are similar to conventional microscopy. This indicates that the experimental protocol and the diagnostic standards of conventional microscopy-based tests can be applied to our chip-scale microscopy technique without considerable modifications.

The SPSM method allows for digital refocusing of the images [1]. Each LED in the array illuminates the target object at a specific angle; thus, the sub-pixel shift between each frame varies with the vertical location of the target object. In the pixel super- on the same chip, where the variations in the cyst sizes (5 - 25 μm) cause the cells to be placed in different imaging planes. From a single set of raw data, we can reconstruct high-resolution images focused at different heights, by using the simple linear relationship between the sub-pixel shift and the imaging depth[1] ($z = 0$ at the surface of the image sensor). In addition, large clumps of cells can be resolved vertically to correctly account for the number of cells.

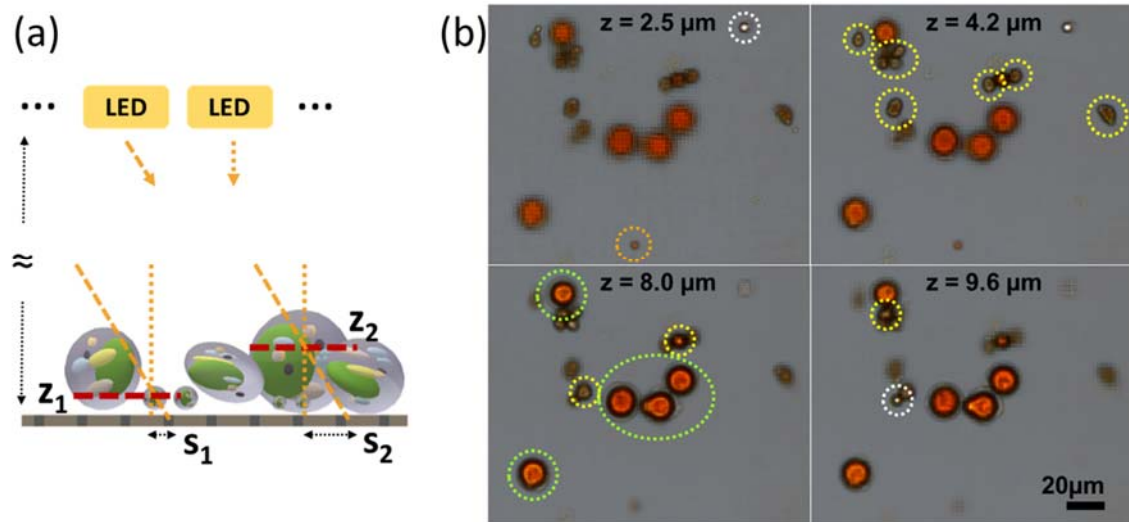


Figure 4 - 5. Digital refocusing of SPSM. (a) Refocusing is based on the difference in sub-pixel shift at different height planes. (b) Digitally refocused images of parasite cysts. Entamoeba (blue), giardia (red), and cryptosporidium (black) can be found in different z -planes. 4.3.4. Image-based identification of parasite cysts

4.2.4 Identification of parasite cysts

To verify the diagnostic potential of the SPSM technique, we performed a blind experiment with images of Entamoeba, Giardia, and Cryptosporidium cysts. In the experiment, we asked two experienced researchers to identify the parasite species from randomized images. The researchers were given 60 randomized images of each cell type, taken with both SPSM and conventional microscopy (Figure 4 - 6). In total, 360 images were analyzed. The samples used in the experiment were from separate batches of purified culture and the samples were stained with iodine. From this experiment, we were able to establish the identification accuracy of manual counting with 95% confidence intervals. The accuracy of the identification was comparable between conventional microscopy and SPSM images. This result indicates that images taken with the SPSM are suitable for distinguishing between the three parasites. The relatively low accuracy for Giardia in both SPSM and conventional images can be attributed to the variable sizes and shapes in the Giardia cyst sample.

Our positive results prompted us to investigate the possibility of further streamlining the identification process, using an image-based automatic identification algorithm. We implemented an algorithm to first detect the particles in the images based on the color and brightness variation. Next, we used the area, diameter, aspect ratio, and convexity of the particles to identify the types of cysts. We optimized the algorithm by training it on a set of known SPSM cyst images (500 of each parasite

species for a total of 1500 samples). We then tested its accuracy on the same set of images as was used in the manual experiment described above. The algorithm's accuracy is listed in Table 1. The algorithm performed slightly worse than manual counting but was nevertheless able to achieve a high level of accuracy. The errors were mostly attributable to clumps of cysts and irregularities. With the accuracy achieved, we believe that our automated identification can be applicable to the screening of parasite cysts in stool smear samples as a means to expedite diagnosis.

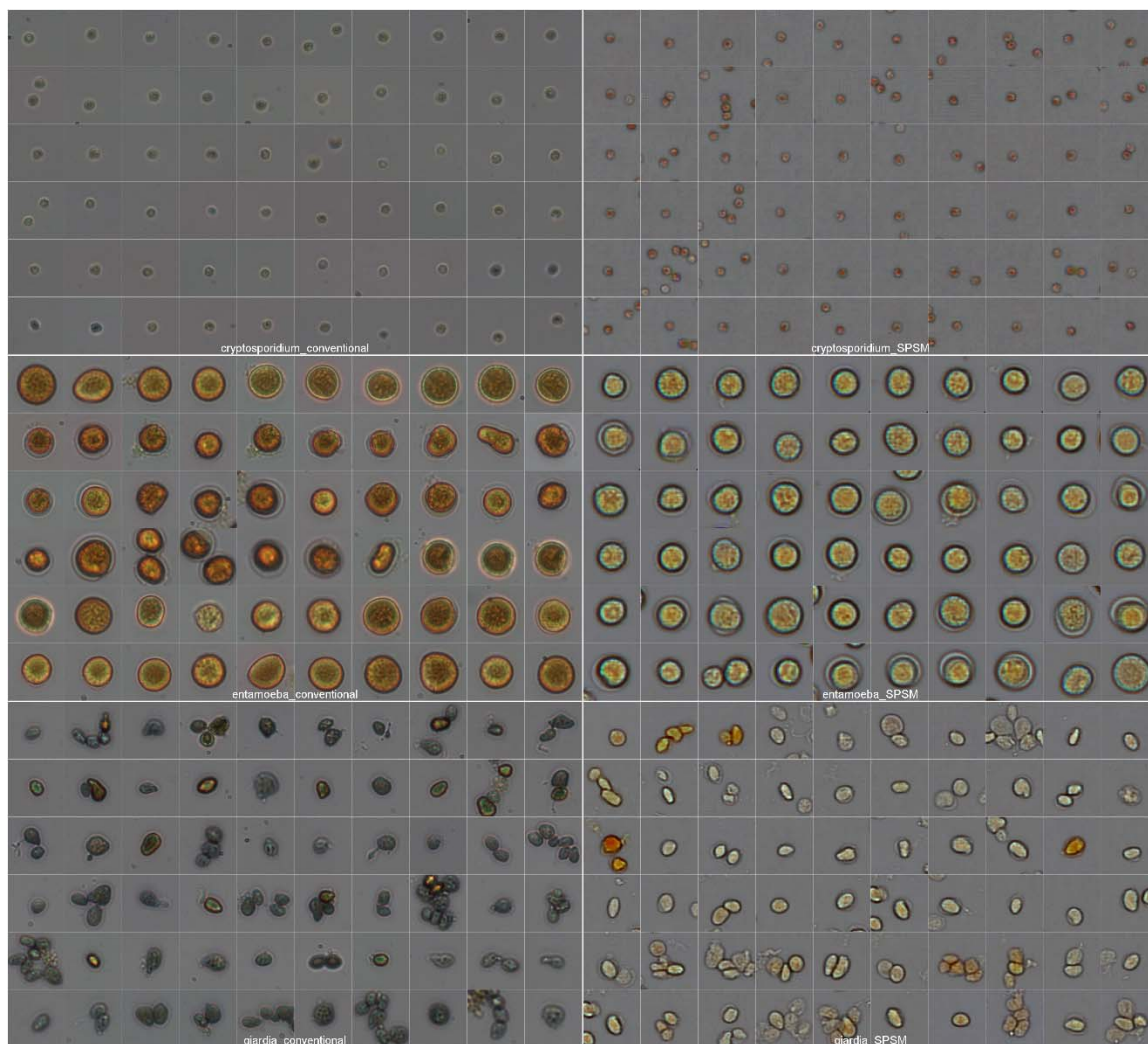


Figure 4 - 6. Images used in the identification experiments. 20× objective microscope (Left) and SPSM (Right) images of *Cryptosporidium* (top), *Entamoeba* (center) and *Giardia* cysts (bottom) used for the blind experiment and the automatic cell identification experiments.

Sample	Method	Accuracy (%)	False Positive Rate (%)	False Negative Rate (%)
<i>Cryptosporidium</i>	Conventional (manual)	100	0	0
	SPSM (manual)	100	0	0
	SPSM (automatic)	98	2.5	1.7
<i>Giardia</i>	Conventional (manual)	97	0	8.3
	SPSM (manual)	98	0	5
	SPSM (automatic)	96	2.5	6.7
<i>Entamoeba</i>	Conventional (manual)	100	0	0
	SPSM (manual)	100	0	0
	SPSM (automatic)	98	0.8	3.3

Table 4 - 1. Results of cell-type identification tests with conventional and SPSM images.

4.3 Discussions

We have demonstrated on-chip color imaging of waterborne protozoan parasite cysts with the SPSM technique using LED array illumination. The proposed system achieves ultra-wide FOV (25 mm²) and high imaging resolution (< 1 μm) with color capability. We showed that the system is capable of imaging three major types of water-borne parasite cysts, *Entamoeba*, *Giardia*, and *Cryptosporidium*, and the resulting images are suitable for both manual and automatic identification of the cyst types. We believe that, with further development, our chip-scale microscope can potentially provide a low-cost and portable solution to microscopy-based diagnosis of waterborne parasite infection in resource-poor settings.

The experimental format here is limited in scope in that it verified that the SPSM was able to distinguish between the parasites if they are the only objects present in the sample. To tackle parasite identification in a stool smear sample, the envisioned system would have to be able to distinguish parasites apart from generic particulates. While we expect image analysis would allow such a distinction to be made, the far larger proportion of generic particulates would likely negatively impact on the accuracy of such an analysis, even if the false-positive identification rate is low. We believe that one viable approach to this challenge would be to use fluorescently tagged antibodies that would preferentially attach to the parasites to help screen out generic particulates. We note that a small proportion of the generic particulates may also be fluorescently tagged, and thus lead to false-positive identifications. However, the combination of both image and fluorescence tagging should lead to a greatly suppressed false-positive rate.

BIBLIOGRAPHY

1. Zheng, G., C. Kolner, and C. Yang, *Microscopy refocusing and dark-field imaging by using a simple LED array*. Opt. Lett., 2011. **36**(20): p. 3987-3989.
2. Zheng, G., S.A. Lee, Y. Antebi, M.B. Elowitz, and C. Yang, *The ePetri dish, an on-chip cell imaging platform based on sub-pixel perspective sweeping microscopy (SPSM)*. Proc. Nat'l. Acad. Sci., 2011. **108**(41): p. 16889-16894.
3. Baldursson, S. and P. Karanis, *Waterborne transmission of protozoan parasites: Review of worldwide outbreaks – An update 2004–2010*. Water Research, 2011. **45**(20): p. 6603-6614.
4. Karanis, P., C. Kourenti, and H. Smith, *Waterborne transmission of protozoan parasites: a worldwide review of outbreaks and lessons learnt*. Journal of Water and Health, 2007. **5**(1): p. 1-38.
5. Haque, R., S. Roy, A. Siddique, U. Mondal, S.M.M. Rahman, D. Mondal, E. Houpt, and W.A. Petri, *MULTIPLEX REAL-TIME PCR ASSAY FOR DETECTION OF ENTAMOEBIA HISTOLYTICA, GIARDIA INTESTINALIS, AND CRYPTOSPORIDIUM SPP.* The American Journal of Tropical Medicine and Hygiene, 2007. **76**(4): p. 713-717.
6. Minak, J., M. Kabir, I. Mahmud, Y. Liu, L. Liu, R. Haque, and W.A. Petri, *Evaluation of Rapid Antigen Point-of-Care Tests for Detection of Giardia and Cryptosporidium Species in Human Fecal Specimens*. Journal of Clinical Microbiology, 2012. **50**(1): p. 154-156.
7. Luján, H.D., M.R. Mowatt, and T.E. Nash, *Mechanisms of Giardia lamblia differentiation into cysts*. Microbiology and Molecular Biology Reviews, 1997. **61**(3): p. 294-304.
8. Xu, W., M.H. Jericho, I.A. Meinertzhagen, and H.J. Kreuzer, *Digital in-line holography for biological applications*. Proceedings of the National Academy of Sciences, 2001. **98**(20): p. 11301-11305.
9. Sanchez, L., V. Enea, and D. Eichinger, *Identification of a developmentally regulated transcript expressed during encystation of Entamoeba invadens*. Molecular and Biochemical Parasitology, 1994. **67**(1): p. 125-135.

SMARTPHONE-BASED CHIP-SCALE MICROSCOPE FOR PORTABLE IMAGING

Portable microscopic imaging systems are in high demand for personalized medicine, global healthcare and environmental monitoring. For example, diagnostics for many third-world diseases, such as blood-borne diseases, water-borne parasite infections and bacterial infections, require microscopic inspection of bodily fluids or cells/tissue samples [1-6]. Also, microscopic analysis of environmental specimen is a crucial step of water quality monitoring and environmental pathogen screening [7]. A low-cost, light-weight portable imaging systems can greatly improve and simplify the way these tests are conducted. In this chapter, we present the implementation of chip-scale microscopy on a smartphone platform for portable imaging applications.

5.1 Background

Recent advances in smartphone technology are transforming global healthcare and remote sensing. Smartphone penetration is expected to surpass 60% of the global population by the end of 2019[8]. Modern smartphones deploy high computing power compatible to personal computers, mobile network connectivity and complex sensor technologies, all integrated in a palm-sized geometry. In particular, camera modules in smartphones employ state-of-the-art image sensors with small pixel sizes and high pixel counts, currently up to 40 Mega pixels. Microscopes using these built-in camera modules allow for compact and portable digital imaging platform for field applications. In addition, the connectivity of these mobile devices opens up various opportunities for telemedicine and remote diagnostics in resource-limited settings[9-11].

Many efforts have been demonstrated to construct a compact microscope on mobile devices. One of the initial approaches was to add an objective lens atop of a camera module of a mobile phone [12]. These imaging systems can be attached to any mobile phones without modification of the device, realizing low-cost microscopes for the mass. The performance of these microscopes is determined by the design of the optical systems, where increased resolution results in the limited field-of-view (FOV). Lensfree microscopes on mobile phones based on digital inline holography method has been demonstrated [13]. While these microscopes provide compact and light-weight design ideal for field applications, the reconstruction based on iterative phase-recovery algorithm is computationally heavy for mobile devices. Smart-phone based contact microscopy method has been developed to image

highly dense or connected samples, with the attachment of tapered fiber-optic array over the camera module [14].

So far, we demonstrated the feasibility of implementing lensless chip-scale microscopy using shadow imaging and pixel super-resolution algorithm. The general strategy requires the sample be placed on the surface of the image sensor. The shadow image casted by the sample upon light illumination is collected with the resolution determined by the sensor's pixel size. We then improve the image resolution via the pixel super-resolution image reconstruction of multiple low resolution images taken with sub-pixel shifts between each frame. We demonstrated this sub-pixel scanning by flowing the sample through a microfluidic channel (SROFM)[15], by using the inherent motility of the biological sample (SPMM)[16] and by varying the angle of illumination (SPSM) [17]. In SPSM technique, we have used moving light sources, such as the bright pixels in a smartphone screen or a light emitting diode (LED) array, which creates sub-pixel shifted shadows on the detector surface. With these scanning strategies, we have constructed sub-micron-resolution imaging systems with ultra-wide field-of-view (FOV) in a compact and lensless scheme. Furthermore, direct shadow imaging technique does not impose strict requirements on the light source, such as bandwidths or coherency, which simplifies the device design. Also, image reconstruction using pixel-super resolution algorithm does not require high computing power and can be performed on smartphone processors. For these reasons, our chip-scale imaging technique holds a solid ground for applications in mobile microscopy.

In this work, we report on the construction of a portable chip-scale microscope on a smartphone platform. Our device is based on the SPSM method, but with a fixed single light source rather than a sweeping source. Instead, we use the user's hand motion to perform angular scanning of the illumination. This scheme eliminates the illumination design as well as the lenses, thus allowing for a simple, low-cost and compact imaging device that is only composed of an image sensor. To obtain high-resolution images, we perform sub-pixel scanning by manually tilting the device around an ambient light source, such as the sun or a lamp, and process the raw images with the pixel-super resolution algorithm. Image acquisition and reconstruction is performed on a custom built application, constructing a stand-alone portable imaging device for field applications. Our prototype devices are constructed on android smartphones and achieve sub-micron resolution over an ultra-wide FOV. We demonstrate the working principle of our smartphone microscope and evaluate the performance of

our prototype device. We envision that our smartphone microscope can be a good fit for outdoor imaging applications where the user can perform microscopy imaging with sunlight illumination.

5.2 Working principle

The working principle of our smartphone microscope is shown in Figure 5 - 1. The technique is based on the shadow imaging method where the sample is placed directly on the surface of the image sensor. The light transmitted through the sample is collected at the photodiode of each pixel in the image sensor, providing direct shadow images with the resolution limited by the size of the pixels. To improve the imaging resolution, a sequence of images are captured with the varying angle of illumination as the user tilts the device around the light source, such as the sun or a lamp. Then, the captured raw sequence is processed with pixel super-resolution algorithm and reconstructed into a single high resolution image with enhanced optical resolution. We implemented a prototype system on android smartphones, by modifying the built-in camera module (Figure 5 - 1b). Image acquisition and the processing is performed on the smartphone with a custom-built android application.

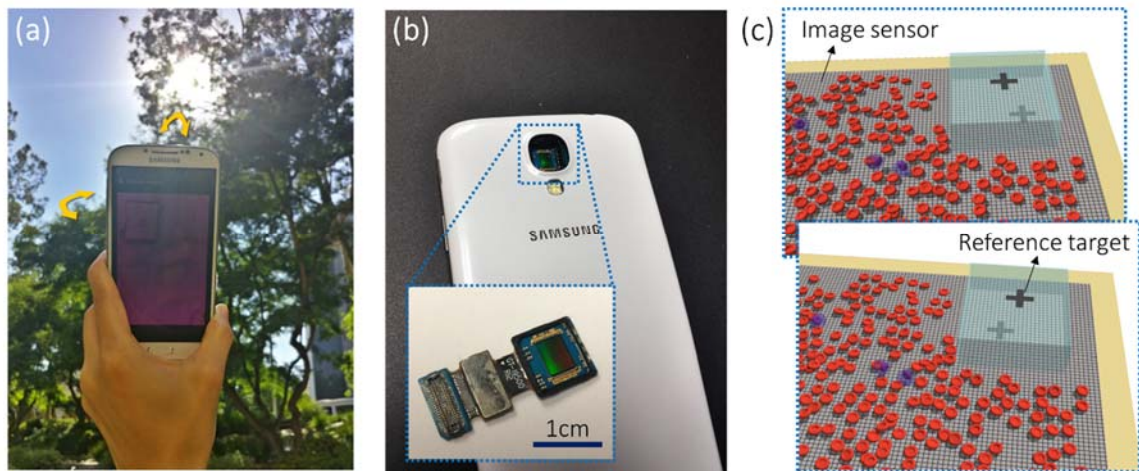


Figure 5 - 1. Working principle of the smartphone-based chip-scale microscope. (a) Using sunlight as the light source for imaging, the user holds the smartphone with the back camera module facing the sun, slowly moves the device to capture multiple images with varying angle of illumination. (b) The prototype device uses the back camera module of an android phone. We remove the lens module of the camera and place the sample directly on the surface of the image sensor. The inset shows the image sensor module with the lens removed.

The shadow imaging scheme does not require pre-designed illumination sources for imaging. The illumination can be any incoherent light from a single light source, for example, the sun, a flash light or a lamp, such that it creates a single shadow. By removing the illumination design, we can construct a truly compact and low-cost on-chip microscope for portable imaging needs. In this work,

we have demonstrated our imaging capabilities with sunlight, a LED flashlight and a fluorescent lamp. For the field applications, the user can simply point the camera towards the sun and acquire images. In the case of indoor use or in the presence of overcast, indirect illumination may cause multiple or diffused shadows. The user can instead obtain images with other illumination sources, such as a light bulb or a flashlight. To determine whether the illumination is suitable for imaging, we placed a known target object on one corner of the image sensor, such that the sharpness of the target's shadow can be used as an indicator (Figure 5 - 2). Due to the high intensity and unwanted infrared bands of direct sunlight, we attached an infra-red filter and a neutral-density filter (2 Optical density units) on the back cover of the smartphone. To test various illuminations, we imaged the same microspheres under an LED flashlight, a fluorescent lamp and the sun (Figure 5 - 6).

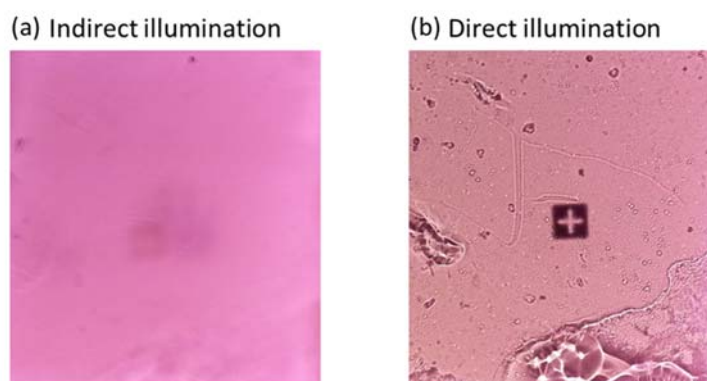


Figure 5 - 2. Shadow images of the reference target under the indirect and direct illumination. (a) The target image taken under the room light with multiple fluorescent bulbs and (b) under a flashlight. The target (cross-mark) is $200\ \mu\text{m} \times 200\ \mu\text{m}$ in size.

5.3 Device construction

5.3.1 Hardware design

Our smartphone microscope prototype uses the built-in camera module of a smartphone. The image sensor surface was revealed by simply removing the lens module in the back camera module of the smartphone. Figure 5 - 1b shows the modified camera module. The camera module parts are readily available for purchase and are very easy to replace. We used two smartphone models – Samsung Galaxy S3 and S4. The pixel sizes of the image sensor is $1.4\ \mu\text{m}$ and $1.1\ \mu\text{m}$, respectively. The total FOV is same as the size of the image sensor, which was $4.6\ \text{mm} \times 3.5\ \text{mm}$ for both devices. Due to debayering process in the camera, we cannot access the raw values of each pixel. Instead, we selected green pixels in the Bayer pattern, which occupy 50% of the pixels in the image sensor, and

rotated the image by 45° . The effective pixel size of the raw image becomes larger by the factor of $\sqrt{2}$, which is $1.98 \mu\text{m}$ and $1.56 \mu\text{m}$, with 50% areal fill factor.

Sample preparation step is identical to previous chip-scale microscopy techniques. Direct shadow imaging relies on the sample being in contact with the image sensor. For the experiments in this work, we made a dry or wet film of the sample on the image sensor. Mounting a microfluidic chamber or a cell culture well on the image sensor is also possible.

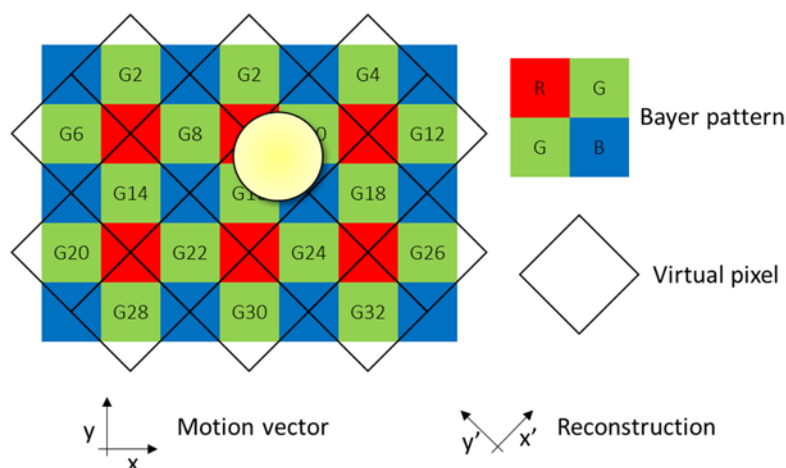


Figure 5 - 3. Layout of pixel geometry. Due to the debayering process in the camera module, we selected green pixels out of RGB bayer pattern and rotated the image 45° to obtain real images. The effective pixel size increases by factor of $\sqrt{2}$.

5.3.2 Android Application design

Figure 2 shows the workflow of the image acquisition. User starts the app and opens the camera to start image capture. The user is advised to point the camera towards the light source and tilt the camera in all directions. As the images are taken, the application calculates in real-time the tilt angle of each image, which is plotted in the screen and also saved in the memory for image reconstruction. After the image acquisition, the user can review and load the sequence of images, and select a smaller region for reconstruction (200×200 pixels). The program then crops the user defined region out of entire set of sequence, normalizes the images, and perform image reconstruction with the sub-pixel shift values measured in the image acquisition step. When the data is loaded directly from the memory (previously captured data), the application performs target tracing and image cropping/normalization simultaneously. The final reconstructed image is displayed in the screen and also saved automatically in the memory. Image normalization and cropping takes about 2 minutes for 100 frames, the delay is

mostly from accessing each image file in the memory. The high resolution image reconstruction takes few seconds for 200×200 pixels.

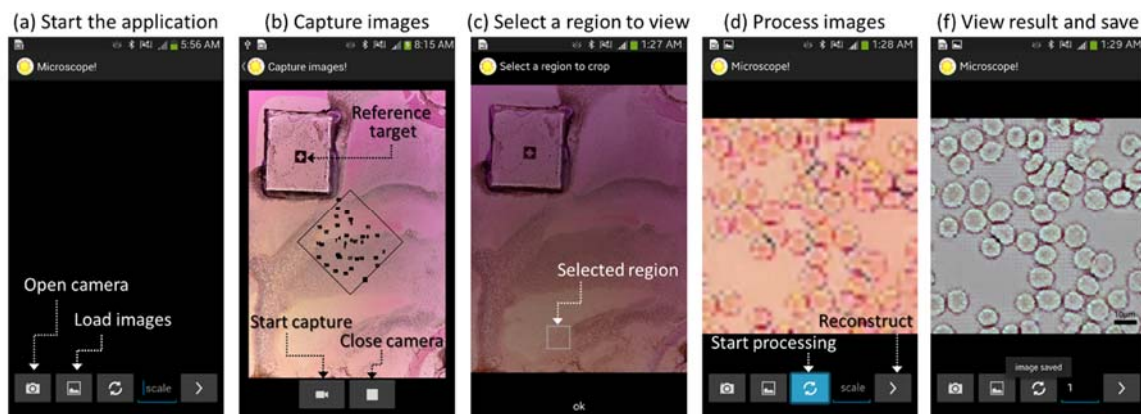


Figure 5 - 4. Imaging process of with the custom-built application. (a) Upon start, user can select to acquire new data using the camera, or load acquired images from the memory. (b) When capturing new data set, the user points the camera towards the sun and start capturing images. Reference target (a cross mark) shown in the upper left corner of the field of view is traced in each frame and the measured shifts are plotted over the camera view. Captured images are saved in the data storage, under a specified folder. Once the capturing is finished, user can choose to close the camera and return to the main window or to capture the data again. The sample used in this demonstration is unstained blood smear. (c) From the main window, user can select the load images button and load one of the acquired images from the gallery. The application prompts the user to select a smaller region to reconstruct. (d) Once a target region is selected, the application returns to the main window and plots the low resolution images of the selected region. The user clicks start processing button, and the application crops the entire low resolution sequence and pre-process the data to normalize the background and plots the measured tilt angles. (e) Once the pre-processing is done, user can start reconstruction. (f) The final high-resolution image is shown in the application and automatically saved to the data storage.

5.3.3 Motion tracing and image reconstruction

The algorithm of image reconstruction is similar to our previous chip-scale microscopy demonstrations. The raw sequence represents spatially undersampled images of the original image with each frame translated by known sub-pixel shifts. Then, the algorithm re-arranges the low resolution sequence into a single high resolution matrix, according to the sub-pixel shifts of the object in each frame. Previously, we have applied such algorithm in various chip-scale microscopy techniques where low resolution images were sub-pixel shifted via microfluidic scanning of sample, inherent motion of the sample, or the sweeping the incident angle of illumination. In the case of sweeping light source, the shadow of the sample on the image sensor plane translates with a known amount of shift for each illumination angle, which then can be processed with pixel super-resolution reconstruction. In this work, we rely on user's hand motion to tilt the device (both sample and the

detector) around the light source to capture multiple low resolution shadow images with sub-pixel shifts.

Since the image reconstruction relies on the knowledge of the sub-pixel shifts between each frames, it is crucial to precisely measure the angle of incidence of the illumination in each frame. To calculate the illumination angle of the user's manual tilting, we traced the shadow images of a known reference target that is placed above the sensor. In shadow imaging, displacement of the shadow varies linearly with the distance between the sample and the object. The actual sample is usually located within a few micrometers range from the sensor surface (depending on the size of the sample), thus the sub-pixel shifts of the sample shadow can be scaled from the shift of the reference shadow. When the reference object is placed at a large distance away from the sensor, the reference shadow moves in large displacement and the accuracy of the measurement increases. However, if too far, reference shadow becomes blurry due to diffraction and the tracking of the shadow may fail in the image processing step due to low contrast of the target shadow images. For the reference target, we placed a piece of 200 μm -thick transparent film with a cross-pattern (200 $\mu\text{m} \times 200 \mu\text{m}$) printed on one side. The film is placed such that the printed target pattern faces towards the illumination (Figure 5 - 1c).

Figure 5 - 5 shows raw images and improved high resolution images of 2.5 μm microspheres imaged with a 1.4- μm -pixel sensor. Note that the bright center of each microsphere are resolved in the improved images as oppose to the low resolution images. We used 100 images to perform 8×8 enhancement by rounding the sub-pixel shifts to integer multiples of 1/8th of a low resolution pixel.

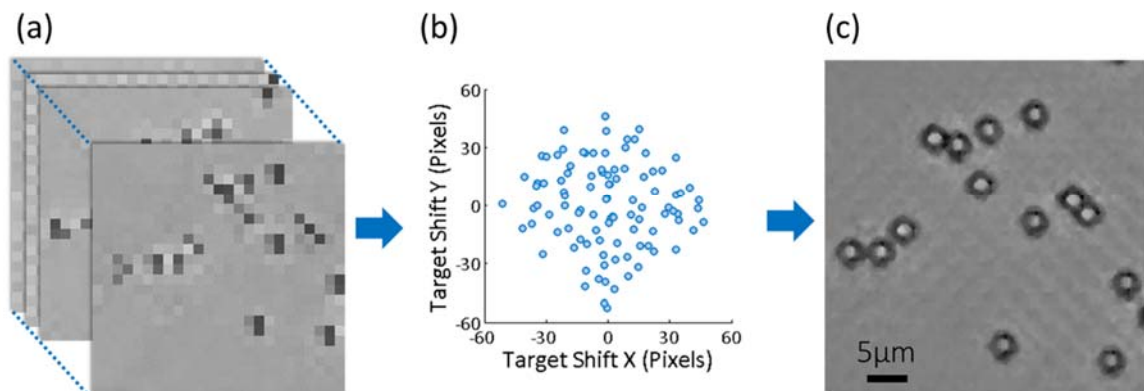


Figure 5 - 5. Raw and reconstructed images of 2.5 μm microspheres. (a) 100 frames of low resolution images were taken while we manually tilt the device. (b) The tilt angle for each image is measured by the shift of target object. (c) Reconstructed images show bright centers of the microspheres.

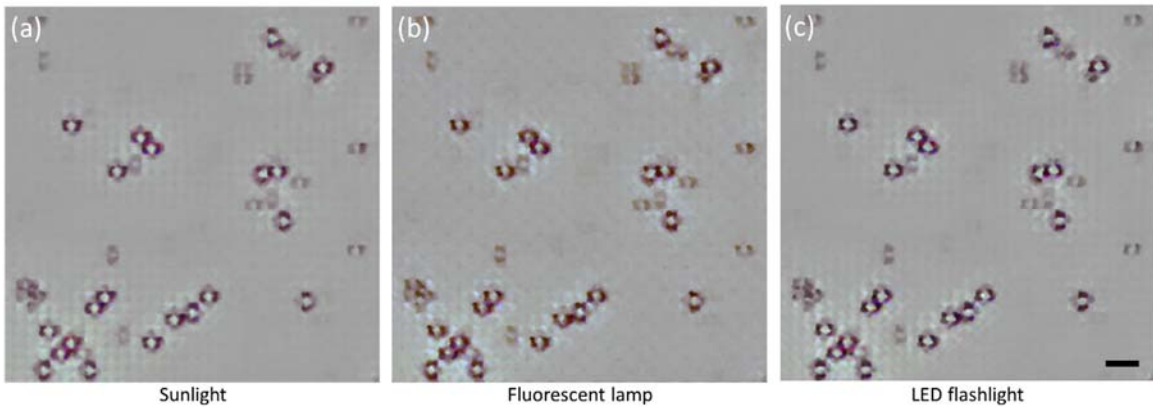


Figure 5 - 6. Microsphere ($2.5\ \mu\text{m}$ and $1.75\ \mu\text{m}$) images taken under various illumination sources. Under (a) LED flashlight in a smartphone, (b) Fluorescent light bulb (compact type, 15W) and (c) sunlight (clear sky, 2pm). For all experiments, we placed an IR filter and a ND filter (2OD) above the image sensor. For (a) and (b), images were taken at 30 cm away from the light source.

In order to remove motion-dependency in the image quality (Figure 5 - 7), the user is advised to tilt the camera around all four directions (up, down, left and right) within the boundary displayed in overlay with the camera. The application calculates the tilt in real-time as the user moves the hand around, plots the location in the screen to inform the user at which angle the images were taken. With the real-time processing, we can also reject images that are not suitable, for example, when an image is taken outside of the suggested boundary of illumination angle and when an image was previously taken at the same angle. The camera runs until it takes enough number of pictures. Typically, we used 100 frames for $8\times$ enhancement at the frame rate of 3 frames/sec for data transfer and target tracing, resulting in ~ 40 seconds of total image acquisition time. The frame rate is variant on the hardware data transfer rate and the image size.

The real-time target tracing was performed with OpenCV-based image processing algorithm[18]. The target object tracking process is as follows; from a captured image, we first converted the region containing the target shadow into HSB space. We then thresholded the HSB image into a binary image based on hue and saturation values to highlight the dark region (reference target's shadow) in the image. After removing the unwanted noises in the binary image, we computed the center of mass of the image to find the center position of the target shadow. We dump the images where target tracing was unsuccessful or the tilt angle was out of suggested range. Otherwise, the image and the measured target location is saved in the memory for reconstruction. Upon reconstruction, the translation of the target shadow is scaled to the expected shadow shift of the

sample on the image sensor surface. This scale factor, which denotes the height of the in-focus plane, is taken as user input upon reconstruction.

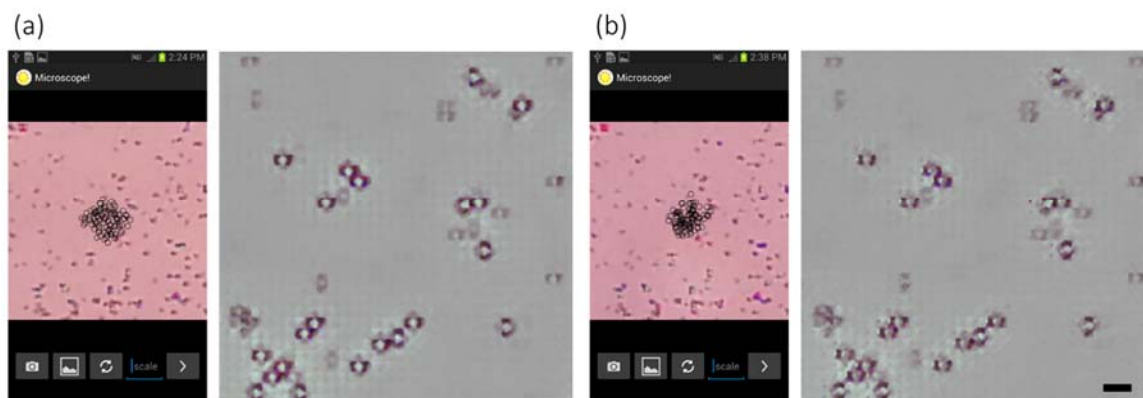


Figure 5 - 7. Microsphere images taken under different scanning motion. (a) Careful x, y scanning by monitoring the target tracing results, and (b) Random scanning by continuously tilting the device without target tracing. Insets show the tracing results. Both images were taken under sunlight illumination. Scale bar indicates 5 μm .

5.4 Portable imaging with smartphone microscope

Figure 5 - 8 shows blood smear images taken with our Samsung Galaxy S4 prototype. We used 100 images with the enhancement factor of 8. The boundaries of each red blood cell is clearly resolved in the reconstructed image. The blood smear is stained with Wright-Giemsa stain by dipping the entire image sensor module in methanol and Wright-Giemsa staining solutions according to the standard blood smear staining procedure. We imaged the same sample under different illumination sources (Figure 5 - 9). The quality of these images are similar between illuminations, except that the color contrast is higher in the images with an LED flashlight and a fluorescent lamp since the illumination spectra better matches the absorption spectra of methylene blue and eosin in Wright-Giemsa stain.

We investigated the resolution limit of our device by imaging 500-nm microspheres. We placed the microspheres on the surface of the 1.12- μm -pixel image sensors (Galaxy S4) and captured 200 images for reconstruction with the enhancement factor of 13 and 8. In both cases, the centers of the microsphere were resolved, and the diameter of the microspheres measured 580 nm and 590 nm, respectively (Figure 5 - 10). However, the images were inverted - the rim of the microsphere appears brighter than the center. We believe that this is caused by the microlens array on top of the image sensor pixels; the raw images taken at large angle of illumination, the microspheres appear brighter than the background. Previously, we have shown that the bright centers of 500-nm microspheres can

be resolved with 2.2- μm -pixel sensors without microlens array. We did not observe this effect with the microspheres that are larger than the microlens. Assuming that our optical resolution limit is 500 nm, reconstruction with 8 \times enhancement is sufficient because it is above the Nyquist limit of the high-resolution images (200-nm per pixel).

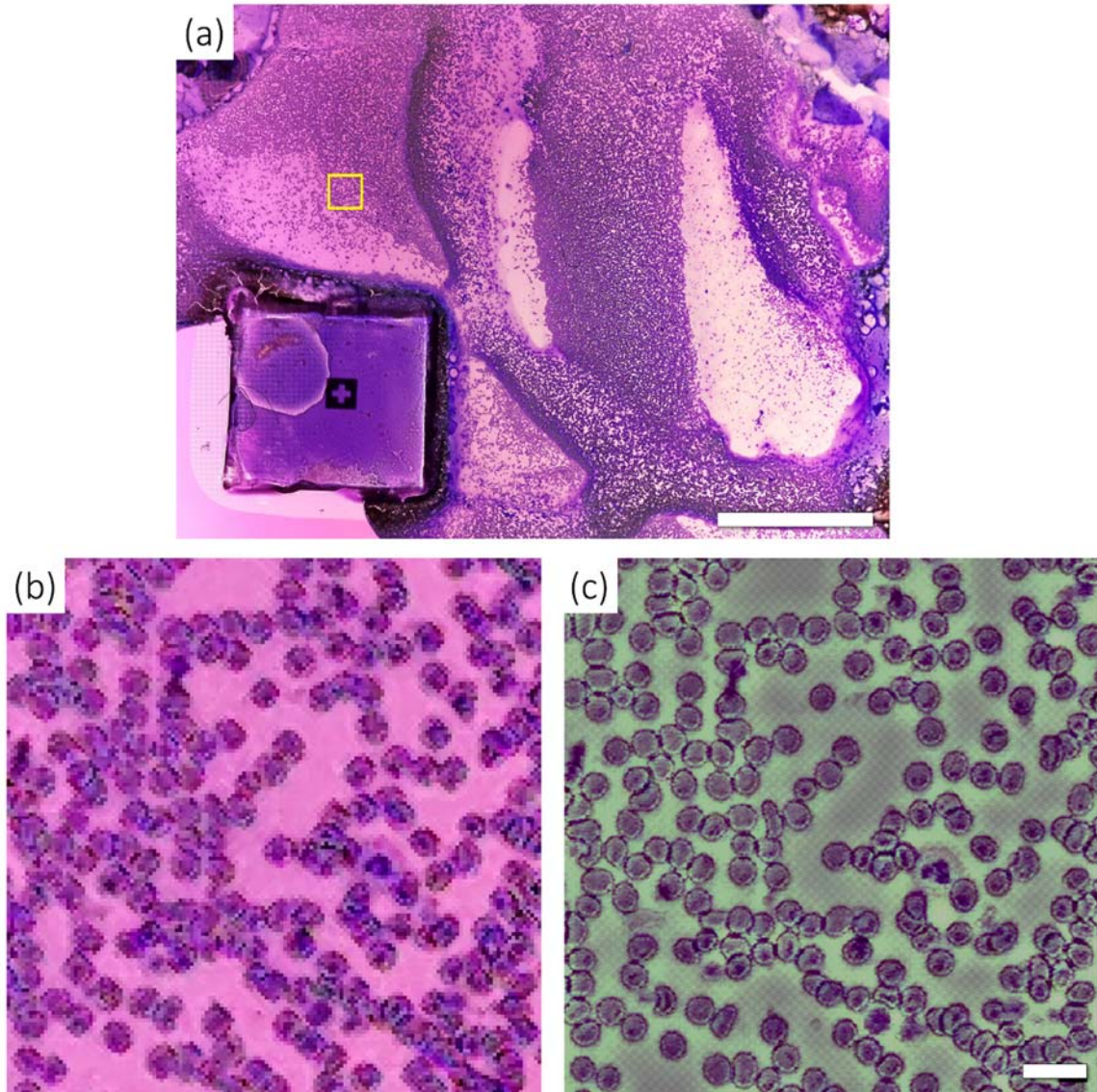


Figure 5 - 8. Wright-Giemsa stained blood smear. (a) A full FOV image of a blood smear made on the image sensor. Image sensor measures 4.5 mm \times 3.6 mm and the scale bar indicates 1 mm. (b) Raw and (c) reconstructed high resolution image of the region highlighted in (a). Images are reconstructed in the custom-built application. Scale bar indicates 20 μm .

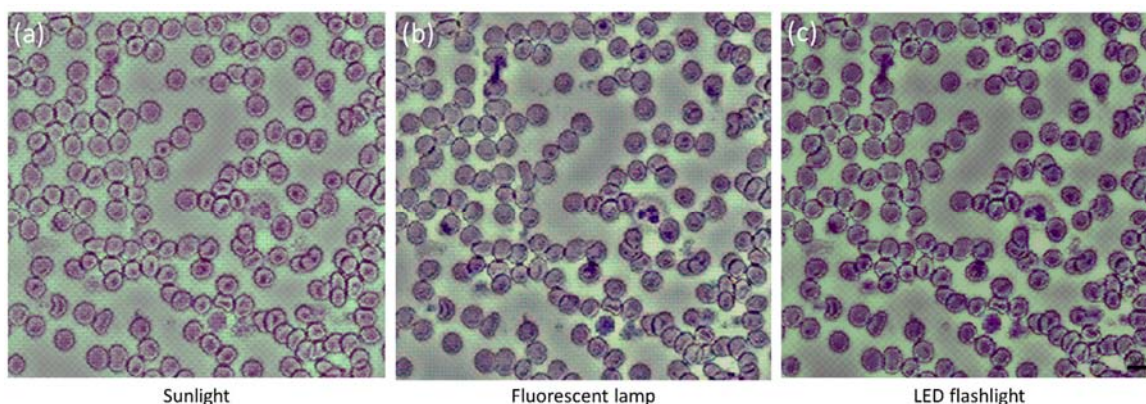


Figure 5 - 9. Blood smear images taken under various illumination sources. Under (a) sunlight (clear sky, 2pm), (b) Fluorescent light bulb (Spiral type, 15W) and (c) LED flashlight in a smartphone. For all experiments, we placed an IR filter and a ND filter (2OD) above the image sensor. For (b) and (c), images were taken at 30cm away from the light source.

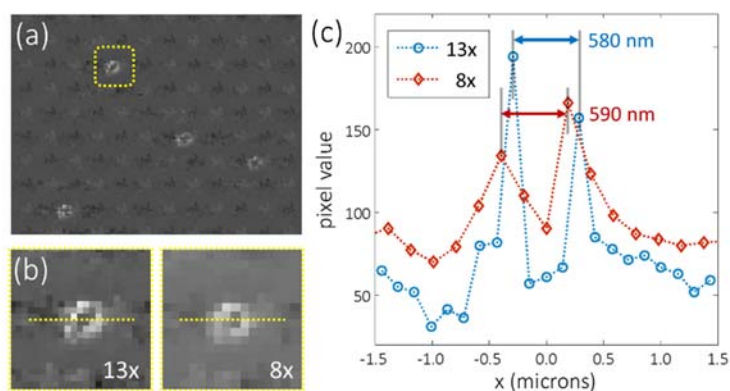


Figure 5 - 10. (a) Images captured with 500-nm polystyrene microspheres on the image sensor. We used 1.12- μm pixel sensors (effective low-resolution pixel size of 1.58 μm) (b) Magnified images of the microsphere marked in (a). We used 13x and 8x enhancement for high resolution reconstruction. One pixel in each image measures 120 and 200 nm, respectively. (c) Line trace of a microsphere images with 13x and 8x enhancement. In both cases, the center of the microsphere is resolved.

For portable imaging applications, we used our smartphone microscope to image fresh water sample taken from a koi pond on Caltech campus. We took the sample directly from the pond, dispensed 20 μL over the image sensor and let the particles settle for a few minutes before imaging. The images show various types of green algae in the pond water (Figure 5 - 11). We compared the images with the conventional microscope images of the same sample (20 \times objective lens, 0.4 Numerical Aperture). Various species of *Scenedesmus* (typically *Scenedesmus quadricauda* and *Scenedesmus acuminatus*), which is one of the most common freshwater genera of green algae, are found in the images[19]. In the reconstructed images, the grid-type artifacts can be seen in thick

samples. This results from the shadows of the parts of the sample in different height planes moving at different sub-pixel shifts under different illumination angle, which become out-of-focus upon reconstruction. These artifacts can further be suppressed by filtering the images to remove specific spatial frequency components.

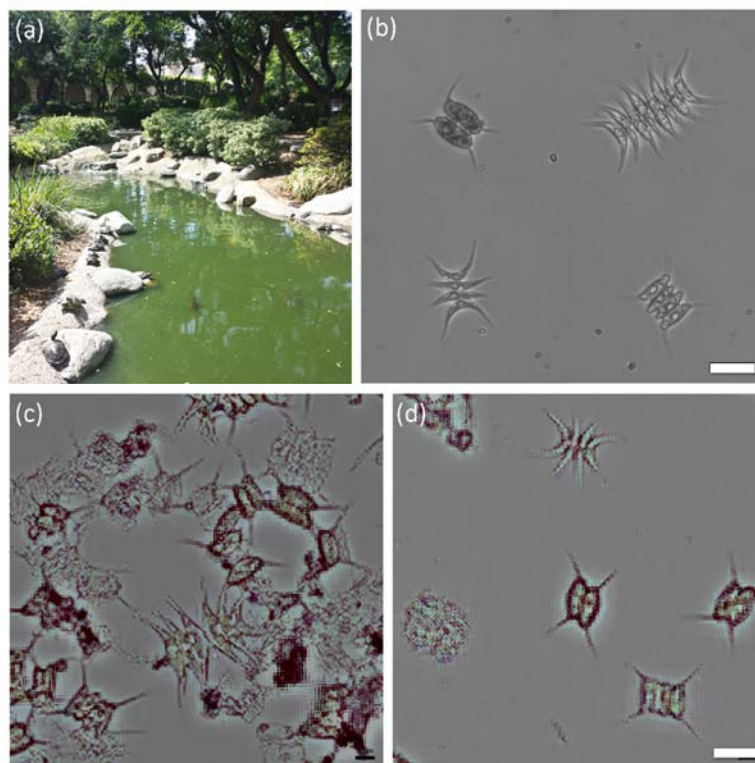


Figure 5 - 11. Portable microscopy of fresh-water microorganisms for water quality monitoring. (a) We took the fresh-water sample directly from a koi pond. 20- μ L of sample was dispensed on the image sensor and the particles were let settle down for few minutes before image acquisition. (b) Conventional microscope images of same sample taken with 20 \times (0.4 Numerical Aperture) objective lens. (c-d) Reconstructed images of green algae found in the pond. The green algae found in the sample are different species of *Scenedesmus*, a genus of *Chlorophyceae*. All scale bars indicate 20 μ m.

5.5 Discussions

We believe that the beauty of this technique is its simplicity and robustness, such that anyone can easily build their own device with commercially available parts. This makes microscopy more available for scientific and environmental applications, as well as for education and hobbyists. As for low-cost diagnostics in the resource-limited environment, one can construct these microscopes at low-cost with recycled-smartphones and image sensor modules, which can be purchased at relatively lower cost. We have shown that our device can produce images that are suitable to distinguish different types of blood cells and even resolve sub-cellular structures. These results suggests that we

can construct a portable diagnostic device by simply modifying readily available components and perform imaging-based tests such as whole-blood cell counting and diagnosis and monitoring of blood-borne parasite infections, such as malaria and trypanosomiasis.

Furthermore, direct shadow imaging scheme allows for integration of complex microfluidic systems on the smartphone without having to construct add-on devices. Small microfluidic channels can be attached on top of the image sensor, or more complex microfluidic systems can be designed to incorporate the image sensor in the part of the system where optical detection is required. The unprocessed direct shadow images still provide decent resolution ($\sim 2 \mu\text{m}$) to image biological samples and/or microstructures.

We also envision that fluorescence imaging capabilities can be incorporated with the addition of a filter layer on the image sensor[20]. The ability to detect fluorescent stains and immunofluorescence can enhance the specificity of image-based diagnostic tests. In addition to imaging, detection of various immunoassays and genomic assays can be performed on-chip, providing an easier route for micro total-analysis-systems on a smartphone platform.

BIBLIOGRAPHY

1. Kilian, A.H.D., W.G. Metzger, E.J. Mutschelknauss, G. Kabagambe, P. Langi, R. Korte, and F. von Sonnenburg, *Reliability of malaria microscopy in epidemiological studies: results of quality control*. Tropical Medicine & International Health, 2000. **5**(1): p. 3-8.
2. Kirchhoff, L.V., J.R. Votava, D.E. Ochs, and D.R. Moser, *Comparison of PCR and microscopic methods for detecting Trypanosoma cruzi*. Journal of Clinical Microbiology, 1996. **34**(5): p. 1171-5.
3. Mabey, D., R.W. Peeling, A. Ustianowski, and M.D. Perkins, *Tropical infectious diseases: Diagnostics for the developing world*. Nat Rev Micro, 2004. **2**(3): p. 231-240.
4. Marshall, M.M., D. Naumovitz, Y. Ortega, and C.R. Sterling, *Waterborne protozoan pathogens*. Clinical Microbiology Reviews, 1997. **10**(1): p. 67-85.
5. Savioli, L., H. Smith, and A. Thompson, *Giardia and Cryptosporidium join the 'Neglected Diseases Initiative'*. Trends in Parasitology, 2006. **22**(5): p. 203-208.
6. Wongsrichanalai, C., M.J. Barcus, S. Muth, A. Sutamihardja, and W.H. Wernsdorfer, *A review of malaria diagnostic tools: microscopy and rapid diagnostic test (RDT)*. The American journal of tropical medicine and hygiene, 2007. **77**(6 Suppl): p. 119-127.
7. Payment, P., M. Waite, and A. Dufour, *Introducing parameters for the assessment of drinking water quality*. Assessing Microbial Safety of Drinking Water, 2003: p. 47.
8. Gilstrap, D., *Ericsson Mobility Report*. 2013: November 2013.
9. Bellina, L. and E. Missoni, *Mobile cell-phones (M-phones) in telemicroscopy: increasing connectivity of isolated laboratories*. Diagnostic Pathology, 2009. **4**(1): p. 19.
10. Granot, Y., A. Ivorra, and B. Rubinsky, *A New Concept for Medical Imaging Centered on Cellular Phone Technology*. PLoS ONE, 2008. **3**(4): p. e2075.
11. JeongGil, K., L. Chenyang, M.B. Srivastava, J.A. Stankovic, A. Terzis, and M. Welsh, *Wireless Sensor Networks for Healthcare*. Proceedings of the IEEE, 2010. **98**(11): p. 1947-1960.
12. Breslauer, D.N., R.N. Maamari, N.A. Switz, W.A. Lam, and D.A. Fletcher, *Mobile Phone Based Clinical Microscopy for Global Health Applications*. PLoS ONE, 2009. **4**(7): p. e6320.
13. Tseng, D., O. Mudanyali, C. Oztoprak, S.O. Isikman, I. Sencan, O. Yaglidere, and A. Ozcan, *Lensfree microscopy on a cellphone*. Lab on a Chip, 2010. **10**(14): p. 1787-1792.
14. Navruz, I., A.F. Coskun, J. Wong, S. Mohammad, D. Tseng, R. Nagi, S. Phillips, and A. Ozcan, *Smart-phone based computational microscopy using multi-frame contact imaging on a fiber-optic array*. Lab on a Chip, 2013. **13**(20): p. 4015-4023.
15. Zheng, G., S.A. Lee, S. Yang, and C. Yang, *Sub-pixel resolving optofluidic microscope for on-chip cell imaging*. Lab on a Chip, 2010. **10**(22): p. 3125-3129.
16. Lee, S.A., G. Zheng, N. Mukherjee, and C. Yang, *On-chip continuous monitoring of motile microorganisms on an ePetri platform*. Lab on a Chip, 2012. **12**(13): p. 2385-2390.
17. Zheng, G., S.A. Lee, Y. Antebi, M.B. Elowitz, and C. Yang, *The ePetri dish, an on-chip cell imaging platform based on sub-pixel perspective sweeping microscopy (SPSM)*. Proceedings of the National Academy of Sciences, 2011. **108**(41): p. 16889-16894.
18. *OpenCV4Android SDK*. Available from: http://docs.opencv.org/doc/tutorials/introduction/android_binary_package/O4A_SDK.html.
19. Guiry, M. and G. Guiry, *AlgaeBase. World-wide electronic publication, National University of Ireland, Galway*. 2011.

20. Lee, S.A., X. Ou, J.E. Lee, and C. Yang, *Chip-scale fluorescence microscope based on a silo-filter complementary metal-oxide semiconductor image sensor*. Optics Letters, 2013. **38**(11): p. 1817-1819.

FLUORESCENCE CHIP-SCALE MICROSCOPY WITH SILO-FILTER IMAGE SENSOR

6.1 Background

Fluorescence is a molecular phenomenon where the substance absorbs light or other electromagnetic radiation and emits light of other wavelength. It occurs from instantaneous ($\sim 10^{-8}$ s) relaxation of excited electrons of a molecule and the energy losses between excitation and emission results in the Stokes shift of emission towards longer wavelengths of light. With the adequate optical systems, this shift in wavelength allow for detection of fluorescent molecules within the sample of interest. For biological imaging, many fluorescent dyes have been developed to label specific parts of a specimen, by conjugating to other organically active substances such as proteins and nucleic acids. These fluorophores are available with various excitation and emission spectra for multiplexed detection.

Fluorescence microscopy has now become a powerful tool for visualizing inter- and intra-cellular dynamics in biological processes. With a wide variety of probes available, fluorescence imaging provides target-specific, high-contrast images suitable for quantitative and automated data analysis. As the simplest form, epifluorescence microscopes have long been standard equipment in biological imaging. However, lens-based epifluorescence microscopes still suffer from their inherent disadvantages of high cost, large size, and limited field of view (FOV) and fluorescence collection efficiency. A fluorescence imaging system that overcomes these drawbacks can greatly improve the efficiency and the cost of image-based analyzes, such as high content screening [1], lineage tracing [2] and migration assays [3].

6.1.1 Optical requirements for fluorescence detection

Fluorochromes typically used for biological imaging has well-defined excitation and emission spectrum within UV-visual-IR regions. Figure 6 - 1 shows an absorption and emission spectra of a typical fluorochrome. The intensity of fluorescent signal is very weak compared to the intensity of light required to excite the fluorophores and it is dependent on several factors[1, 2]. Some of these factors are the inherent chemical characteristics of the fluorescent dye itself; the absorptivity of excitation light (extinction coefficient) and the ratio between the emitted and the absorbed photons (Quantum yield) typically determine the brightness of the fluorochrome. The concentration of

fluorophores in the specimen and the thickness of the specimen also determines the intensity of fluorescence emission. Lastly, the fluorescence collection efficiency of the microscope determines the amount of fluorescent signal detected by the optical system and is dependent on the performance of optical components and the NA of the objective lens. Considering these factors, the intensity of collected fluorescent signal can be expressed as below;

$$I_{fl} = \eta I_{em} = \eta Q I_{ab} = \eta Q I_{ext} (1 - e^{-\epsilon c l}) \approx I_{ext} \eta Q \epsilon c l \quad (6,1)$$

I_{em} , I_{ab} and I_{ext} denotes intensities of fluorescence emission, absorption of excitation light and excitation light incident on the sample. The quantum yield, Q , denotes how much of the absorbed light will be converted into fluorescence emission and typically ranges between 0.1 to close to unity. The extinction coefficient, ϵ , for fluorochromes typically range between $1e4 \sim 1e5 \text{ M}^{-1}\text{cm}^{-1}$. However, for biological imaging, the amount of light absorption is limited by the amount of allowed fluorophores in the sample. The size of the sample, l , is typically in the order of micrometers and the concentration of fluorophores, c , range between nanomolar to micromolar concentration. For an epifluorescence microscope with minimum loss, the fluorescence collection efficiency, η , is the volume fraction of the cone of rays corresponding to the acceptance angle, θ , of an objective lens out of the anisotropic fluorescence emission.

$$\eta = \frac{1 - \cos \theta}{2} = \frac{1 - \sqrt{1 - \left(\frac{NA}{n}\right)^2}}{2} \quad (6,2)$$

For low-magnification objective lenses of NA = 0.3, 0.5 and 0.75, the corresponding collection efficiency will be $\eta = 2, 7$ and 17%. The maximum achievable collection efficiency is around 30%, with a 1.4NA oil immersion objective lens. This raises a crucial limitation of objective-lens based epifluorescent microscopes – large FOV imaging with a low NA lens is hindered by the loss of fluorescence signal due to the low collection efficiency. Dim fluorescent samples require high NA objective lenses, which in turn limits the FOV.

Considering these factors, the ratio between the intensity of fluorescence signal and excitation light is in the order of 10^{-4} (highly fluorescent) to 10^{-9} (weak fluorescence)[2]. The imaging system's ability to attenuate the excitation light and detect the fluorescence signal without loss determines the quality (contrast) of the fluorescence images.

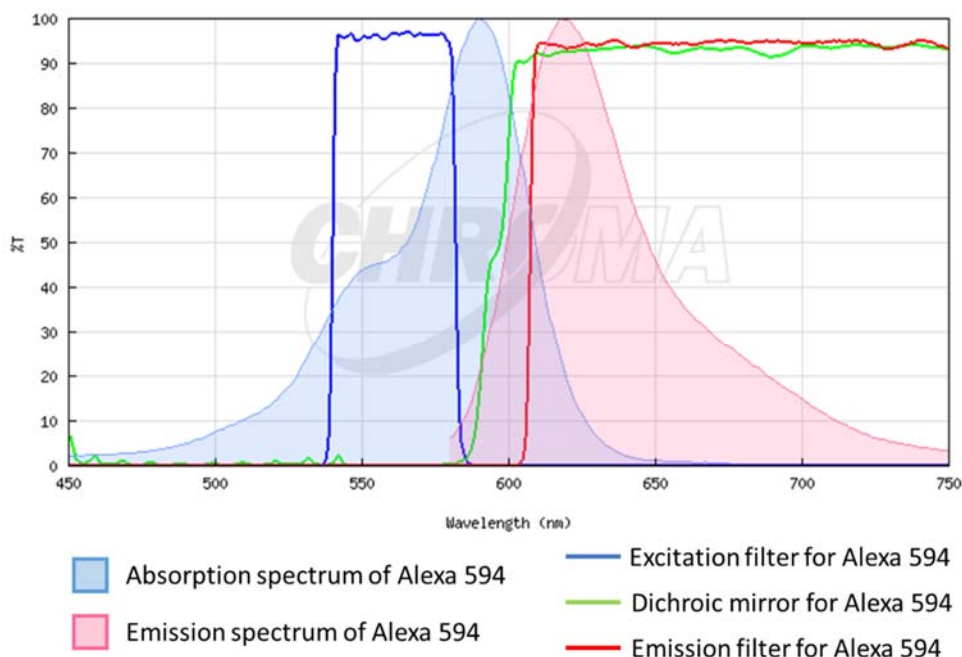


Figure 6 - 1. Fluorescence absorption and emission spectrum of Alexa 594 fluorochrome and the transmission characteristics of a commercial filter set typically used for detection of red fluorochromes such as Alexa 594, Texas red and mCherry. This plot is obtained from Chroma spectra viewer (<http://www.chroma.com/spectra-viewer?fluorochromes=49&set=757&showDetails=1>)

6.1.2 Epifluorescence microscopy

Conventional epifluorescence microscopes employ a set of optical filters to illuminate the sample with the wavelengths of light for fluorescence excitation and selectively detect the emission bands of the target fluorophores. Figure 6 - 2 illustrates a schematic of a wide-field epifluorescence microscope. Fluorescence filter cube is composed of a dichroic beam splitter, which reflects the excitation wavelengths and transmits the emission band, and two filters that each transmit excitation and emission wavelengths to further reduce backgrounds in the resulting images. These set of filters are designed for specific fluorochromes and sometimes for detection of multiple fluorochromes and available for the user to choose (Figure 6 - 1). The light sources for fluorescence microscopes can be broadband (Mercury-arc lamps and Xenon-arc lamps) or monochromatic (LEDs and lasers), but laser sources are not preferred in wide-field epifluorescence microscopes due to their coherent nature.

There are two major types of optical filters used for epifluorescence microscopes; absorptive filters and thin-film interference filters. Absorptive filters attenuate light by absorption and thus the performance is dependent on the thickness of the colored glass or amount of the polymer dye. Although cheaper and less dependent on the incidence angle, absorptive filters have limited

wavelength selectivity and sometimes lower transmittance at the pass band. Thin-film coatings can be specifically designed for desired wavelengths with sharp spectral slopes, thus being more preferred in modern fluorescence microscopes. However, interference-based attenuation requires highly precise design and manufacturing, which makes it expensive and sensitive to angle of incidence. In an epifluorescence microscope, the attenuation of excitation band is determined by the performance of the dichroic mirror and the emission filter, and typical thin-film coating filters provide ~ 3 OD and ~ 7 OD, respectively, and thus more than 10 ODs to provide enough SNR in the resulting images.

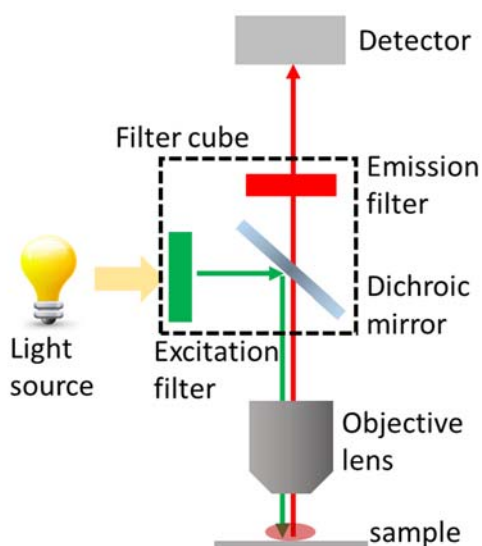


Figure 6 - 2. Schematics of a wide-field epifluorescence microscope equipped with a fluorescent filter cube.

6.1.2 Fluorescence on-chip microscopy

In chip-scale fluorescence imaging, the emission filter is required between the sample and the detector which selectively transmits the fluorescence signal and attenuates excitation light. Implementation of fluorescence capability in chip-scale microscopes has been challenging due to the incoherent nature of fluorescence emission and the need for high-performance filters. Despite the high performance, thin-film coatings are too costly for chip-scale microscope platforms, where the image sensors are often disposed after a single use or prone to damages from being in direct contact with the sample. Absorptive color dyes make good candidate materials for an emission filter thanks to their low cost and ease of fabrication. However, the limited absorptive property of dyes necessitates a substantially thick filter layer, which imposes a separation between the sample and the detector. As

a result, the fluorescence emission would spread over multiple pixels and degrade the imaging resolution. Previous works have used a fiber guide plate to confine the fluorescence collection angle, but the achieved resolution of approximately 100 μm [based on the point spread function (PSF)] is restrictive for a broad range of bio-imaging application where higher resolution is strongly desired [3, 4].

One previous method to improve resolution in chip-scale fluorescence imaging is by using a structured illumination. Since the fluorescence emission only comes from the part of the sample that is illuminated with the excitation light, one can create tight focus spots of excitation beam to spatially limit the sources of fluorescence signal and scan the sample or the focus array to perform wide-field imaging. Other than the illumination design, it is still in line with our lensless chip-scale microscope approaches where the sample is directly placed on top of the sensor that is coated with absorptive filter. First approach by Pang *et al.*[5] have combined the concept of optofluidic microscope and diffractive optical elements (Fresnel zone-plates) to perform fluorescence imaging on chip. In fluorescence Talbot microscopy technique, Pang *et al.*[6] have created an array of focal spots on top of the filter-coated image sensors via the Talbot effect, and laterally scanned the focal spots over the sample by steering the beam with a micro-electro-mechanical (MEMS) mirror. In both systems, the resolution is determined by the size of the excitation focus, which was in the order of 1 μm . However, creating tight focal spots with diffractive optical elements and scanning of focus grid with the MEMS-mirror still requires high precision fabrication and alignment of optics, which may increase the cost and the size of chip-scale microscopes. One unique advantage of these systems is that the simple collection geometry (filter coated-image sensor) has decoupled the trade-off between the collection efficiency and the field-of-view in conventional lens-based systems. Large FOV fluorescence imaging with high resolution and high fluorescence collection efficiency of 12.5% have been achieved[6].

6.2 Fluorescence imaging with uniform filter coating

Figure 6 - 5 illustrates a fluorescence-capable ePetri system. The image sensor can be coated with absorptive dye, which passes fluorescence emission and blocks out excitation light. Bright-field imaging can still be done with SPSM illumination at the pass band of the filter layer, which yields shadow images of the sample. For the absorptive filter material, we chose Orasol® Red pigment, which has long-pass characteristics with cut-off at 590 nm. The optical density of the filter is determined by the concentration of the dye and the thickness of the filter layer. Ideally, we want to

maximize the dye concentration such that the filter layer can be as thin as possible. However, when the dye concentration is above the saturation concentration, the undissolved dye particles in the filter layer may cause significant loss of fluorescence signal. Through optimization of the filter material, we chose the Orasol red concentration of 1.7g/ml in KMPR1005 photoresist with 8 μm coating thickness. We use a high power green LED with a Texas Red excitation filter ($559 \pm 34 \text{ nm}$, $1 \text{ mW}/\text{cm}^2$) as the excitation source at an oblique angle of illumination. This allows for effective increase in the light path within the filter layer, resulting in higher rejection of the background signal. Note that fluorescence emission is omnidirectional and is not affected by the angle of illumination and the emission, given the same illumination intensity. The size of the entire system was $15 \times 15 \times 15 \text{ cm}^3$, which conveniently fits inside a commercial CO2 incubator for time-lapse imaging of live cells.

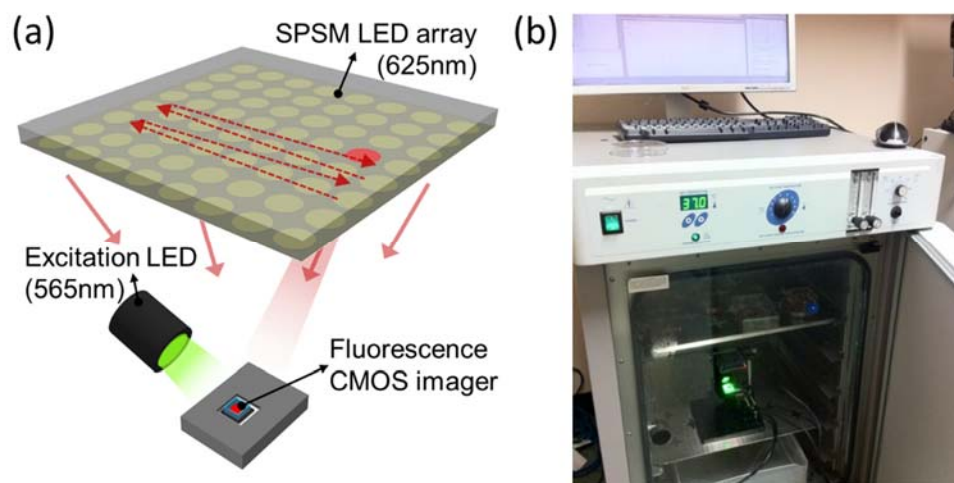


Figure 6 - 3. Bright-field and fluorescence imaging system using a filter coated CMOS imager. (a) Schematic diagram of the proposed imaging system consisting of a red LED array, high power LED for fluorescence excitation. (b) Compact chip-scale fluorescence microscope in action.

Adding fluorescence capability to SPSM imaging system can be useful for a wide range of applications. In Figure 6 - 4, we imaged clinical stool sample of *Giardia lamblia*-infected patient with a CMOS image sensor coated with Orasol red filter. The sample is stained with Alexa 594-labeled primary and secondary antibodies targeted for *Giardia lamblia*. In the bright field image, it is difficult to locate the giardia cysts among other particles in the stool sample. Also, in the fluorescence image, there is auto-fluorescence and non-specific binding of fluorescent antibodies to the debris, which is difficult to differentiate from the real signal. By matching the bright-field and fluorescence images together, we can easily identify giardia cysts by matching the fluorescence signal and the particle

morphology from the bright-field image. This added functionality allows for easier and more precise detection of parasite infection for diagnostic applications. However, the fluorescence resolution is very low ($\sim 20 \mu\text{m}$ from the PSF), which limits the application of this system for samples of smaller size and higher concentration. In addition, the resolution of bright-field imaging is also compromised low due to the increased distance between the sample and the detector.

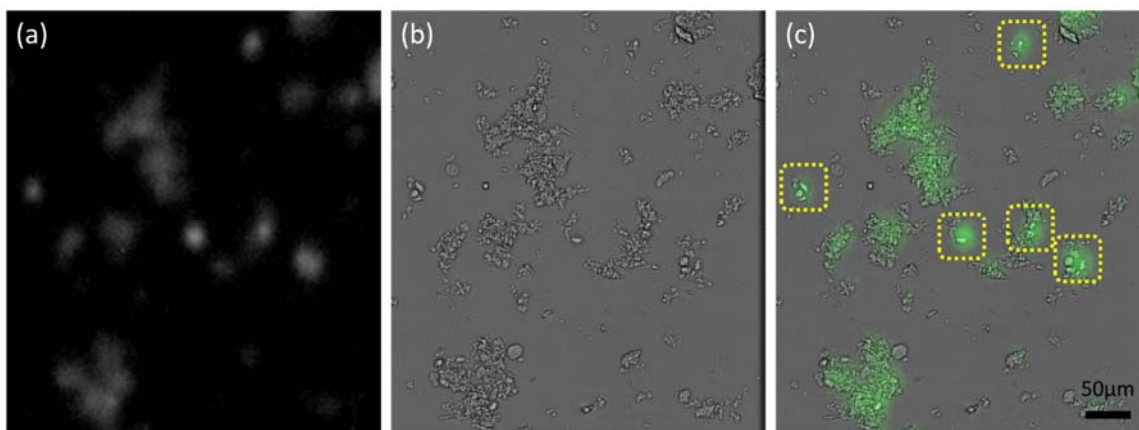


Figure 6 - 4. Fluorescence(a), bright-field(b) and overlay(c) images of stool smear sample of a *Giardia lamblia* infected patient. The sample is treated with immunofluorescence stain targeted for giardia. Marked cells in (c) indicate giardia cysts.

6.3 Fluorescence imaging with silo-filter sensors

A truly compact and low-cost fluorescence imaging solution with a resolution of approximately $10 \mu\text{m}$ (defined through the PSF) is sought, but has so far eluded practical implementation. To address this need, we developed a lensless fluorescence microscope using a CMOS image sensor with a silo-filter (SF) lattice structure. The pixel structure of a SF sensor is depicted in Figure 6 - 5 and Figure 6 - 6. The SF structure introduces pixelation in the filter layer with the metal grid blocking light crosstalk between pixels. The reflective metallic walls isolating each pixel can guide fluorescent light through the thick absorptive filter layer and onto the photodiode of a single pixel in the image sensor. As a result, fluorescence emission is confined to the pixel that is directly underneath the fluorophore with minimum loss of the signal and the plane of highest focal acuity is relayed from the sensor's surface to the top of the filter. We successfully fabricated such a structure on a working CMOS image sensor and obtained wide-field ($4.8 \times 4.4 \text{ mm}^2$) fluorescence imaging with $13\text{-}\mu\text{m}$ resolution. In combination with the SPSM method, we can perform transmission bright-field imaging and target-specific fluorescence imaging on a single ePetri platform.

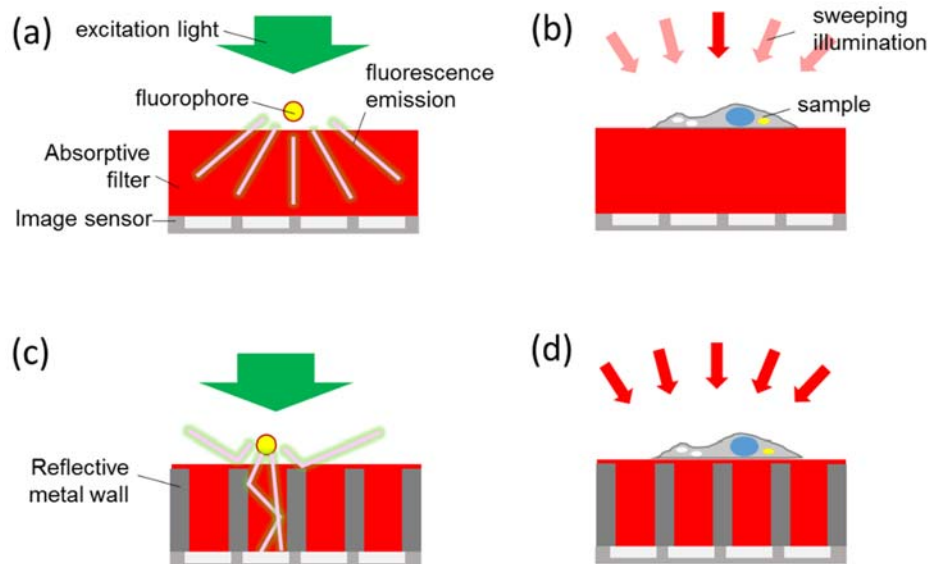


Figure 6 - 5. Fluorescence and bright field imaging configurations. (a-b) CMOS sensors coated with uniform filter layer. The fluorescence emission will blur out to several adjacent pixels. Bright-field shadow images will also deteriorate due to the increased distance between the pixel array and the sample. (c-d) Fluorescence and bright-field imaging with silo-filter sensors. Metal grid structure for pixelation in the filter layer guides fluorescence emission and relays focal plane through the filter layer.

6.3.1 Imaging system design

The imaging system consisted of a CMOS camera with an SF image sensor and the light sources for fluorescence excitation and SPSM bright-field imaging. The target sample, such as living cells, was placed on the surface of the SF sensor for imaging. Two modes of imaging are available: bright-field imaging by the SPSM method using 8×8 red light emitting diode (LED) array illumination (625 nm, $5 \mu\text{W}/\text{cm}^2$ per LED), and fluorescence imaging exploiting a high-power green LED with a Texas Red excitation filter (559 ± 34 nm, $1 \text{ mW}/\text{cm}^2$). For bright-field imaging, we scanned the 8×8 LED array to obtain 64 low-resolution images (15 ms exposure), which were combined into a single high-resolution image aided by pixel super-resolution reconstruction [7, 8]. Fluorescence images were taken with the excitation beam incident at a 60° angle (Figure 6 - 3). The integration time ranged from 100 to 450 ms, depending on the brightness of the sample. Total imaging time was approximately 40 seconds for a single set of bright-field and fluorescence imaging, which included software delays in device control and data transfer. We performed all cell culture experiments inside a commercial CO_2 incubator.

6.3.2 Fabrication of silo-filter structures

The fabrication process of silo-filter structure is shown in Figure 6 - 6. The prototype SF sensor was fabricated on a commercial CMOS image sensor ($5.2 \mu\text{m}$, 1024×1256 pixels). We first built high-aspect-ratio pillar arrays that are aligned to the sensor's pixel grid with SU-8 photoresist over an indium tin-oxide (ITO) coated image sensor. Using the ITO as the seed layer, we electroplated nickel via DC electroplating (condition) over the pillar array which works as the mold for metal deposition. During the electro plating process, metal wires and pins exposed on a sensor is sealed with acrylic nail polish. The nail polish is later removed by washing with acetone. Once the nickel grid was plated to the same height of the SU-8 layer, the pillar arrays were removed via oxygen plasma etching (150W, 20 min). After removing the mold, holes were filled with the Orasol® Red absorptive red pigment by spin coating. The top surface of the structure was coated with polystyrene passivation layer for cell culture [9, 10]. The Orasol® Red longpass filter has a 590-nm cut-off, appropriate for detecting red to far red dyes with green excitation, as was prepared with the recipe described in ref [11], with 1.7 g/ml concentration. The prototype had a SF-metal grid structure of $6 \mu\text{m}$ height and $4 \mu\text{m}$ opening with $1.2 \mu\text{m}$ metal walls, achieving a 59% filter fill factor (Figure 6 - 6). The effective imaging area of the prototype was $4.8 \times 4.4 \text{ mm}^2$.

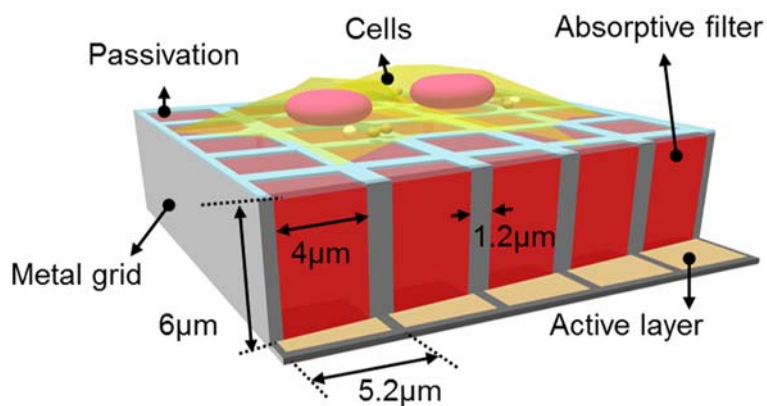


Figure 6 - 6. Schematic diagram of the SF structure for fluorescence chip-scale microscope.

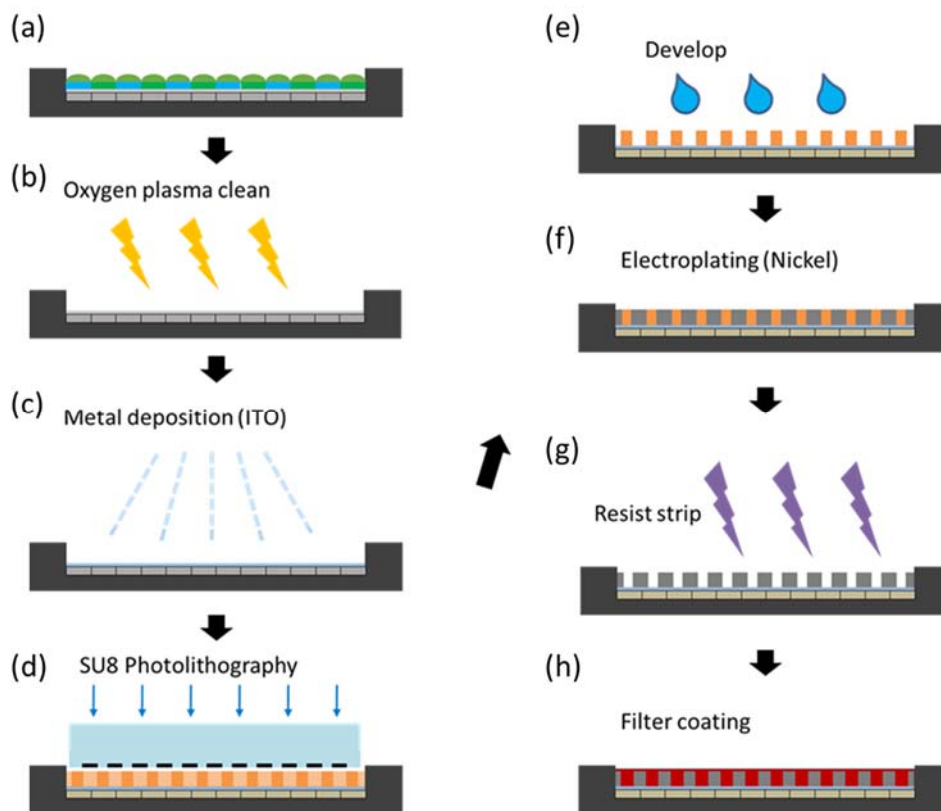


Figure 6 - 7. Fabrication process for silo-filter structures on a commercial CMOS image sensor.

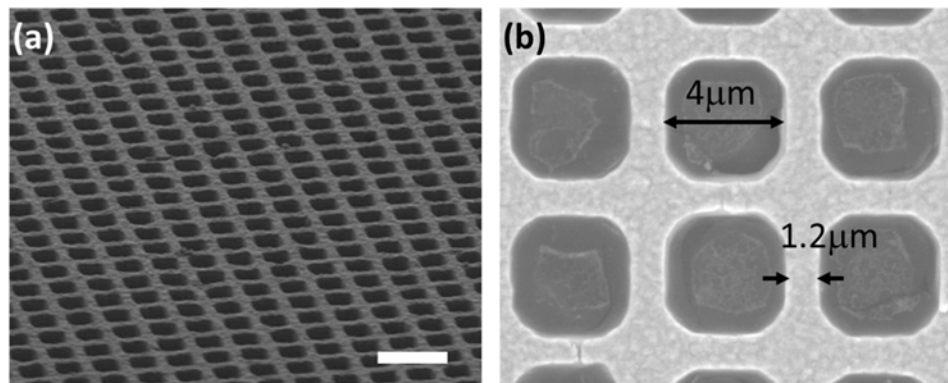


Figure 6 - 8. SEM micrograph of fabricated metal grid structure. Scale bar in (a) indicates 10 μm .

6.3.3 Performance and fluorescence collection efficiency

Figure 6 - 9 shows the angular sensitivity of the SF pixel geometry to plane illumination light field at 560 nm (green light, nominal excitation wavelength of Texas Red) and 625 nm (red light,

nominal emission wavelength of Texas Red). We measured light transmission at varying angles of incidence through a uniform filter (UF) and SF of the same height at both excitation and emission wavelengths. The metal grid structure provides enhanced rejection at large incident angle, which also improves background rejection for fluorescence. In the case of a UF, transmittance at a large incident angle is reduced due to the increased light traveling distance through the absorptive layer. With a SF, this loss is enhanced further due to scattering from the metal surface and the imperfect reflectance of the metal wall ($\sim 65\%$ at 590 nm [12]). As a result, we can achieve a comparable background rejection with a thinner filter in the SF structure than in the UF coating. At 60° incidence for excitation beam at 560 nm, a 6- μm SF filter provided 3.8 optical density units, sufficient for detection of fluorescence from bright samples.

The SF sensor sacrifices a large-angle component of the fluorescence emission due to the metal grid. The angular transmission data from Figure 6 - 9 at 625 nm provide a means for estimating that the fraction of isotropic fluorescence emission that can be effectively measured by the sensor is approximately 6%. This collection efficiency of the SF sensors can be improved by increasing the fill factor, optimizing the absorptive dye, and improving the surface uniformity and reflectance of the metal grid.

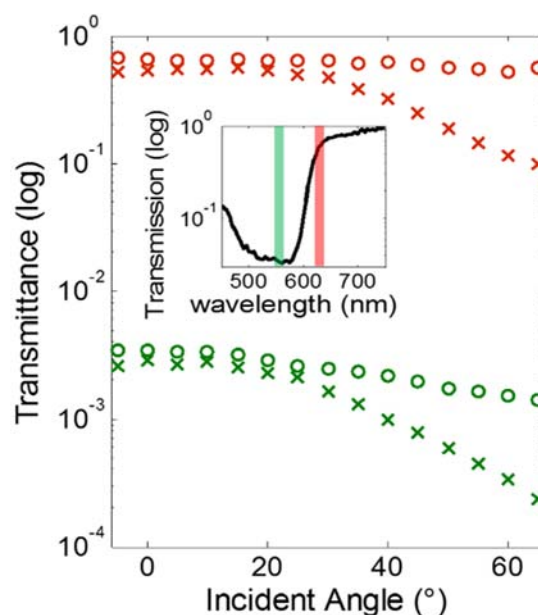


Figure 6 - 9. Transmission of light at varying incidence angles for uniform filter and silo-filter with 560 nm (green) and 625 nm (red) plane wave illumination. The transmission curve of the Orasol® Red filter (3 μm) is shown (inset).

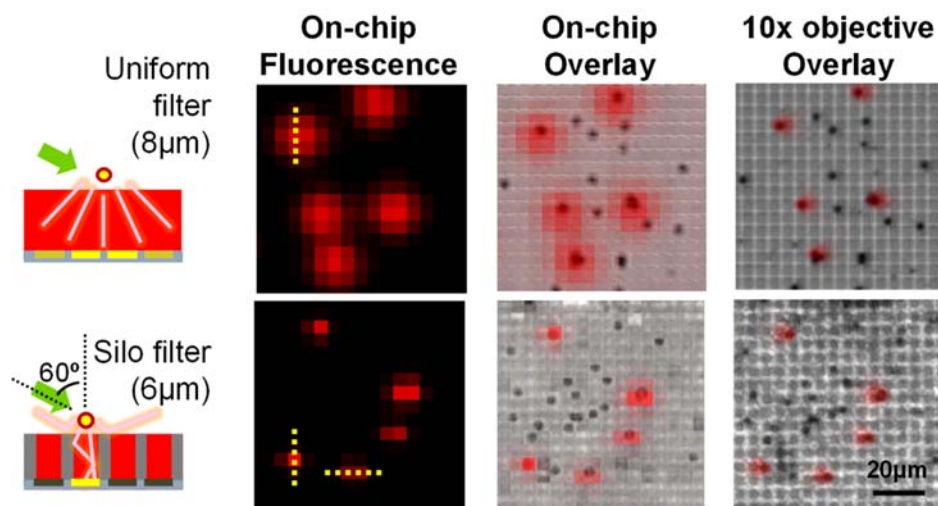


Figure 6 - 10. (b) Bright-field and fluorescent images of fluorescent ($2.5 \mu\text{m}$) and non-fluorescent ($2.0 \mu\text{m}$) microbeads in UF and SF sensors. Results are confirmed with $10\times$ objective microscope images.

We verified the fluorescence detection capability of our prototype by imaging fluorescent microspheres on the UF and SF sensors. A mixture of Texas Red fluorescent polystyrene microspheres ($2.5 \mu\text{m}$) and non-fluorescent microspheres ($2 \mu\text{m}$) were placed on the surface of the UF and SF sensors and imaged with the configuration illustrated in Figure 1a. We compared the $8\text{-}\mu\text{m}$ -thick UF sensor with the $6 \mu\text{m}$ SF sensor to match the background rejection in the resulting fluorescence images. Figure 6 - 10 shows the SPSM bright-field and fluorescence images obtained from the UF (top) and SF (bottom) sensors. $10\times$ objective lens microscope images of the same beads confirm that the UF and SF sensors can identify fluorescent and non-fluorescent beads. The obtained images demonstrate the improved resolution in the SF sensor images; the UF sensor images display large spots blurred out to several pixels, whereas the SF sensor has confined most of the fluorescence emission to a single pixel or two.

6.3.4. Resolution limit of Silo-filter structure

We quantified the resolution limit of the SF sensors with the PSF obtained with the fluorescent microbeads (Figure 6 - 11). Since the SF pixel is larger than the fluorescent bead, the location of the bead within the pixel affects the PSF. In the best case, a bead is placed at the center of an SF pixel and FWHM measures 1.2 pixels. In the worst case, a bead is placed on the metal grid between two pixels and the FWHM is increased to 2.2 pixels. Based on these measurements, we conclude that our prototype can resolve two beads that are placed 2.5 pixels ($13 \mu\text{m}$) apart, regardless of the position of the objects.

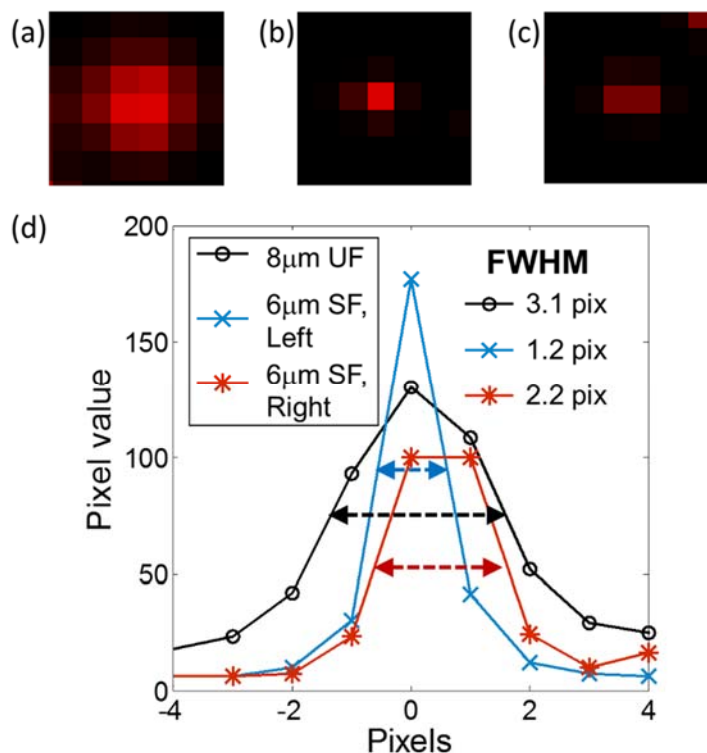


Figure 6 - 11. Resolution of silo-filter CMOS sensor. (a-c) Point spread functions of 2.5- μm fluorescent microbeads on 8- μm uniform filter coating (a), and 6- μm silo-filter coating. One pixel in all images are 5.2 μm . In (b) the microbead was located on top of the pixel and (c) in between two pixels. (d) Corresponding full-width-half at maximum values of point spread functions in (a-c).

6.4 Fluorescence live-cell imaging with Silo-filter image sensors

Figure 6 - 12 shows the images of mammalian cells cultured on an SF ePetri system. We used two types of fluorescently labeled cells: HEK 293 cells expressing mCherry red fluorescent protein (RFP), and MCF-7 cells stained with SYTO-64 red nucleic acid stain. Fluorescence images are taken with a 450 ms exposure. We corrected for the baseline noises resulting from the unblocked excitation light by subtracting the background image taken in the absence of cell samples. The images with the nucleic acid stain can distinguish the cell nucleus from the cytoplasm, whereas RFP-expressing cells fluoresce from all parts of the cells. Although current fluorescence resolution of our SF sensor is insufficient for identifying sub-cellular structures, image-based biological analysis at single-cell resolution may be applicable when combined with the higher-resolution bright-field images.

Finally, we performed long-term monitoring of cells cultured on an ePetri system using the SF sensors. HEK 293-mCherry cells were grown on a SF-ePetri system placed in the incubator and a set of bright-field and fluorescence images were obtained at 20 min intervals for 20 hours (Figure 6 - 14).

The time-sequence images indicate movement and growth of HEK 293 cells, which suggests that the fluorescent ePetri system can be adapted for monitoring dynamic processes in biological samples.

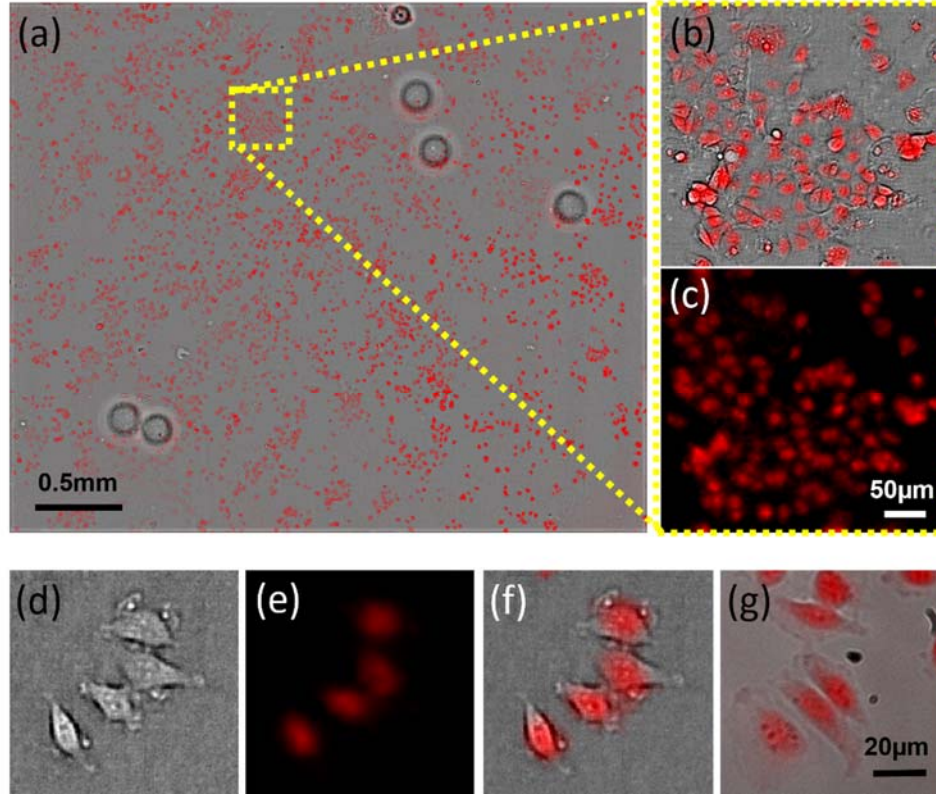


Figure 6 - 12. Bright-field and fluorescence images of living cells taken with a SF sensor chip. The sample is MCF-7 cells stained with SYTO-64 nucleic acid stain. (a) Full FOV bright-field and fluorescence overlay image. (b-c) Overlay and fluorescence images of region highlighted in (a). (d-f) SF sensor bright-field, fluorescence and overlay images. (g) 20× objective microscope image of the same type of cells on a conventional petri dish.

The quality of fluorescence images is assessed by computing the signal-to-noise ratio (SNR). Typically, images with more than 30 dB SNR are considered "good" for further analysis. The SNR in each image can be expressed as below:

$$\text{SNR} = 20\log_{10}\left(\frac{\mu_{sig} - \mu_{bg}}{\sigma_{bg}}\right) \quad (6,3)$$

where μ_{sig} and μ_{bg} are the mean signal and background intensities, respectively, and σ_{bg} is the standard deviation of the background [13]. Background pixels are identified by the inhomogeneity measurement method described [13]. The computed SNRs of the fluorescent images were 9.5 dB

(nucleic acid stain), 32 dB (RFP) and 35 dB (fluorescent beads). Images with nucleic acid stain resulted in relatively low SNR values due to the high background from unbound fluorophores.

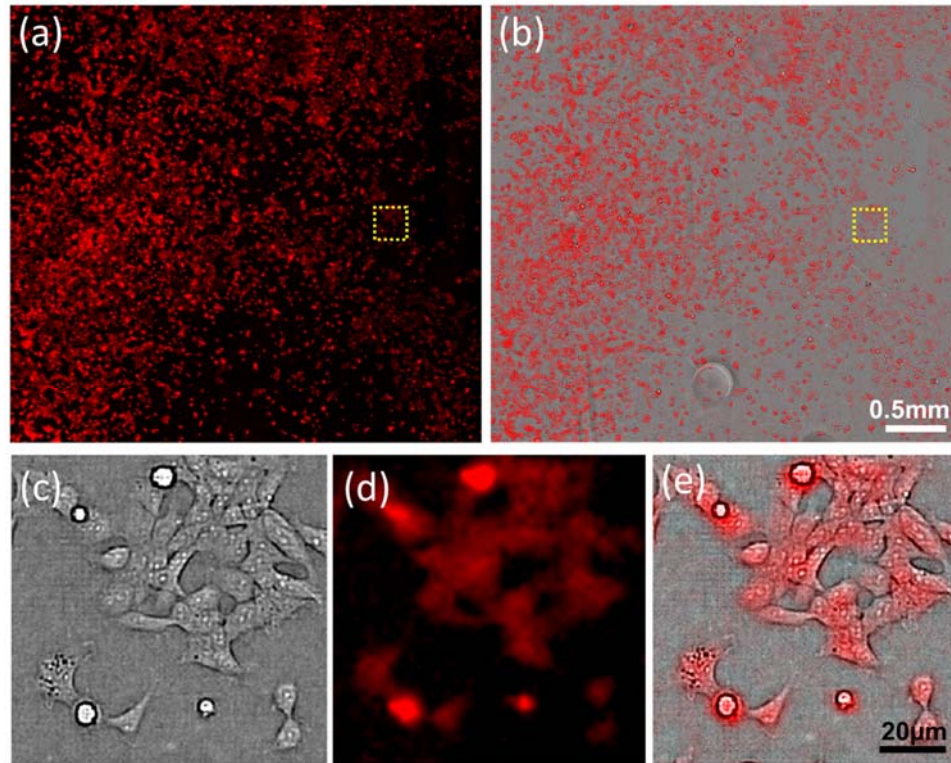


Figure 6 - 13. Bright-field and fluorescence images of mCherry-HEK293 cells taken with a SF sensor chip. (a-b) Full FOV fluorescence and overlay image. (c-e) Brightfield, fluorescence and overlay images of region highlighted in (a,b).

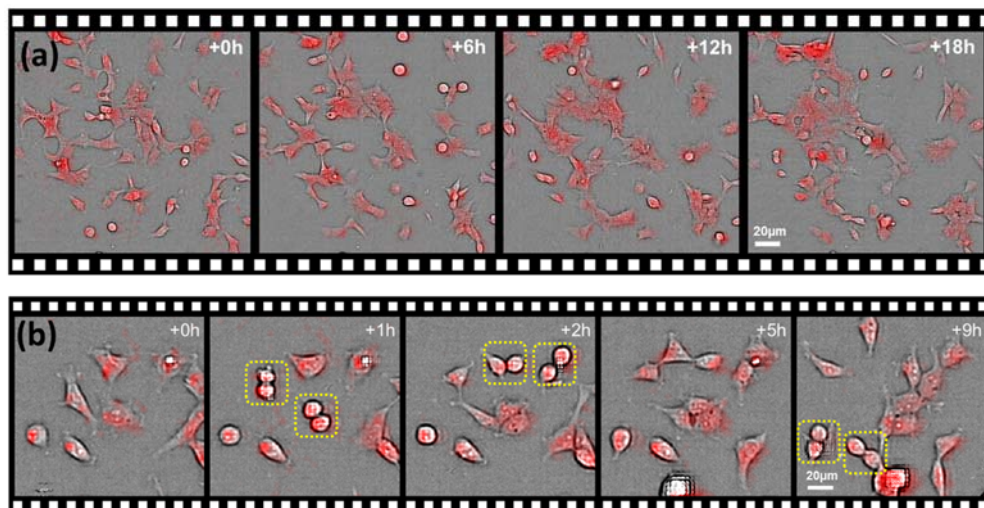


Figure 6 - 14. Time-lapse sequence showing migration and mitosis (b,boxed) of HEK 293-mCherry cells.

6.5 Discussions

Fluorescence imaging systems based on SF-CMOS sensors can be very compact, low-cost and robust, suitable for imaging needs for high-throughput biological analysis, portable microscopy and field-diagnostics. This system does not require any stringent characteristics on the optical components, such as coherency of the illumination and precise alignment. The illumination for both bright-field and fluorescence is based on incoherent light sources (LEDs), and the only design parameter for fluorescence excitation is the illumination angle and the intensity. Also, the fabrication of SF-CMOS sensors are based on standard LIGA (Lithography, Electroplating, and Molding) process, which can be easily incorporated into the standard production process for the CMOS image sensors. Although the prototype device was built on a relatively large pixel sensor (5.2 μm), we expect that the state-of-the-art CMOS process is capable of fabricating much finer structures on smaller pixel sensors ($< 2.2 \mu\text{m}$), with better surface-coverage and higher fill-factor. Multi-color fluorescence may be possible, if Bayer-pattern-like patterning of different absorptive filters can be achieved on the pixel level. Previously, Pang *et al.*[6] have successfully detected fluorescence emission from Alexa 488 and green fluorescent proteins using green-pigment based absorptive filter layer.

The performance of the SF-CMOS sensors can improve by further optimizing the structure. For example, higher fill-factor of the SF structure with increased reflectance of the metal surfaces can improve the collection efficiency of the fluorescence signal. Smaller pixels will yield higher spatial resolution of the resulting images (both fluorescence and bright-field images). However, SF structures on smaller pixel sensors may lead to degradation of fluorescence collection efficiency, due to the increased aspect ratio and decreased numerical aperture of the SF structure. Structured-illumination based fluorescence imaging[6] on SF-CMOS sensors can achieve higher resolution. For Talbot-grid based microscopy, higher density of illumination focal spot array can be used on SF sensors compared to UF sensors and the number of scanning required to image the full FOV can be significantly reduced, thus increasing the throughput of imaging.

BIBLIOGRAPHY

1. Lichtman, J.W. and J.-A. Conchello, *Fluorescence microscopy*. Nat Meth, 2005. **2**(12): p. 910-919.
2. Reichman, J., *Handbook of optical filters for fluorescence microscopy*. Chroma Technology Corporation, 2000.
3. Coskun, A.F., I. Sencan, T.-W. Su, and A. Ozcan, *Lensless wide-field fluorescent imaging on a chip using compressive decoding of sparse objects*. Opt. Express, 2010. **18**(10): p. 10510-10523.
4. Coskun, A.F., I. Sencan, T.-W. Su, and A. Ozcan, *Wide-field lensless fluorescent microscopy using a tapered fiber-optic faceplate on a chip*. Analyst, 2011. **136**(17): p. 3512-3518.
5. Pang, S., C. Han, L.M. Lee, and C. Yang, *Fluorescence microscopy imaging with a Fresnel zone plate array based optofluidic microscope*. Lab on a Chip, 2011. **11**(21): p. 3698-3702.
6. Pang, S., C. Han, M. Kato, P.W. Sternberg, and C. Yang, *Wide and scalable field-of-view Talbot-grid-based fluorescence microscopy*. Opt. Lett., 2012. **37**(23): p. 5018-5020.
7. Park, S.C., M.K. Park, and M.G. Kang, *Super-resolution image reconstruction: a technical overview*. Signal Processing Magazine, IEEE, 2003. **20**(3): p. 21-36.
8. Zheng, G., S.A. Lee, Y. Antebi, M.B. Elowitz, and C. Yang, *The ePetri dish, an on-chip cell imaging platform based on sub-pixel perspective sweeping microscopy (SPSM)*. Proc. Nat'l. Acad. Sci., 2011. **108**(41): p. 16889-16894.
9. Stange, T., R. Mathew, D.F. Evans, and W. Hendrickson, *Scanning tunneling microscopy and atomic force microscopy characterization of polystyrene spin-coated onto silicon surfaces*. Langmuir, 1992. **8**(3): p. 920-926.
10. Lock, E., S. Walton, and R. Fernsler, *Preparation of ultra thin polystyrene, polypropylene and polyethylene films on Si substrate using spin coating technology*. 2008, DTIC Document.
11. Richard, C., A. Renaudin, V. Aimez, and P.G. Charette, *An integrated hybrid interference and absorption filter for fluorescence detection in lab-on-a-chip devices*. Lab on a Chip, 2009. **9**(10): p. 1371-1376.
12. Robert, W., *The variation of the reflectivity of nickel with temperature*. Proc. Phys. Soc. , 1947. **59**(5): p. 781.
13. Paul, P., D. Kalamatianos, H. Duessmann, and H. Huber. *Automatic quality assessment for fluorescence microscopy images*. in *Proceedings of IEEE International Conference on BioInformatics and BioEngineering, (BIBE 2008)*.

SUMMARY

Several implementations of chip-scale microscopes have been covered in this thesis, with the aim of achieving compact and low-cost imaging for various biological applications. Bright-field chip-scale microscopes discussed in this thesis are based on pixel super-resolution reconstruction of direct shadow images, with different strategies for obtaining sub-pixel shifted images of the specimen placed on a CMOS image sensor. Fluorescence version of the chip-scale microscope have also been demonstrated, where silo-filter microstructures effectively guide the fluorescence emission to compensate for the resolution loss in the filter layer.

In Chapter 2, we proposed and demonstrated a new version of optofluidic microscope that utilizes the pixel super-resolution algorithm to capture and reconstruct high resolution images of biological samples in flow. The novel combination of the pixel super-resolution and optofluidic approach towards microscopy removes the need for bulky and expensive lenses, coherent illumination sources and precision microscanning mechanisms. SROFM system allows us to capture images of rotating samples in high resolution and, thereby, reveal three-dimensional sub-cellular structures from different perspectives. In addition, color imaging capabilities with switching illumination of RGB LEDs have been implemented, aiming to detect stained *P. falciparum* parasites within the red blood cells for potential applications in malaria diagnostics. We have achieved sub-micron optical resolution ($0.66\ \mu\text{m}$ with $2.2\text{-}\mu\text{m}$ sensor) compatible with conventional microscopy with $20\times$ objective lens (0.4NA).

In Chapter 3, we demonstrated the imaging of motile microorganisms by using the inherent motion of the cells for the pixel super-resolution reconstruction. The sub-pixel motion microscopy (SPMM) utilizes the swimming motion of *Euglena gracilis* to capture a sequence of shadow images with sub-pixel shifts. Using SPMM method, we achieve high resolution ($\sim 1\ \mu\text{m}$) imaging over $5.7\ \text{mm} \times 4.4\ \text{mm}$ area without using any optical elements. In this chapter, we also introduce the concept of ePetri, a self-imaging Petri dish for cultivation and biological analysis of live biological specimen on a chip-scale microscopy platform. We show long term culture of *Euglena gracilis* in a SPMM ePetri platform, and demonstrate image-based analysis for automatic cell counting, motion analysis, and shape analysis.

In Chapter 4, we have demonstrated on-chip imaging of waterborne protozoan parasite cysts with the sub-pixel sweeping illumination microscopy (SPSM). Lateral translation of the light source above the image sensor, easily achieved by using an LED matrix, causes sub-pixel shifting of the shadow images. In this scheme, static samples with high confluency can now be imaged for an ultra-wide FOV ($5.7 \text{ mm} \times 4.4 \text{ mm}$) and high imaging resolution ($< 1 \text{ }\mu\text{m}$) with color capability. We imaged three major types of water-borne parasite cysts, *Entamoeba*, *Giardia*, and *Cryptosporidium*, and showed the resulting images are suitable for both manual and automatic identification of the cyst types. We believe that, with further development, our chip-scale microscope can potentially provide a low-cost and portable solution to microscopy-based diagnosis of waterborne parasite infection in resource-poor settings.

Chapter 5 presents a smartphone-based lensless microscope using an ambient light source and the user's hand motion. We have constructed prototypes systems by removing the lens-module in a smartphone camera and placing the samples on the surface of the image sensor. The image sensor captures direct shadow images of the sample while the user tilts the device around a light source, such as the sun, a lamp or a flashlight. The corresponding sub-pixel-shifted shadows are analyzed with vision processing and processed with pixel-super resolution algorithm for high-resolution reconstruction. We discussed both hardware modification and the android application for image acquisition and reconstruction using OpenCV vision library. We have shown various images of microscopic samples - blood smear, microspheres and freshwater green algae - and demonstrated the imaging capability of our system. We achieved sub-micron resolution over ultra-wide FOV ($4 \text{ mm} \times 3 \text{ mm}$) in lensless and light source-free scheme. Our smartphone microscope features one of the most compact and simple designs among portable microscope devices developed to this date.

In Chapter 6, we developed a chip-scale fluorescence microscope using SF-CMOS image sensors. Our extruded pixel design eliminates the undesirable separation between the sample and the CMOS imager that the absorptive filter layer would otherwise introduce. We successfully imaged fluorescent samples with the SF sensor, achieving $13\text{-}\mu\text{m}$ resolution over $4.8 \times 4.4 \text{ mm}^2$ FOV. In addition, we demonstrated an ePetri imaging system using the SF sensors, which can obtain both bright-field and fluorescence images in a compact, low-cost geometry, suitable for long-term monitoring and various image-based biological analysis.

